Crystal Engineering of Mixed-Ligand Metal-Organic Frameworks

Tayyibah Tahier

Dissertation presented for the degree of

Master of Science

in the Department of Chemistry

University of Cape Town

July 2016

Supervisor: Dr. C. L. Oliver

Acknowledgements

A special thanks to:

My supervisor, Dr. C. L. Oliver, for his supervision, direction and encouragement. I am truly grateful for all the help I received throughout this project.

All the members of the Centre for Supramolecular Research group. Thank you for all the advice and friendship you have given me during my postgraduate studies.

My friends, for their constant motivation and for always inspiring me.

My mother, for her love and patience throughout my studies. Thank you for all your support and for always being there for me.

Parts of this thesis have been published:

Tayyibah Tahier and C. L. Oliver, In situ variable-temperature single crystal X-ray diffraction studies of the single-crystal-to-single-crystal dehydration and rehydration of a mixed-ligand 2D zinc metal–organic framework using trimesate and 4,4'-bipyridine-N,N'-dioxide as ligands, CrystEngComm., 2015, **17**, 8946-8956.

Abbreviations

1D – one dimensional

2D – two dimensional

3D – three dimensional

4,4'-bpdo – 4,4'-bipyridine-*N*,*N*'-dioxide

ASU – asymmetric unit

BET - Brunauer-Emmett-Teller

bpy – 4,4-bipyridine

bpe - 1,2-bis(4-pyridyl)ethane

CSD – Cambridge structural database

DEF – *N*,*N*'-diethylformamide

DMF – *N*,*N*'-dimethylformamide

DSC – differential scanning calorimetry

EA – elemental analysis

H_3BTC – 1,3,5-benzenetricarboxylic acid (trimesic acid)

HSM – hot stage microscopy

FT-IR – Fourier transform infrared spectroscopy

MOF – metal-organic framework

H_2nbdc – 5-nitro-1,3-benzenedicarboxylic acid

PXRD – powder X-ray diffraction

SBU – secondary building unit

SCSC – single-crystal-to-single-crystal

SCXRD – single crystal X-ray diffraction

sof – site occupancy factor

TG – thermogravimetric

TGA – thermogravimetric analysis

VT-PXRD – variable-temperature powder X-ray diffraction

VT-SCXRD – variable-temperature single crystal X-ray diffraction

Abstract

Research of solid state complexes has grown and developed exponentially over the past few years in terms of supramolecular chemistry and crystal engineering. The synthesis and characterisation of metal-organic frameworks (MOFs) have attracted widespread attention owing to their potential in various applications. This includes gas sorption, which could aid in alleviating serious environmental issues such as global warming by sequestrating greenhouse gases. Advances in the design of these materials using the mixed ligand approach add to variation in structures and thus provide a further means of tailoring of properties.

A novel two dimensional, mixed-ligand MOF has been synthesised based on 1,3,5-benzenetricarboxylic acid, 4,4'-bipyridine-*N*,*N*'-dioxide and zinc sulfate with the formula $[Zn_3(BTC)(4,4'\text{-bpdo})(OH)(SO_4)(H_2O)_3]_n \cdot n(H_2O)_{2.33}$ (**1**). The 2D layers of **1** arrange in a polar fashion with adjacent layers forming isolated cavities. Variable-temperature powder X-ray diffraction (VT-PXRD) analysis showed that the crystallinity of the compound was retained and the crystalline phase remained unchanged as the temperature was increased. Variable-temperature single crystal X-ray diffraction (VT-SCXRD) analysis of **1** revealed that the dehydration and rehydration processes occur *via* single-crystal-to-single-crystal transformations. Water vapour sorption experiments showed a type-I isotherm, typical of microporous materials.

A two dimensional, interpenetrated, mixed-ligand MOF has been synthesised based on 5-nitro-1,3-benzenedicarboxylic acid, 1,2-bis(4-pyridyl)ethane and cadmium nitrate with the formula $[Cd(bpe)_{1.5}nbdc]\cdot DMF$ (**2**). VT-PXRD analysis shows subtle differences in the compound as the temperature is increased. VT-SCXRD experiments show that the most notable change in the structure occurs at 373 K. These changes include the removal of the guest molecule and a change in the crystal system, along with changes in the orientation of the pyridyl ring of the organic ligand. Carbon dioxide sorption experiments at 195 K showed a type-IV isotherm, which is usually associated with mesoporous materials.

Both **1** and **2** were synthesised using the solvothermal method and fully characterised using X-ray diffraction studies (SCXRD, PXRD, VT-SCXRD and VT-PXRD), thermal analysis (thermogravimetric, differential scanning calorimetry, hot stage microscopy), elemental analysis and FT-IR spectroscopy. The porosity of the compounds was tested using carbon dioxide (273 K and 193 K), nitrogen, water vapour and liquid sorption experiments.

Table of contents

CHAPTER 1: INTRODUCTION

Important topics and terms which are associated with metal-organic frameworks, such as supramolecular chemistry, reticular synthesis, crystal engineering, interpenetration and single-crystal-to-single-crystal transformations are explored. The importance of porosity, which is related to applications of metal-organic frameworks that include water vapour and gas sorption is discussed. The use of mixed ligands that were used in the synthesis of the compounds is rationalised. Motivation and objectives of this research project are stated at the end of this chapter.

1.1 Supramolecular Chemistry and Crystal Engineering

The term "supramolecular chemistry" refers to chemistry involving the intermolecular bond, whereas molecular chemistry is concerned with covalent bonds between atoms.[1] Supramolecular chemistry is aimed at constructing highly complex, functional systems held together by intermolecular interactions.[1] These interactions may include coulombic interactions and non-covalent bonds (e.g. van der Waals and hydrogen bonding interactions) between molecules.[2] Supramolecular chemistry explores systems that are capable of generating well-defined, organised supramolecular architectures by self-assembly of their molecular components. Structural chemists and crystallographers recognise that crystals have a higher level of complexity than molecules.[3,4] Metal-organic frameworks (MOFs) and coordination polymers fall under examples of supramolecular complexes by virtue of their host-guest and possibly host-host interactions in the case of interpenetration.

The concepts of supramolecular chemistry are inherently linked to crystal engineering, which is recognised as an important form of supramolecular synthesis.[3,5] Crystal engineering has been defined as the rational design of functional molecular solids with desired physical and chemical properties.[3,4] The term crystal engineering was first used in the literature in 1955 by R. Pepinsky in a meeting abstract of the American Physical Society, but it is generally associated with the work contributed by G. M. J. Schmidt and A. I. Kitaigorodskii.[6] The subject of crystal engineering consists of three aspects, these include i) the study of intermolecular interactions ii) the study of the packing modes, in the context of these interactions; and iii) the study of crystal properties and their fine-tuning with purposeful

variations within the structure.[4] Through the knowledge of crystal engineering, the synthesis and design of MOFs have received significant attention in recent years. The main aim of crystal engineering is to construct crystal frameworks from molecular structures. This is the synthetic step, which is not always easy due to the complex nature of crystal structures.[4,7]

1.2 Metal-Organic Frameworks and Coordination Polymers

Coordination polymers and metal-organic frameworks (MOFs) originate from solid state, inorganic and coordination chemistry.[8] These materials are constructed from metal ions and organic linkers. The definitions of coordination polymers and MOFs vary between journals and authors. Terminology and nomenclature should be used as tools to constructively discuss new compounds and materials as well as create added value to any scientific field.[8,9] Some authors use the terms interchangeably, while others consider MOFs to be a subclass of coordination polymers.[7,10–14] This thesis deals with studies of 2D MOFs, hence these terms will be discussed briefly in this section.

The term "coordination polymer" has been known since at least 1959, when Kinoshita *et al*. described the crystal structure of a three dimensional network with the formula [Cu(adiponitrile)$_2$] and nitrate anions. Other reports on coordination polymers appeared in 1960, but there was not much interest in the topic. It was in 1990 that the subject gained more attention, from work by Robson *et al*. and later by Yaghi *et al.*, amongst others.[15,16]

Yaghi *et al.* provided one of the earliest definitions of a MOF, when they described a MOF having extended channels and composed of organic ligands coordinated to metal ions.[17] This 3D interpenetrated, cationic MOF was prepared *via* hydrothermal synthesis, using 4,4'-bipyridine (bpy) and copper(II) nitrate as the starting materials, and had the formula [Cu(4,4'-bpy)$_{1.5}$·NO$_3$(H$_2$O)$_{1.5}$]. Ligands such as bpy led to structures with low stability and high flexibility. As a result, between 1998 and 2001 research was then focussed on synthesising MOFs with carboxylate functionality in order to stabilise frameworks. This greatly accelerated the production of robust porous MOFs as shown in multiple articles by Yaghi and co-workers.[17–19] The stabilization afforded by the carboxylate functionality can also be rationalised in terms of the Hard Soft Acid Base (HSAB) theory. Carboxylate groups fall under the category of hard Lewis bases. Although, zinc and cadmium fall under the category of

intermediate and soft metals, respectively, these metals are commonly used in the synthesis of MOFs.

Rowsell and Yaghi defined coordination polymers as extended connections of metal-ligand monomers through coordination bonds.[14] They suggested that in order for a solid to be defined as a MOF, it should possess the following characteristics; a geometrically well-defined structure and strong bonding that provide robustness with linking units that could be modified by organic synthesis. It would appear that MOFs based on bpy ligands would be excluded from their definition of MOFs. However, in the same paper, they refer to pyridyl-based MOFs and carboxylate-based MOFs as two individual groups but still as MOFs, highlighting the ambiguity in MOF terminology that existed at the time.[14]

Another distinction between the two terms was made by O'Keeffe. He suggested that the bonds formed in MOFs are stronger than those formed in coordination polymers, which are generally weaker and have lower stability.[20] According to Kitagawa *et al*., coordination polymers or MOFs may have frameworks composed of a variety of structures ranging from 1D, 2D to 3D structures.[10] The definitions of coordination polymers and MOFs, respectively, according to the IUPAC recommendations are as follows, "A coordination compound with repeating coordination entities extending in 1, 2 or 3 dimensions" and "A metal-organic framework, abbreviated to MOF, is a coordination network with organic ligands containing potential voids."[9] In this dissertation, the IUPAC definition of MOFs will be followed.

As stated by Batten *et al*.[8], new terminology should help us discuss new compounds without having to go through never-ending definitions that might obstruct literature searches. More importantly, the properties of the materials should matter the most.[8] MOFs exhibit chemical and structural versatility which can be exploited in order to tune the physical and chemical properties of the structure.[10–12,21]

1.3 Topology

Topology is used to enhance the description of crystal structures of MOFs. Network topology is an important aspect in the analysis and design of MOFs. This type of analysis provides insight into the underlying network of a structure. Complicated crystal lattices can be simplified to equivalent nodes and rods sets.[22,23] Nodes may be placed at the metal

centre, at the centre of the metal ion cluster or at the centre of the organic ligand. Rods represent the linkages between the nodes, often aligned with the axis of a ligand. **Figure 1.1** shows some of the simplest architectures that can be produced using commonly available metal ions and organic linkers. A recurring feature of these types of networks is the presence of voids, which arise due to the architecture itself and the dimensions of the organic linkers and may thus add to the functionality of the structure by being porous.[5]

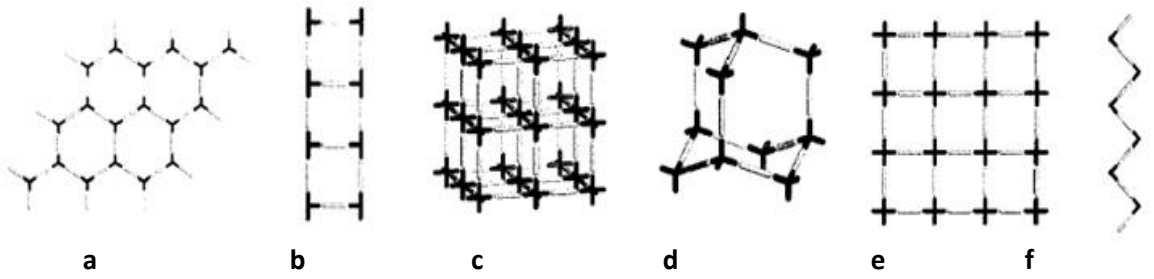

Figure 1.1: Schematic representation given by Moulton *et al.*[5] of some of the simple network architectures reported for MOFs **a)** 2D honeycomb **b)** 1D ladder **c)** 3D octahedral **d)** 3D hexagonal diamondoid **e)** 2D square grid and **f)** 1D zigzag chain. Reprinted (adapted) with permission from (B. Moulton and M. J. Zaworotko, *Chem. Rev.*, 2001, **101**, 1629–1658). Copyright (2001) American Chemical Society.

1.4 Reticular Synthesis

The term reticular synthesis is used to describe the logical process of assembling molecular building blocks into pre-determined networks and is a subset of crystal engineering. Research in the area of MOFs has progressed to a stage where the viability of the building block approach and the scope of reticular synthesis have been demonstrated.[19]

MOFs are designed and synthesised using building blocks, which consist of metal ions and organic linkers.[7,10–12] Yaghi *et al.* focussed on using the carboxylate functionality to chelate metal ions and lock them into robust, directional metal-oxygen-carbon clusters. These clusters are referred to as secondary building units (SBUs). The clusters act as connection points and can have varied geometries. The successful design of robust frameworks was first accomplished by Yaghi's group in MOF-2 and MOF-5.[17,19] In MOF-5, $Zn_4O(CO_2)_6$ units consisting of four ZnO_4 tetrahedra, with a common vertex and six carbon atoms from carboxylate ligands that represent an octahedral SBU, are linked together by benzene rings (**Figure 1.2.a**). In principle, the cubic network was prepared with Zn(II) and 1,4-benzenedicarboxylic acid to yield the octahedral SBU *in situ*. Since the SBU and benzene entities are large and rigid, the overall framework is highly porous and stable (as observed

from the sorption studies and thermal analysis of the framework). The stability of MOF-5 can be understood by comparing the basic network made up of single atom vertices with the actual structure (**Figure 1.2.b**). The concept of SBUs has been useful in rationalizing the topologies of MOFs.[19,24]

a **b**

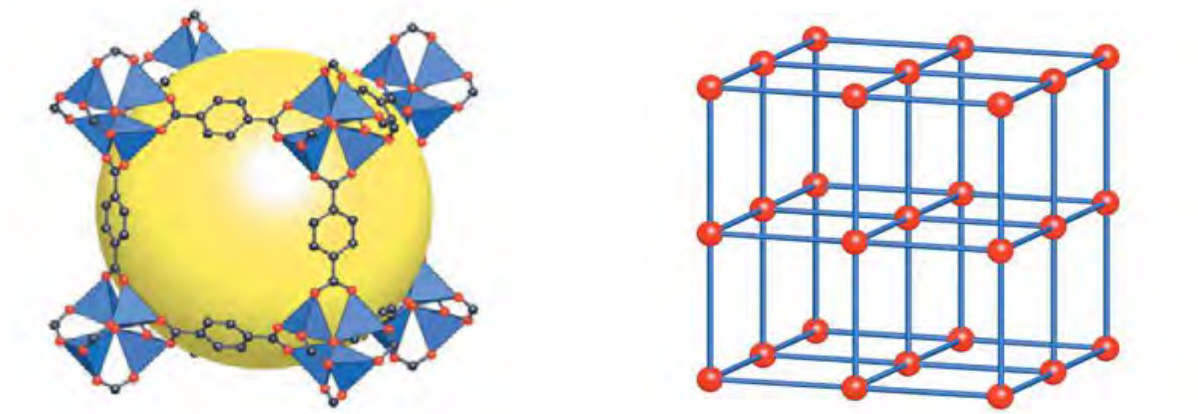

Figure 1.2: a) MOF-5 structure shown as ZnO_4 tetrahedra joined by benzenedicarboxylate linkers **b)** topology of MOF-5 shown as a "ball (metal cluster) and stick (organic linker)" model[19]

1.5 Porosity

Porosity is an important aspect in the functionality of MOFs. Porous MOFs are used in various applications, such as gas and solvent sorption. In an article published by Barbour,[25] permeability in conventional porous MOFs can be defined when solvent molecules can be removed completely, or exchanged without substantial disruption to the topology of the host framework. In the same article, Barbour classifies porosity into additional categories: i) virtual porosity and ii) porosity "without pores".[25]

Virtual porosity involves deleting atoms from the ASU of the crystal structure. The choice of which molecules to delete is generally based on the particular choice of guest molecule, regardless of whether it plays an important structural role or not. A packing diagram is then produced to show that large open channels have been generated by this process. It is then declared that the channels generated are pores.[25]

Porosity "without pores" can be explained through dynamic processes that occur within the crystal structure. For example, a crystal structure of the bowl-shaped molecule *p-tert*-butylcalix[4]arene was found to contain discrete lattice voids of 235 $Å^3$, but closer inspection showed that there were no channels connecting these voids. **Figure 1.3** shows

the two dimensional packing arrangement of *p-tert*-butylcalix[4]arene, with the voids depicted as yellow contact surfaces generated using a probe radius of 1.5 Å. It is clear that the voids are not interconnected, therefore the structure seems nonporous to a sphere of radius 1.5 Å. However, exposing the crystals to liquid vinyl bromide resulted in a single-crystal-to-single-crystal (SCSC) transformation with the vinyl bromide molecules enclosed in the void space.[25,26] Furthermore, when the guest free *p-tert*-butylcalix[4]arene molecule is exposed to air, carbon dioxide, methane or hydrogen respectively, the gases are absorbed by the structure. It has been suggested that the processes involve the host molecules cooperating with one another to create opportunities for the guest molecules to enter or leave the crystal structure. The authors claim that it is difficult to determine the exact mechanisms of these processes due to the transient nature of the porosity.[25,26]

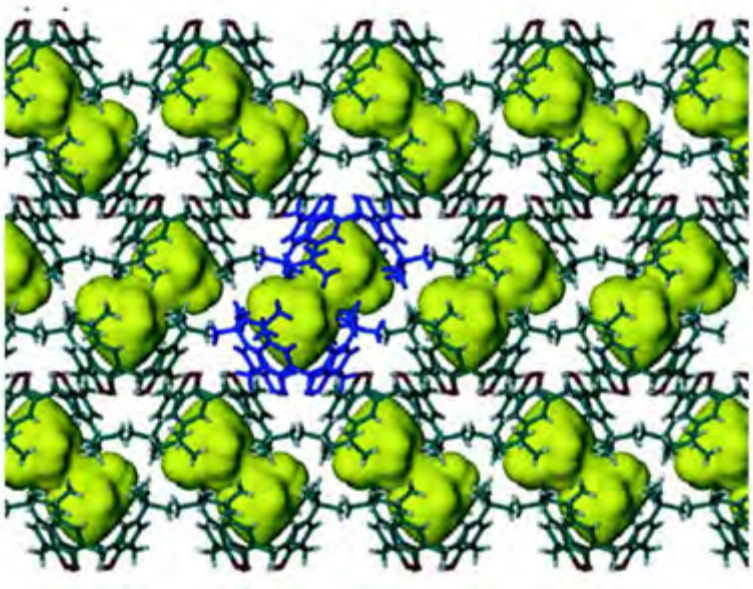

Figure 1.3: Two dimensional packing arrangement of *p-tert*-butylcalix[4]arene.[25] Reprinted (adapted) with permission from (L. J. Barbour, *Chem. Commun.*, 2006, 1163–1168). Copyright (2006) American Chemical Society.

Undoubtedly, one of the most attractive features of MOFs is their crystalline and porous nature. However, some MOFs may show initial promise in terms of porosity, but cannot withstand the desolvation process or reabsorb either the same or different solvent molecules.[27,28] As stated by Barbour, it might seem strange to suggest that crystals possessing discrete voids, but no open channels leading to these voids might be permeable, but examples like these have been observed in the literature.[25]

Conventional porosity requires the existence of infinite open channels with a 3–10 Å diameter range in the host framework. However, molecules in crystals tend to pack close to each other in order to maximise attractive intermolecular interactions. It is quite rare to find structures with open channels or isolated void spaces larger than 25 $Å^3$. MOFs have become attractive materials for porosity, since they consist of infinite frameworks of interconnected units. The coordination geometries around the metal centres lay the foundation for these frameworks; hence the structural variations that are possible by combining metal and bridging ligands are endless. In many structures, solvent molecules fill the void spaces formed by metal-ligand networks.[25]

1.6 Interpenetration

Interpenetration is a common phenomenon which occurs in MOFs, whereby two or more distinct frameworks are entangled over an entire crystal lattice.[21] Pore size and framework stability are two of the most important factors in the synthesis of MOFs specifically with regards to porosity.[29] It has been suggested that by using elongated organic linkers (such as pyridyl-based ligands), it is possible to synthesise MOFs with ultrahigh porosity. However, an increase in pore size may lead to unstable frameworks. This generally leads to crystal structures with interpenetration, which have increased stabilities due to the maximisation of contacts at the expense of the large void space.[28,30,31] Although no covalent bonding exists between the interpenetrated frameworks, they cannot be separated without the breaking of various chemical bonds.[30,32,33] The degree of interpenetration ("n-fold" refers to "n frameworks") could be 2-fold or greater, resulting in reduced voids.[31]

Many examples have been reported in the literature whereby interpenetration affects the porosity of frameworks for sorption applications.[11,21,34,35] While interpenetration reduces the pore size of the framework, it is not necessarily a disadvantage.[21] The structure may still exhibit useful properties such as an increase in stability, due to an increase in the amount of supramolecular interactions per framework, to aid in sorption studies.[36,37] Zhou *et al*. found that interpenetration was an important factor in the uptake of gases for their structures.[34,38] In their study, the Langmuir surface area and volumetric hydrogen uptake for PCN-6 (interpenetrated structure) and PCN-6' (non-interpenetrated structure) were compared. The N_2 adsorption isotherm for both structures activated at 50 °C showed a type-I isotherm

(**Figure 1.4.a**), with the Langmuir surface area for PCN-6 calculated to 3800 m^2 g^{-1}, which was 41% more than PCN-6' (Langmuir surface area of 2700 m^2 g^{-1}). Hydrogen adsorption studies (**Figure 1.4.b**) showed that PCN-6' activated at 50 °C can absorb 1.35 wt% hydrogen at 760 Torr and 77 K (volumetric uptake = 3.94 kg m^{-3}), while PCN-6 activated at 50 °C absorbs 1.74 wt% hydrogen (volumetric uptake = 9.19 kg m^{-3}). It was suggested that this increase could be due to the formation of new adsorption sites and small pore sizes formed as a result of interpenetration. The smaller pore sizes increase interactions between hydrogen gas and the framework, therefore increasing the apparent surface area and causing PCN-6 to absorb more gas. However, if open channels are blocked as a result of interpenetration, the overall surface area of a framework may drop significantly.[38]

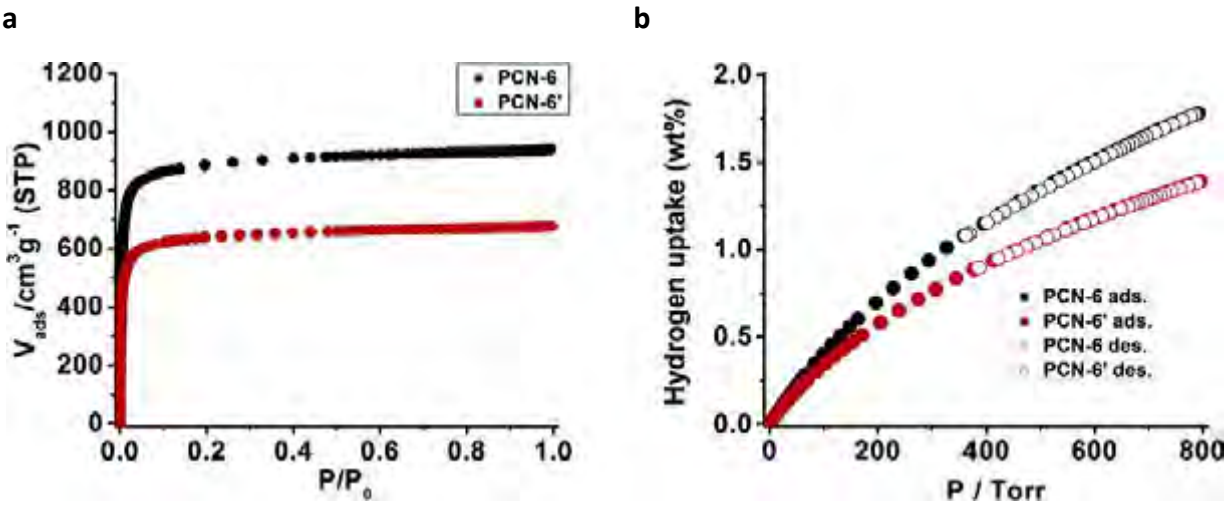

Figure 1.4: Gas sorption isotherms (77 K) of PCN-6 and PCN-6' activated at 50 °C for **a)** N_2 and **b)** H_2[38]
Reprinted (adapted) with permission from (S. Ma, D. Sun, M. Ambrogio, J. A. Fillinger, S. Parkin and H. C. Zhou, *J. Am. Chem. Soc.*, 2007, **129**, 1858–1859). Copyright (2007) American Chemical Society.

Different synthetic procedures (such as temperature and concentration control) have been developed in order to attain a certain control of interpenetration in MOFs, having in mind their potential benefits.[39] However, these analyses are commonly devoted to 3D MOFs, due to the vast amount of information found in the scientific literature for these types of networks. Information on interpenetration in 2D MOFs is scattered in the literature, with the properties being occasionally investigated.[40]

It should be noted that the properties of interpenetrated MOFs are not only related to their molecular structures, but also to the topology of the network as well as the way in which the individual networks are entangled. Interpenetrated 2D MOFs exhibit a variety of distinct

topologies and entanglement types of 2D nets. The most frequent types of topologies that occur in 2D MOFs are the square lattice and honeycomb type.[40]

1.7 Applications

The design and structure of robust MOFs make them ideal candidates for a variety of applications. Most MOFs have been designed with the expectation of producing large pore sizes to achieve maximum sorption of gases. There are numerous reports in the literature where these materials have successfully been used for gas storage, molecular sensing, separations and catalysis.[10,11,13,18,21,22,24,28,30,31,36,37,41–43]

Yaghi and co-workers investigated nine compounds for their structural and porosity attributes. The list represents frameworks of various characteristics such as square channels (MOF-2), pores with open metal sites (MOF-505 and $Cu_3(BTC)_2$), packed cylindrical channels (MOF-74), interpenetration (IRMOF-11), alkyl and amino functionalised pores (IRMOF-3 and -6) and ultra high porous frameworks (IRMOF-1 and MOF-177). From the list, MOF-177 had the highest surface area when compared to the other structures, with the Brunauer-Emmett-Teller (BET) surface area equal to 4508 m g^{-1}.[28,44] The framework was synthesised by heating a mixture of 1,3,5-benzenetribenzoate (BTB, shown in **Figure 1.5a**) and $Zn(NO_3)_2{\cdot}6H_2O$ in *N*,*N*'-diethylformamide (DEF) to 100 °C. Single crystal X-ray diffraction (SCXRD) analysis revealed that the compound had the formula $Zn_4O(BTB)_2{\cdot}(DEF)_{15}(H_2O)_3$ and that it was an open, three dimensional framework.[45] The crystal structure depicting the void available in MOF-177 is shown in **Figure 1.5b**.

a **b**

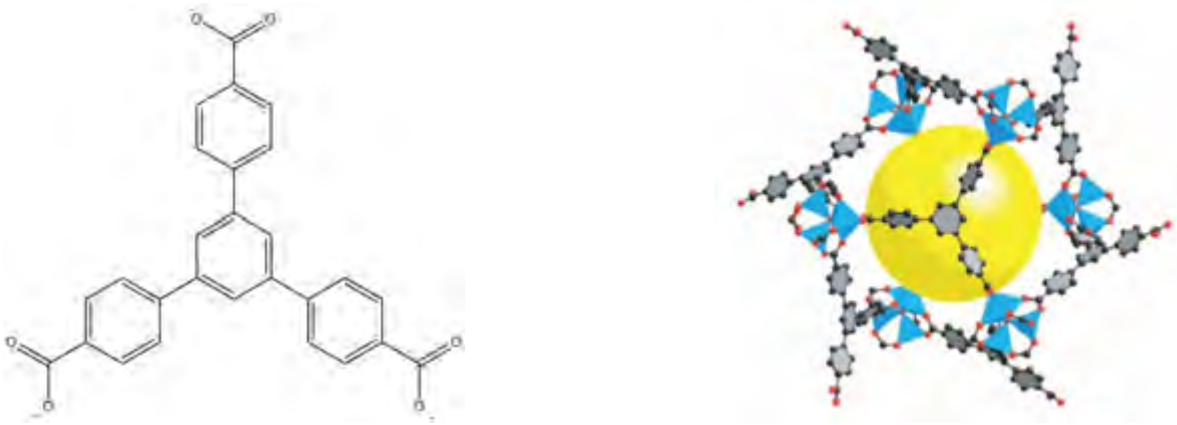

Figure 1.5: a) Chemical structure of 1,3,5-benzenetribenzoate (BTB) **b)** single void shown as a yellow sphere in MOF-177.[28] Reprinted (adapted) with permission from (H. Furukawa, N. Ko, Y. B. Go, N. Aratani, S. B. Choi, E. Choi, A. Ö. Yazaydin, R. Q. Snurr, M. O'Keeffe, J. Kim and O. M. Yaghi, *Science*, 2010, **329**, 424–428). Copyright (2010) American Chemical Society.

The room temperature CO_2 adsorption isotherms of the selected MOFs are shown in **Figure 1.6**. The volumetric space enclosed by MOF-177 resulted in a CO_2 capacity of 33.5 mmol g^{-1}. This value is larger than any other value reported for a porous material. It must be noted that although MOF-177 absorbs more CO_2 at 35 bar, it does not exclude the use of other MOFs for CO_2 uptake, especially since it is outperformed by many of these MOFs at lower pressures.[44]

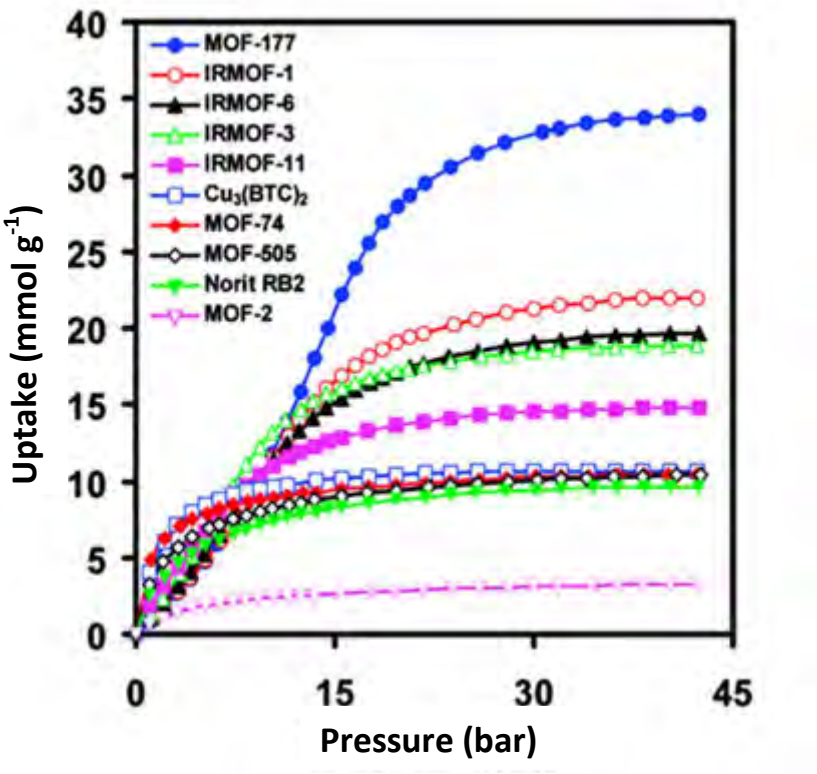

Figure 1.6: Comparison of gravimetric CO_2 capacities for several MOFs determined at room temperature and pressure up to 42 bar.[44] Reprinted (adapted) with permission from (A. R. Millward and O. M. Yaghi, *J. Am. Chem. Soc.*, 2005, **127**, 17998–17999). Copyright (2010) American Chemical Society.

A comparison was also made between MOF-177 and benchmark physisorptive materials at the time, such as zeolite 13X and MAXSORB. Zeolites are one of the earliest, most highly successful porous materials in industrial applications, based on their stability, well-defined pore shapes and narrow pore-size distributions. Although MOFs and zeolites are similar in design, the former class of materials has the potential for larger pore sizes and greater access to these pores. [44,46,47] The highest reported gravimetric CO_2 capacity for zeolites at 25 °C is 7.4 mmol g^{-1} (at 32 bar) for zeolite 13X. Alternatively, a sample of MAXSORB (a type of carbon powder) showed an uptake of 25 mmol g^{-1} (at 35 bar), while it was shown that MOF-177 had a gravimetric CO_2 capacity of 33.5 mmol g^{-1} at 25 °C and 42 bar, exceeding

that of the benchmark materials. Amazingly, at 35 bar, a container filled with MOF-177 can absorb twice the amount of CO_2 than a container filled with benchmark materials and nine times the amount of CO_2 than a container without absorbent (**Figure 1.7**). These results show that MOFs represent a new direction for absorbing gases such as CO_2 from the atmosphere.[44]

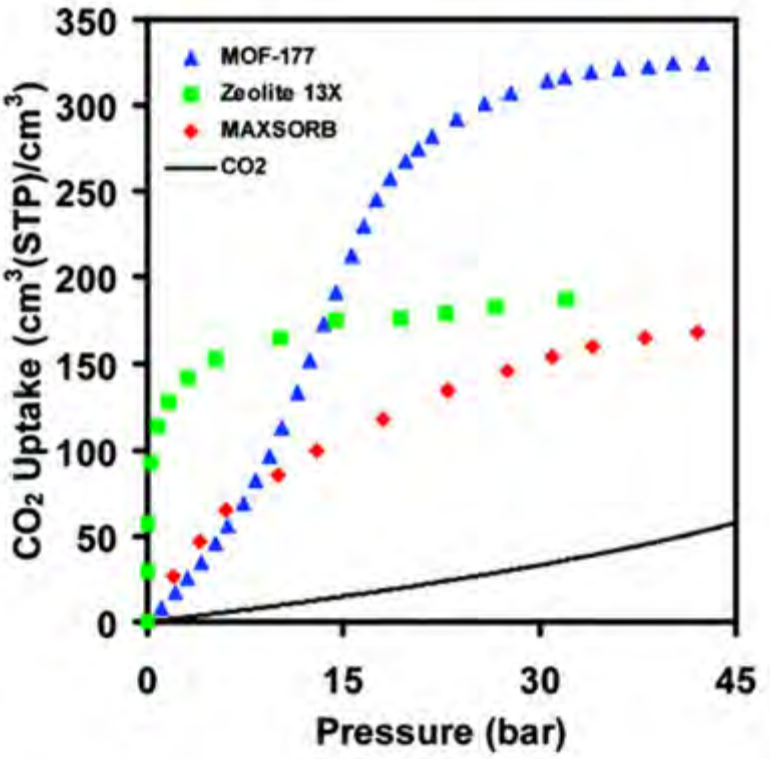

Figure 1.7: Comparison of the volumetric CO_2 capacity of MOF-177 relative to zeolite 13X, MAXSORB carbon powder and pressurised CO_2.[44] Reprinted (adapted) with permission from (A. R. Millward and O. M. Yaghi, *J. Am. Chem. Soc.*, 2005, **127**, 17998–17999). Copyright (2010) American Chemical Society.

As mentioned in the previous section, interpenetration affects the porosity and gas sorption properties of MOFs. However, interpenetrating MOFs are commonly used in gas sorption studies and there are many examples that can be found in the literature. Sun *et al*. studied gas sorption properties of a four-fold interpenetrated copper(II) framework $[Cu(INAIP)]\cdot 2H_2O$ (**CuINAIP**), where $INAIP^{2-}$ = 5-(isonicotinamido)isophthalate (**Figure 1.8a**). The coordination environment of Cu(II) in the ASU of **CuINAIP** is shown in **Figure 1.8b**.[36]

a **b**

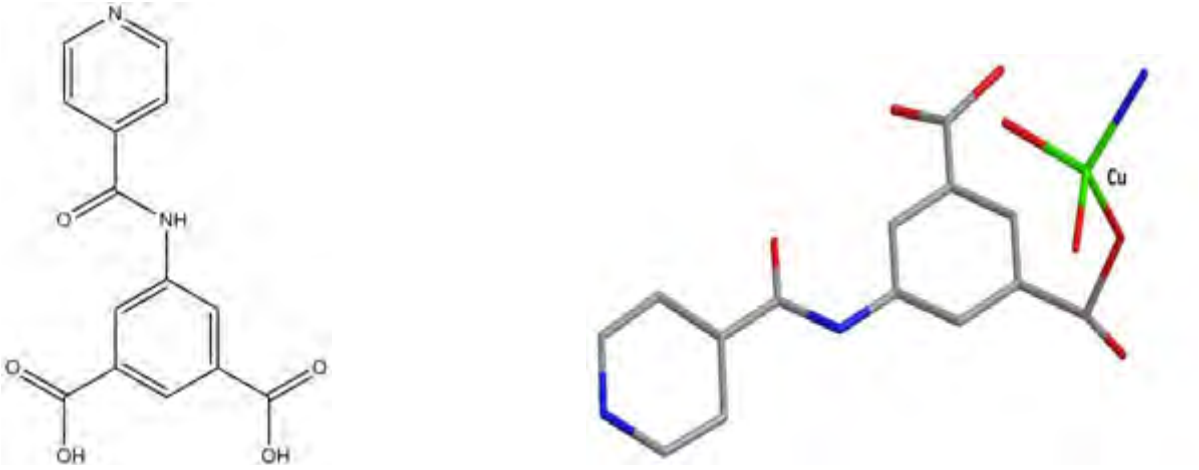

Figure 1.8: a) Chemical structure of H_2INAIP **b)** coordination environment of Cu(II) in the ASU of **CuINAIP**. Reprinted (adapted) with permission from (M. S. Chen, M. Chen, S. Takamizawa, T. Okamura, J. Fan and W. Y. Sun, *Chem. Commun.*, 2011, **47**, 3787–9). Copyright (2011) American Chemical Society.

Crystals of **CuINAIP** were heated to 180 °C, which resulted in the dehydrated form, **CuINAIPD**. The most interesting feature of the H_2 type-I isotherm of **CuINAIPD** is its steep slope at low pressures (**Figure 1.9.a**). This indicates that the pores available in **CuINAIPD** have strong interactions with H_2 molecules.[36] Further gas sorption studies were performed on the structure with CO_2 and N_2 gas (**Figure 1.9.b**). Interestingly, **CuINAIPD** displayed selective gas adsorption for CO_2 over N_2 gas. The sorption measurements of CO_2 for **CuINAIPD** also displayed type-I isotherms, typical of microporous materials, which at 1 atm indicated values of 57.64 and 47.34 cm^3 (STP) g^{-1} for 273 K and 298 K, respectively, whilst the N_2 sorption isotherm indicated lower values of 4.68 and 2.71 cm^3 (STP) g^{-1} at 273 K and 298 K, respectively.

Additionally, **CuINAIPD** was subjected to vapour sorption studies. The compound showed type-I isotherms for water and alcohol vapours.[36] At lower pressures (0-0.08 atm), the rate of vapour sorption is higher for water than the alcohol vapours (**Figure 1.9.c**). It was also clear that the absorption of alcohol molecules was size dependent, indicated by a decrease in sorption as the carbon chain length increased.[36]

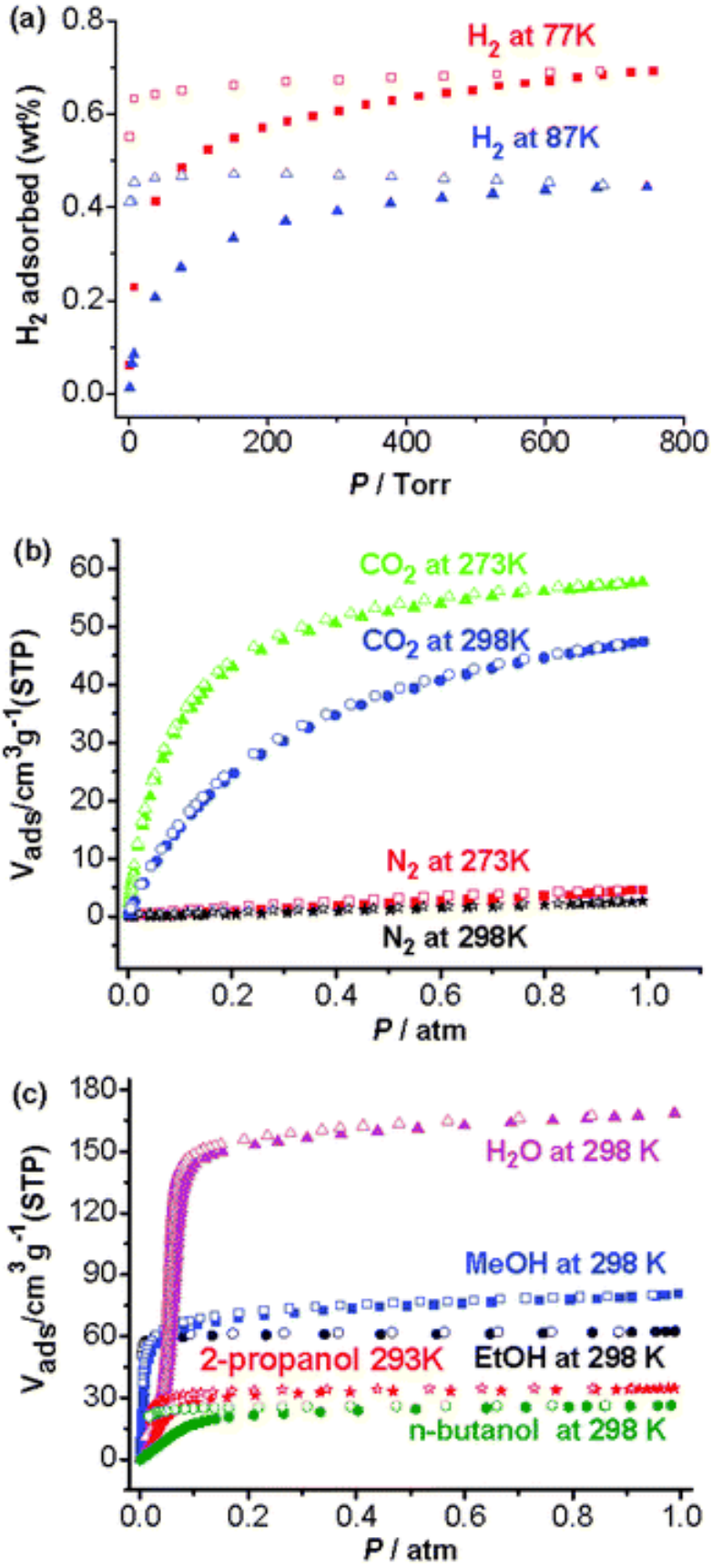

Figure 1.9: CuID sorption isotherms of **a)** hydrogen **b)** carbon dioxide and nitrogen sorption and **c)** water and various alcohols.[36] Reprinted (adapted) with permission from (M. S. Chen, M. Chen, S. Takamizawa, T. Okamura, J. Fan and W. Y. Sun, *Chem. Commun.*, 2011, **47**, 3787–9). Copyright (2011) American Chemical Society.

1.8 Single-Crystal-to-Single-Crystal Transformations

Single-crystal-to-single-crystal (SCSC) transformations have received much interest in the field of crystal engineering. However, examples of these transformations in the literature are rare since most crystals are unable to retain their crystallinity upon rearrangement of molecules.[48–51] These structural changes may be induced as a result of external stimuli such as heat or light, which may cause the movement of solvent molecules in the framework, in the case of MOFs.[49,52,53] SCSC transformations are highly desirable since this allows for the visualisation of the transformed crystal structure when guest molecules are added or removed from the framework, while the original unit cell parameters are retained. This direct insight could provide a further understanding of the interactions that occur between solvent molecules and the host framework. It has been demonstrated that investigations into SCSC transformations can open routes to the systematic study of gas sorption, separation and solid state reactions.[48,51]

Kitagawa and co-workers reported on a series of flexible MOFs based on tris(2-carboxyethyl)isocyanurate (tci) that included $\{[Cu_2(tci)(OH)(H_2O)_3]\cdot 1.5H_2O\}_n$, $\{[Ce(tci)(H_2O)_2]\cdot 2H_2O\}_n$ and $\{[Pr(tci)(H_2O)_2]\cdot 2H_2O\}_n$ that showed reversible SCSC transformation from 2D to 3D frameworks through thermal dehydration/rehydration processes.[10,54] These compounds had a high affinity for H_2O molecules and in the case of the $\{[Cu_2(tci)(OH)(H_2O)_3]\cdot 1.5H_2O\}_n$ compound, it was suggested that the strong affinity for the water molecules arises due to the narrow channels leading to the metal sites and the hydrophilicity of the framework associated with the carbonyl groups of the ligands.[54] **Figure 1.10** illustrates the bonding rearrangements in $\{[Ce(tci)(H_2O)_2]\cdot 2H_2O\}_n$ during the SCSC transformation upon dehydration/rehydration of the compound.[10]

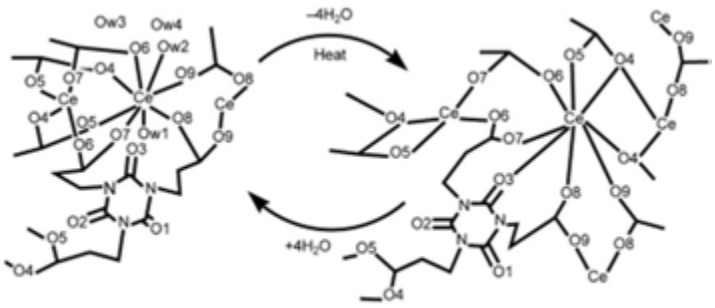

2D $\{[Ce(tci)(H_2O)_2]\cdot 2H_2O\}_n$ **(1)** **3D** $\{[Ce(tci)]\}_n$ **(1')**

Figure 1.10: Bonding rearrangements during the SCSC transformation of $\{[Ce(tci)(H_2O)_2]\cdot 2H_2O\}_n$[10]
Reprinted (adapted) with permission from (S. K. Ghosh, J. P. Zhang and S. Kitagawa, *Angew. Chemie Int. Ed.*, 2007, **46**, 7965–7968). Copyright (2007) American Chemical Society.

Cao *et al*. reported on the synthesis and characterisation of two new, isostructural compounds, $[Co(OBPT)_2]\cdot 0.6H_2O$ (**COBPT**) and $[Ni(OBPT)_2]\cdot 0.6H_2O$ (**NOBPT**), where OBPT = 1,4-bis(4-pyridyl)-1,3,5-tri-azin-2-oate (**Figure 1.11a**). The compounds undergo reversible SCSC transformation driven by thermal stimulation and involved the desorption and adsorption of water molecules. The coordination environment of Co(II) in **COBPT** is shown in **Figure 1.11b**.[46]

a **b**

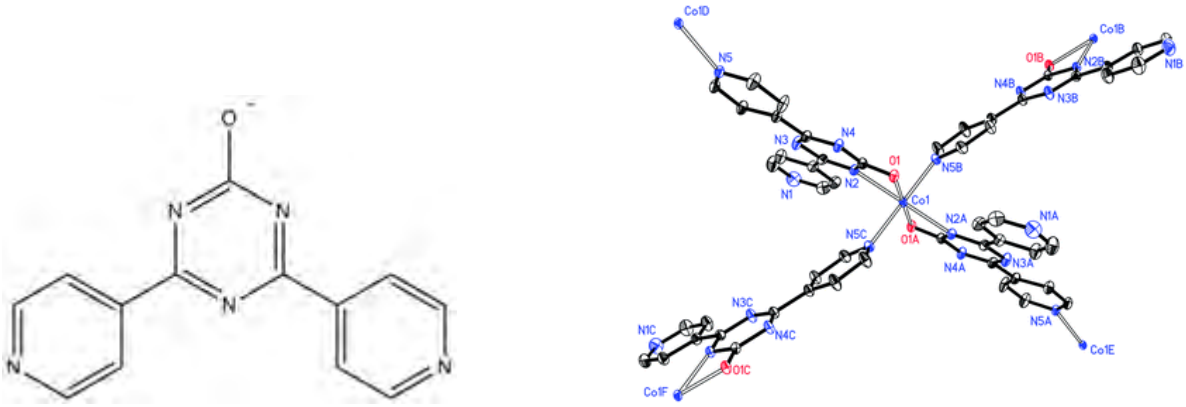

Figure 1.11: a) Chemical structure of 1,4-bis(4-pyridyl)-1,3,5-tri-azin-2-oate (OBPT) **b)** coordination geometry of cobalt(II) in **COBPT** (0.6 lattice H_2O molecule not shown). Reprinted (adapted) with permission from (M. Cao, H. Mo, J. Liang and B. Ye, *CrystEngComm*, 2009, **11**, 784–790). Copyright (2009) American Chemical Society.

The crystals of **COBPT** and **NOBPT** were heated to 200 °C for two hours to yield the dehydrated forms, **COBPTa** and **NOBPTa**, respectively. SCXRD analysis showed that the dehydration process did not cause a change in the framework structures. The removal of water molecules from the structures was confirmed by SCXRD, elemental and thermogravimetric (TG) analysis.[48] Single crystals of **COBPTa** were exposed to air for 3 days, which yielded the rehydrated form **COBPTa'**. SCXRD studies confirmed that the as-synthesised and rehydrated compounds are the same and also confirmed that dehydration and rehydration are completely reversible SCSC processes.[48]

To further examine the sorption and desorption properties of **COBPT**, two sets of experiments were performed. The first involved immersing crystals of **COBPT** in various organic solvents, which included methanol, ethanol, acetone, tetrahydrofuran, benzene, acetonitrile and trichloromethane to investigate whether the lattice water molecules could be exchanged. **COBPT** converted to **COBPTa** in the presence of methanol and ethanol, but remained unchanged in the presence of the other organic solvents. This indicated that the

water molecules were extracted by the alcohols, due to hydrogen bonding between the guest water molecules and the methanol and ethanol molecules, which pulls out the water molecules from the structure.

The second experiment involved immersing the dehydrated **COBPTa** in various organic wet solvents and a H_2O/MeOH mixture for 3 days. It was shown that **COBPTa** can absorb water molecules over organic solvents to recover the original framework. In contrast, the PXRD patterns of the crystals immersed in methanol and ethanol remained unchanged from **COBPTa**, indicating that the dehydrated form cannot absorb water molecules from methanol and ethanol solvents. The authors concluded that the dehydrated form can selectively absorb water molecules over organic solvents except alcohols.[48]

1.9 Metal Ions

The metal ion that is chosen for a particular MOF is of significant importance, since it will have an important role in the properties of the framework. Metal ions are often employed as versatile connectors in the construction of coordination polymers. The oxidation state usually ranges between 1+ and 3+, while the coordination number can range from 2–7 depending on the metal ion that is used, giving rise to a wide range of geometries. Since most metal connectors are cationic, a counter-ion must be present to neutralize the overall charge of the crystal structure. This counter ion may either be the anion of the starting metal salt or the ligand itself.

Zn(II) and Cd(II) are common metal components used in the preparation of MOFs. These metal ions have the ability to simultaneously form bonds with different donor atoms. They are found in group twelve of the periodic table and have relatively large atomic radii. Both metal ions have been reported with various coordination geometries.[55] The variation for Cd(II) and Zn (II) arises from two factors: i) their large ionic radii, which allow flexibility in terms of coordination numbers and ii) the electron configuration (d^{10}) of the metal ion. According to ligand field theory, complexes where the metal ion has a d^{10} electron configuration experience no ligand field stabilization and therefore the ligand environment is controlled by steric factors only, permitting a range of diverse geometries.[56,57]

1.10 Mixed-Ligand Metal-Organic Frameworks

The careful selection of suitable organic ligands with certain features is important for constructing MOFs with desirable properties.[58] Due to the modular nature of MOFs, it is possible to systematically design (in terms of dimensionality and pore volume) and construct these materials based on their desired applications. Mixed-ligand MOFs provide the possibility of tuning pore shape or size, since ligands of various sizes could be used in the synthesis of these materials, thus, allowing for further tailoring of properties. Research towards the rational design and construction of mixed-ligand MOFs show that bipyridine and polycarboxylate groups are the most reliable building blocks to use in the synthesis of these materials. Pillared ligands such as bipyridine may provide pore expansion, while carboxylate linkers provide structural complexity and variation of MOFs by virtue of their various coordination modes. Thus, the mixed-ligand synthetic strategy can be rationalised by combining the advantages of the two types of ligands.[22]

Ligands in mixed-ligand MOFs may be classed into three categories: i) base-base ligand pairs ii) acid-acid ligand pairs and iii) acid-base ligand pairs. The acid-base definitions in this sense refer to their classification before ligation. The acid-base system is the most significant and common branch of mixed-ligand MOFs. Acid-base partners are the perfect combination since they can compensate by balancing the charges, coordination deficiency and weak interaction within the framework simultaneously.[22] A disadvantage of using pyridyl-only based frameworks may arise when counter-ions required for charge compensation block any open channels. It has been suggested by Hupp *et al.* that these problems could be overcome by combining pyridyl coordination with carboxylate coordination in mixed-ligand MOFs. In addition, the mixed coordination may incorporate functionality within the framework.[42] The MOFs studied in this project were synthesised using the mixed ligand approach based on carboxylate and pyridyl moieties as acid-base partners.

These types of frameworks may prove to be challenging to synthesise, since the different linkers should have an equal probability of ligating to the metal ion. Not only do mixed-ligand MOFs allow for a synthetic approach to vary pore size, these compounds also incorporate interesting chemical and functional properties to the framework due to the different functional groups of the linkers.[37,59] Kitagawa and co-workers have led the way in

the synthesis of mixed-ligand MOFs with pillared networks.[22] Other examples of success in constructing mixed-ligand MOFs have been demonstrated by Husain *et al.* whereby a two-fold interpenetrated, 3D MOF has been constructed from Cd(II), trimesate and 1,2-bis(4-pyridyl)ethane.[37] The compound was found to be thermally stable and was subjected to liquid and gas sorption studies. Luo *et al*. hydrothermally synthesised a novel, 3D mixed-ligand MOF based on Cd(II), 5-nitro-1,3-benzenedicarboxylic acid and 1,2-bis(4-pyridyl)ethane. The thermal and fluorescent properties of this interpenetrated structure were reported by this group.[60]

1.10.1 Carboxylate Ligands

Multicarboxylate ligands are common choices for the construction of MOFs due to their high thermal and chemical stability of the carboxylate-metal fragment.[36,41,61] Carboxylate ligands also have different bridging modes (e.g. monodentate and bidentate) and have been proven to stabilize frameworks.[33,38,41,56] 1,3,5-benzenetricarboxylic acid (H_3BTC) is a rigid, planar molecule and demonstrates a wide variety of coordination modes once deprotonated making it ideal for the construction of MOFs.[61] The structure of H_3BTC once fully deprotonated and its various coordination modes are shown in **Figures 1.12**.

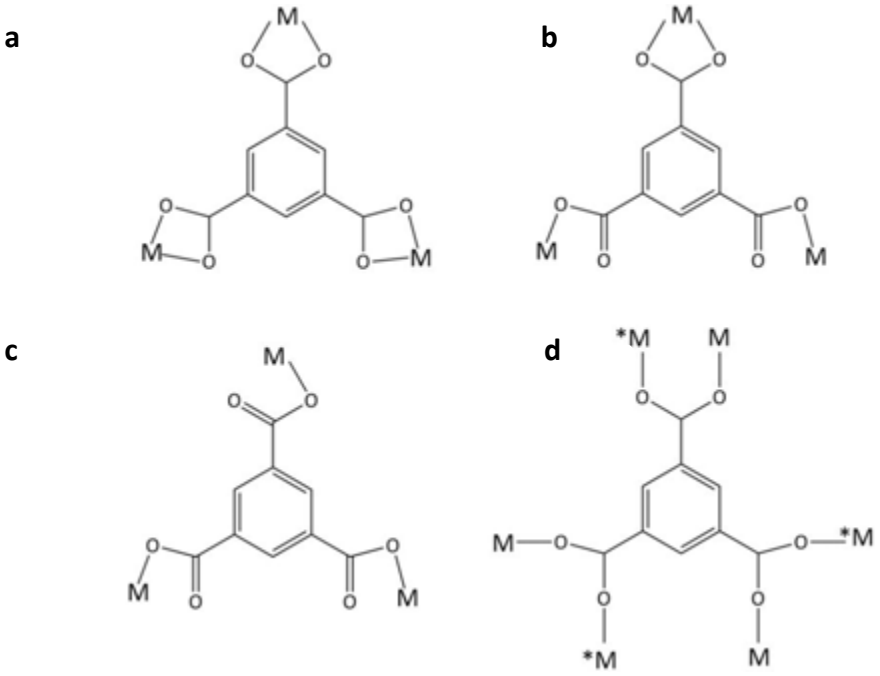

Figure 1.13: Fully deprotonated H_3BTC **a)** chelating in a bidentate fashion to a metal centre **b)** chelating in both a monodentate and bidentate fashion **c)** chelating in only a monodentate fashion **d)** bridging two metal centres in a bridging bidentate fashion.[61] Reprinted (adapted) with permission from (O. M. Yaghi, C. E. Davis, G. Li and H. Li, *J. Am. Chem. Soc.*, 1997, **119**, 2861–2868). Copyright (1997) American Chemical Society.

5-nitro-1,3-benzenedicarboxylic acid (**Figure 1.14**) is a derivative of a carboxylate-based ligand (*m*-isophthalic acid) and hence also displays a variety of coordination modes.[63] Generally, the nitro group (-NO_2) does not coordinate to metal ions, but could act as a hydrogen bond acceptor, which provides additional strength to the framework. The non-coordinating nitro group acts as an electron withdrawing group (EWG) of the ligand. This might have some effect on the electron density and coordination of the carboxylate groups.[64,65] The EWG could stabilize the conjugate base of the 5-nitro-1,3-benzenedicarboxylic acid ligand (H_2nbdc), increasing the probability of coordination.

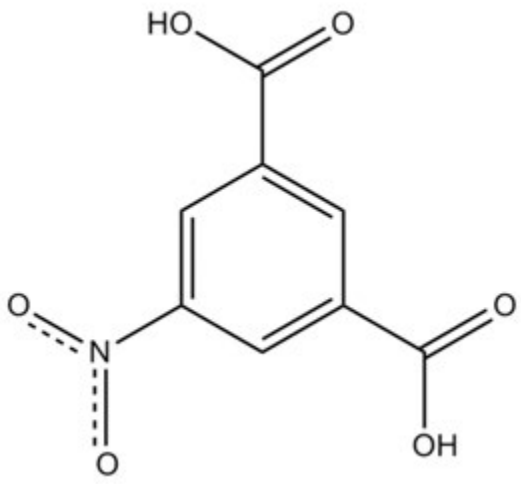

Figure 1.14: Chemical structure of 5-nitro-1,3-benzenedicarboxylic acid (H_2nbdc)

1.10.2 Pyridyl Ligands

Ligands containing two 4-pyridyl nitrogen donor atoms have been found to be useful in the construction of MOFs.[66] Elongated, pyridyl-based linkers are widely used and could provide frameworks with high porosity due to their tendency to extend the diameter of voids. The ligand, 1,2-bis(4-pyridyl)ethane (bpe) is an example of such a ligand and has proven to form stable compounds when paired with carboxylate-based ligands (**Figure 1.15a**).[22,37]

It has been shown that 4,4'-bipyridine-*N*,*N*'-dioxide (**Figure 1.15b**) and its derivatives show unique features in MOFs and have versatile coordination modes.[66] Long *et al*. have reported two Zn(II) complexes that contain four different coordination modes of 4,4'-bipyridine-*N*,*N*'-dioxide (4,4'-bpdo) *via* metal-ligand coordination, hydrogen bonding and $\pi - \pi$ interactions.[66] The positioning of the lone pairs on the pyridyl-N-oxide oxygen

atoms results in a liable coordination nature of the ligand, which causes structural diversity as the ligand can coordinate in more than one way. In addition to being a strongly versatile coordinating ligand, 4,4'-bpdo is a good hydrogen bond acceptor. However, only a few MOFs based on bpdo and carboxylate ligands have been reported.[58,67]

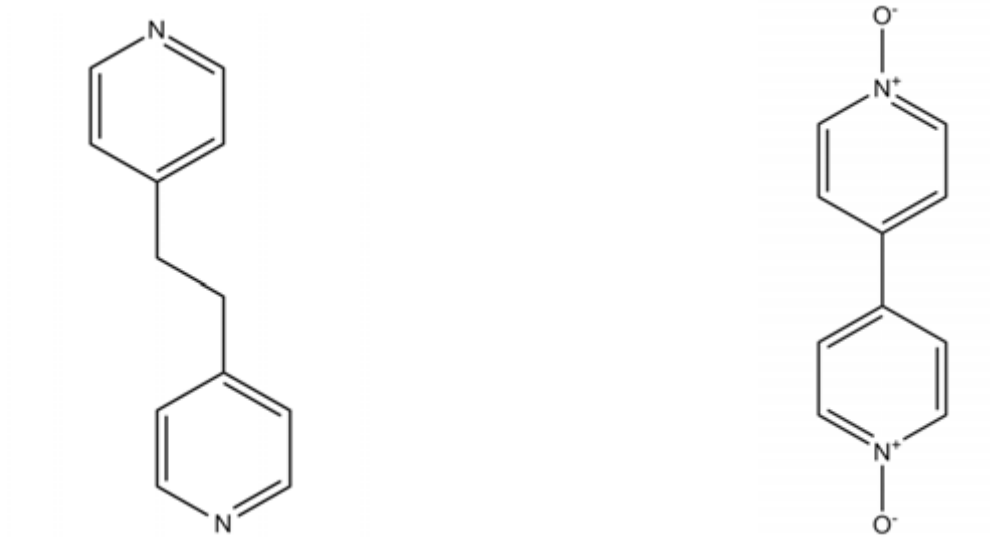

a) 1,2-bis(4-pyridyl)ethane (bpe) **b)** 4,4'-bipyridine-*N*,*N*'-dioxide (4,4'-bpdo)

Figure 1.15: Chemical structures of **a)** 1,2-bis(4-pyridyl)ethane and **b)** 4,4'-bipyridine-*N*,*N*'-dioxide

1.11 Motivation and Objectives

1.11.1 Motivation

Over recent years, there has been a growing interest in the synthesis of MOFs using the mixed-ligand approach. This method incorporates interesting properties of different functional groups in MOFs and can potentially be used to tune pore size for sorption studies. Crystal engineering was used as the foundation for this project in terms of selecting carboxylic acid and pyridyl-based ligands with the expectation of both linkers ligating to the metal centre to produce a mixed-ligand MOF. Zinc(II) and cadmium(II) were chosen as the metal ions. Both Zn(II) and Cd(II) are found in group twelve of the periodic table, which give rise to a wide range of geometries. Complete details relevant to the metal ions used in this project are provided in **section 1.9**. Carboxylate ligands and pyridyl ligands have been reported on extensively and contribute many advantages to frameworks of this nature, which are discussed in **section 1.10.1** and **1.10.2**, respectively. The ligands chosen in this

project are simple, cheap and do not require any prior modification in the synthesis of the MOFs in this project.

1.11.2 Objectives

The main objectives of this project were:

1. To prepare mixed-ligand MOFs based on carboxylate and pyridyl ligands.
2. To fully characterise the compounds using X-ray diffraction studies (powder X-ray diffraction, single crystal X-ray diffraction, variable-temperature single crystal X-ray diffraction and variable-temperature powder X-ray diffraction) and thermal analysis (thermogravimetric analysis, differential scanning calorimetry, and hot stage microscopy).
3. To perform porosity studies (liquid and gas sorption) on the synthesised compounds. This includes investigating the thermal stability and robustness of the activated (guest-free) compound.

1.12 References

1 J. M. Lehn, *Chem. Soc. Rev.*, 2007, **36**, 151–160.

2 D. Braga, *Chem. Commun.*, 2003, **22**, 2751–2754.

3 G. R. Desiraju, *Chem. Commun.*, 1997, **16**, 1475–1482.

4 G. R. Desiraju, *Angew. Chemie Int. Ed.*, 2007, **46**, 8342–8356.

5 B. Moulton and M. J. Zaworotko, *Chem. Rev.*, 2001, **101**, 1629–1658.

6 G. R. Desiraju, *J. Am. Chem. Soc.*, 2013, **135**, 9952–9967.

7 R. Mondal, M. K. Bhunia and K. Dhara, *CrystEngComm*, 2008, **10**, 1167–1174.

8 S. R. Batten, N. R. Champness, X.-M. Chen, J. Garcia-Martinez, S. Kitagawa, L. Öhrström, M. O'Keeffe, M. P. Suh and J. Reedijk, *CrystEngComm*, 2012, **14**, 3001–3004.

9 S. R. Batten, N. R. Champness, X. M. Chen, J. Garcia-Martinez, S. Kitagawa, L. Öhrström, M. O'Keeffe, P. M. Suh and J. Reedijk, *Pure Appl. Chem.*, 2013, **85**, 1715–1724.

10 S. K. Ghosh, J. P. Zhang and S. Kitagawa, *Angew. Chemie Int. Ed.*, 2007, **46**, 7965–7968.

11 H. Jiang, T. A. Makal and H. Zhou, *Coord. Chem. Rev.*, 2013, **257**, 2232–2249.

12 S. Kitagawa and R. Matsuda, *Coord. Chem. Rev.*, 2007, **251**, 2490–2509.

13 C. A. Bauer, T. V. Timofeeva, T. B. Settersten, B. D. Patterson, V. H. Liu, B. A. Simmons and M. D. Allendorf, *J. Am. Chem. Soc.*, 2007, **129**, 7136–44.

14 J. L. C. Rowsell and O. M. Yaghi, *Microporous Mesoporous Mater.*, 2004, **73**, 3–14.

15 A. Corma, H. Garcia and F. X. Llabres i Xamena, *Chem. Rev.*, 2010, **110**, 4606–4655.

16 Y. Kinoshita, I. Matsubara, T. Higuchi and Y. Saito, *Bull. Chem. Soc. Jpn.*, 1959, **32**, 1221–1226.

17 O. M. Yaghi and L. Hailian, *J. Am. Chem. Soc.*, 1995, **117**, 10401–10402.

18 M. C. Das, Q. Guo, Y. He, J. Kim, C. G. Zhao, K. Hong, S. Xiang, Z. Zhang, K. M. Thomas, R. Krishna and B. Chen, *J. Am. Chem. Soc.*, 2012, **134**, 8703–8710.

19 O. M. Yaghi, M. O'Keeffe, N. W. Ockwig, H. K. Chae, M. Eddaoudi and J. Kim, *Nature*, 2003, **423**, 705–714.

20 M. O'Keeffe, *Chem. Soc. Rev.*, 2009, **38**, 1215–1217.

21 S. Furukawa, Y. Sakata and S. Kitagawa, *Chem. Lett.*, 2013, **42**, 570–576.

22 M. Du, C. P. Li, C. Sen Liu and S. M. Fang, *Coord. Chem. Rev.*, 2013, **257**, 1282–1305.

23 L. Öhrström, *Crystals*, 2015, **5**, 154–162.

24 H. Li, M. Eddaoudi, M. O'Keeffe and O. M. Yaghi, *Nature*, 1999, **402**, 276–279.

25 L. J. Barbour, *Chem. Commun.*, 2006, 1163–1168.

26 J. L. Atwood, L. J. Barbour, A. Jerga and B. L. Schottel, *Science*, 2002, **298**, 1000–1002.

27 M. Eddaoudi, H. Li and O. M. Yaghi, *J. Am. Chem. Soc.*, 2000, **122**, 1391–1397.

28 H. Furukawa, N. Ko, Y. B. Go, N. Aratani, S. B. Choi, E. Choi, A. Ö. Yazaydin, R. Q. Snurr, M. O'Keeffe, J. Kim and O. M. Yaghi, *Science*, 2010, **329**, 424–428.

29 M. J. Lin, A. Jouaiti, N. Kyritsakas and M. W. Hosseini, *CrystEngComm*, 2011, **13**, 776.

30 M. Servati-Gargari, G. Mahmoudi, S. Batton, V. Stilinovic, D. Butler, L. Beauvais, W. S. Kassel, W. G. Dougherty and D. G. VanDerveer, *Cryst. Growth Des.*, 2015, **15**, 1336–1343.

31 H. Aggarwal, R. K. Das, P. M. Bhatt and L. J. Barbour, *Chem. Sci.*, 2015, **6**, 4986–4992.

32 S. Kitagawa, R. Kitaura and S. Noro, *Angew. Chemie Int. Ed.*, 2004, **43**, 2334–2375.

33 H. Aggarwal, P. M. Bhatt, C. X. Bezuidenhout and L. J. Barbour, *J. Am. Chem. Soc.*, 2014, **136**, 3776–3779.

34 D. Sun, S. Ma, Y. Ke, D. J. Collins and H. C. Zhou, *J. Am. Chem. Soc.*, 2006, **128**, 3896–3897.

35 E. Y. Choi, K. Park, C. M. Yang, H. Kim, J. H. Son, S. W. Lee, Y. H. Lee, D. Min and Y. U. Kwon, *Chem Eur. J.*, 2004, **10**, 5535–5540.

36 M. S. Chen, M. Chen, S. Takamizawa, T. Okamura, J. Fan and W. Y. Sun, *Chem. Commun.*, 2011, **47**, 3787–9.

37 A. Husain, M. Ellwart, S. A. Bourne, L. Öhrström and C. L. Oliver, *Cryst. Growth Des.*, 2013, **13**, 1526–1534.

38 S. Ma, D. Sun, M. Ambrogio, J. A. Fillinger, S. Parkin and H. C. Zhou, *J. Am. Chem. Soc.*, 2007, **129**, 1858–1859.

39 J. J. Zhang, L. Wojtas, R. W. Larsen, M. Eddaoudi and M. J. Zaworotko, *J. Am. Chem. Soc.*, 2009, **131**, 17040–17041.

40 L. Carlucci, G. Ciani, D. M. Proserpio, T. G. Mitina and V. A. Blatov, *Chem. Rev.*, 2014, **114**, 7557–7580.

41 Z. Su, M. Chen, T. Okamura, M. sheng Chen, S. Chen and W. Sun, *Inorg. Chem.*, 2011, **50**, 985–991.

42 B. Q. Ma, K. L. Mulfort and J. T. Hupp, *Inorg. Chem.*, 2005, **44**, 4912–4914.

43 B. Chen, N. W. Ockwig, A. R. Millward, D. S. Contreras and O. M. Yaghi, *Angew. Chemie Int. Ed.*, 2005, **117**, 4823–4827.

44 A. R. Millward and O. M. Yaghi, *J. Am. Chem. Soc.*, 2005, **127**, 17998–17999.

45 H. K. Chae, D. Y. Siberio-Pe´rez, J. Kim, Y. Go, M. Eddaoudi, A. J. Matzger, M. O'Keeffe and O. M. Yaghi, *Nature*, 2004, **427**, 523–527.

46 J.-P. Zhang, P.-Q. Liao, H.-L. Zhou, R.-B. Lin and X.-M. Chen, *Chem. Soc. Rev.*, 2014, **43**, 5789–5814.

47 A. G. Blanco, A. F. Vallone, A. Gil and K. Sapag, *Int. J. Hydrogen Energy*, 2012, **37**, 14870–14880.

48 M. Cao, H. Mo, J. Liang and B. Ye, *CrystEngComm*, 2009, **11**, 784–790.

49 J. P. Zhang, Y. Y. Lin, W. X. Zhang and X. M. Chen, *J. Am. Chem. Soc.*, 2005, **127**, 14162–14163.

50 D. Sarma and S. Natarajan, *Cryst. Growth Des.*, 2011, **11**, 5415–5423.

51 D. Xue, W. Zhang, X. Chen and H. Wang, *Chem. Commun.*, 2008, **13**, 1551–1553.

52 Y. J. Zhang, T. Liu, S. Kanegawa and O. Sato, *J. Am. Chem. Soc.*, 2009, **131**, 7942–7943.

53 M. K. Sharma and P. K. Bharadwaj, *Inorg. Chem.*, 2011, **50**, 1889–97.

54 S. K. Ghosh, W. Kaneko, D. Kiriya, M. Ohba and S. Kitagawa, *Angew. Chemie Int. Ed.*, 2008, **120**, 8975–8979.

55 H. A. Habib, J. Sanchiz and C. Janiak, *Dalton Trans.*, 2008, **13**, 1734–44.

56 R. Sen, D. Mal, P. Brandao, R. A. S. Ferreira and Z. Lin, *Cryst. Growth Des.*, 2013, **13**, 5272–5281.

57 M. Bosch, M. Zhang and H. Zhou, *Adv. Chem.*, 2014, **2014**, 1–8.

58 G. Xu and Y. Xie, *Acta Crystallogr. Sect.*, 2010, **C66**, 201–203.

59 Y. Bae, K. L. Mulfort, H. Frost, P. Ryan, S. Punnathanam, L. J. Broadbelt, J. T. Hupp and R. Q. Snurr, *Langmuir*, 2008, **24**, 8592–8598.

60 J. Luo, M. Hong, R. Wang, R. Cao, L. Han and Z. Lin, *Eur. J. Inorg. Chem.*, 2003, **14**, 2705–2710.

61 O. M. Yaghi, C. E. Davis, G. Li and H. Li, *J. Am. Chem. Soc.*, 1997, **119**, 2861–2868.

62 Z. Su, M. Chen, T. A. Okamura, M. S. Chen, S. S. Chen and W. Y. Sun, *Inorg. Chem.*, 2011, **50**, 985–991.

63 X. Zhu, P. Sun, J. Ding, B. Li and H. Li, *Cryst. Growth Des.*, 2012, **12**, 3992–3997.

64 Y. X. Ren, S. P. Chen, G. Xie, S. L. Gao and Q. Z. Shi, *Inorg. Chim. Acta*, 2006, **359**, 2047–2052.

65 X. L. Wang, B. Mu, H. Y. Lin, G. C. Liu, A. xiang Tian and S. Yang, *CrystEngComm*, 2012, **14**, 1001–1009.

66 D. L. Long, A. J. Blake, N. R. Champness and M. Schroder, *Chem. Commun.*, 2000, **22**, 2273–2274.

67 D. E. Wang, K. J. Deng, K. Le Lv, C. G. Wang, L. L. Wen and D. F. Li, *CrystEngComm*, 2009, **11**, 1442–1450.

CHAPTER 2: EXPERIMENTAL

The metal ions and organic linkers used for the synthesis of the MOFs in this study are identified in this chapter. The techniques and various instruments used to characterise these compounds are also discussed.

2.1 Starting Materials

The organic ligands (**Figure 2.1**), 1,3,5-benzenetricarboxylic acid (purity 95%), 1,2-bis(4-pyridyl)ethane (98% purity) and 4,4'-bipyridyl-*N*,*N'*-dioxide (98% purity) were purchased from Sigma Aldrich in Germany, while 5-nitro-1,3-benzenedicarboxylic acid (H_2nbdc) (purity >98%) was obtained from EGA-Chemie (Germany). Zinc(II) sulfate heptahydrate (purity >99.5%) was purchased from Hopkin and Williams Ltd in the United Kingdom and cadmium(II) nitrate tetrahydrate was obtained from Riedel-De Haën Ag. Seelze-Hannover in Germany. The solvents used for the synthesis of the MOFs included *N*,*N'*dimethylformamide (99.8% purity), ethanol (99% purity) and Milli-Q water.[1] *N,N'*-dimethylformamide and ethanol were purchased from Sigma Aldrich. All starting materials were used as received.

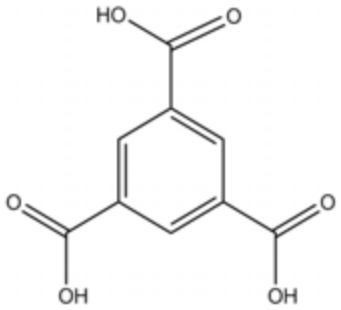

1,3,5-benzenetricarboxylic acid (H_3BTC)

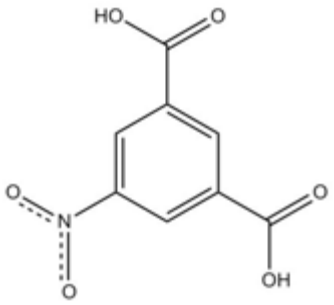

5-nitro-1,3-benzenedicarboxylic acid (H_2nbdc)

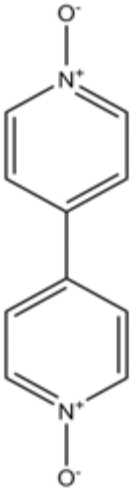

4,4'-bipyridine-*N*,*N*'-dioxide (4,4'-bpdo)

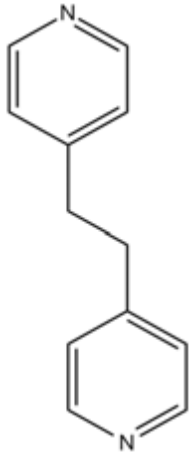

1,2-bis(4-pyridyl)ethane (bpe)

Figure 2.1: Chemical structures of organic ligands used

2.2 General Synthetic Procedure

Single crystals of MOFs were obtained using the solvothermal method for both compounds. The synthesis involved dissolving the ligands and metal ions in separate solvents before adding the solutions together. The mixed solutions were placed in vials and heated in the oven, followed by slow cooling of the solution which yielded the crystals. Full details on synthetic procedures will be discussed in the relevant chapters.

2.3 X-Ray Diffraction

2.3.1 Single Crystal X-Ray Diffraction (SCXRD)

A suitable crystal was removed from the mother liquor and covered in Paratone N oil[2] to prevent the loss of any solvent molecules and also simultaneously glue the crystal to a nylon loop (attached to a rigid mounting) at lower temperatures. The loop was then placed on the goniometer head under a cold stream of nitrogen gas. Single crystal X-ray data collections were carried out on a Bruker KAPPA APEX II Duo diffractometer utilizing MoKα (λ = 0.71069 Å) X-rays. These were produced by a Bruker K780 generator powered at 50 kV and 30 mA. Low temperatures for data collections were achieved by a constant stream of nitrogen gas at a flow rate of 20 cm^3 min^{-1} using a Cryostream cooler (Oxford Cryosystems, UK).

Unit cell refinement and data reduction were carried out using the program SAINT-Plus.[3] All intensity data were scaled and corrected for Lorentz-polarisation and absorption effects using the program SADABS.[4] The crystal system was established from the observed Laue symmetry of the diffraction pattern and the space group of the structures were determined from systematic absences in the X-ray intensity data and linking the observed result with the systematic absences of a known space group. The program XPREP[3] was used to confirm the space group of the structures and to prepare input files SHELXS-97 or SHELXT-97 for the structure solution programs using direct methods.[5] All non-hydrogen atoms were placed in the first electron density map and refined by full-matrix least-squares on F^2 method in SHELXL-2014/7.[5] The programs SHELXS-97, SHELXT-97 and SHELXL-2014/7

were accessed through the X-SEED or OLEX2 interface.[5–7] Full refinement details for each compound, including hydrogen atom placement, are given in the relevant chapters.

2.3.2 Powder X-Ray Diffraction (PXRD)

Powder X-ray diffraction (PXRD) and variable-temperature powder X-ray diffraction (VT-PXRD) measurements were performed using a Bruker D8 Advance diffractometer equipped with a Lynxeye detector using CuKα radiation (λ = 1.5406 Å). A spatula tip of crystals were removed from the mother liquor and dried on filter paper before being gently ground into a powder using a mortar and pestle. The sample was then placed onto a zero background sample holder and scanned over the 2θ range of 4° to 40° with a step size of 0.016° increments. X-rays were generated with a current flow of 40 mA and voltage of 30 kV.

Variable-temperature PXRD (VT-PXRD) experiments were used to determine whether the crystallinity of the compound was retained with an increase in temperature. This is required since it is desirable for the host framework to retain its structure upon solvent removal. The patterns obtained from VT-PXRD give an indication of long range order as well as the crystalline phase of the analysed material with an increase in temperature.

The fully refined structure coordinates were input into the program Mercury[8] to produce an idealised PXRD pattern (calculated pattern) of the structure. The calculated pattern is compared to the PXRD pattern obtained experimentally to determine whether the single crystal is representative of the bulk material. PXRD can also be used to conclude whether any bulk material obtained in subsequent experiments is that of the desired compound.

2.4 Thermal Analysis

Thermogravimetric analysis (TGA), differential scanning calorimetry (DSC) and hot stage microscopy (HSM) were used to measure and observe any physical events upon heating of the sample. These events include solvent loss and decomposition of the material.

2.4.1 Thermogravimetric Analysis (TGA)

Thermogravimetric experiments were used to determine the number of solvent molecules per asymmetric unit present in the crystal structure by measuring the percentage mass loss as a function of temperature. TGA was also used to determine the decomposition temperature, relating to the stability of the host framework. Approximately 2-5 mg of the sample was weighed and surface dried using filter paper. TGA experiments were performed using a TA-Q500 analyser from TA instruments with a heating rate of 10 °C min^{-1} under a dry nitrogen purge gas flow rate of 60 ml min^{-1}. Universal Analysis 2000 software was used to analyse results obtained from the TGA experiments.

2.4.2 Differential Scanning Calorimetry (DSC)

This technique was used to measure the difference in the heat flow between the sample and reference pans as a function of temperature with both pans' temperature changing at the same rate. This allows for the enthalpy of various thermal events to be determined. Approximately 2-5 mg of the sample was surface dried using filter paper before being placed in aluminium pans with two holes in the lid to allow for ventilation. Exothermic and endothermic reactions are presented on the DSC traces by peaks and trough peaks, respectively. DSC experiments were performed using a DSC-Q200 machine from TA instruments with a heating rate of 10 °C min^{-1} and nitrogen purge gas flowing at a rate of 60 ml min^{-1}. Results obtained from DSC experiments were analysed using Universal Analysis 2000 software.

2.4.3 Hot Stage Microscopy (HSM)

This technique is used to observe visual changes which are not directly observable by TGA or DSC, such as colour changes, bubbling due to solvent loss, melting and decomposition of the sample. In this research project, HSM was mostly used to observe solvent loss and decomposition temperatures. The temperature of thermal events observed in HSM experiments were slightly different from those observed in TGA and DSC, due to the different geometries of the experimental setups. For example, HSM experiments do not involve a flow of purge gas over the sample. Therefore, different temperatures are observed

in the HSM, TGA and DSC experiments. HSM was performed by placing the sample on a cover slip under silicon oil and viewed with a Nikon SMZ-10 stereoscopic microscope fitted with a Linkam THMS600 hot stage and a Linkam TP92 temperature control unit. The thermal events were captured with a real-time Sony Digital Hyper HAD colour video camera and images were viewed with the Soft Imaging System program analySIS.[9] All samples were heated at a rate of 10 °C min^{-1}.

2.5 Cogrinding Experiments

Cogrinding experiments offer a quick, easy, alternative approach for the preparation of MOFs. Adequate amounts of the pure material for wide range testing (e.g. gas and solvent sorption experiments) could easily be obtained using this method, which sometimes proves to be challenging when using common synthetic routes.[10] In addition, this method generally produces quantitative yields of the final product in powder form. It should be noted that the material produced *via* the cogrinding method might not be the same as the product formed *via* the solvothermal method. The characterisation of the material obtained is carried out by comparison of the PXRD pattern of the coground material with the calculated pattern obtained from SCXRD. Alternatively, a different MOF may be produced.[10] A combination of reactants i.e. metal, ligand 1, ligand 2 (and a few drops of DMF to assist with the grinding) were coground in a stoichiometric ratio using a mortar and pestle for approximately 20 minutes. The products of each combination were analysed by PXRD to investigate whether the desired MOFs could be produced using this method.

2.6 Fourier Transform Infrared (FT-IR) Spectroscopy

FT-IR experiments were used to compare the absorption bands of the ligands coordinated to the metal in the MOF with that of the free ligands (a shift to a lower wavenumber would be expected for the coordinated ligands) and to compare coordination modes of the ligands. IR absorption bands were measured in the range 4000-650 cm^{-1} on a Perkin Elmer Spectrum One FT-IR spectrometer using attenuated total reflectance (ATR).

2.7 Elemental Analysis (EA)

Elemental analysis was performed in order to determine the percent carbon, hydrogen, nitrogen and sulfur in the sample using a Fisons EA1108 CHNS-O Elemental Analyser. The results obtained from EA were compared with compound compositions determined from single crystal X-ray diffraction.

2.8 Liquid Sorption

Liquids of varying polarities were chosen to investigate the porosity of the MOFs. Burdick and Jackson solvents are arranged in order of increasing polarity index, which is a relative measure of the degree of interaction of the solvent with various polar test solutes.[11] Solvent sorption studies involved placing the compound into small vials and exposing it to roughly 2 ml of solvent for 24 hrs. Solvents chosen for the experiments (with polarity indices) included toluene (2.4), tetrahyrofuran (4.0), chloroform (4.1), 1,4-dioxane (4.8), methanol (5.1) and dimethylformamide (6.4).[11]

2.9 Gas and Water Vapour Sorption

Gas sorption studies were performed to investigate the ability of the MOFs to absorb gases such as carbon dioxide and nitrogen. In addition, water vapour sorption experiments were also performed on the compounds. These experiments were carried out using a Micromeritics 3Flex Surface Area Analyzer. Approximately 150–200 mg of sample was treated in a Micromeritics Flowprep with a constant flow of nitrogen gas over the sample for at least 24 hours and heating at 60 °C in order to evacuate the framework of any solvent. Furthermore, the sample was heated at 60 °C under vacuum *in situ* before starting the analysis. This ensured the removal of any solvent still present in the compound as an empty framework was required for the analysis. A Micromeritics water bath was used for experiments performed at 273 K, while liquid nitrogen was used for experiments performed at 77 K. To perform gas sorption experiments at 195 K, a mixture of acetone and dry ice was used to obtain the low temperature. Complete details of both gas and water vapour sorption experiments, including Brunauer-Emmett-Teller (BET) parameters, are given in the relevant sections.

2.10 Computer Packages

The Cambridge Structural Database (CSD) was accessed *via* ConQuest and used to determine whether structures that were synthesised were novel.[12] The program X-SEED was used as an interface for additional programs such as LAYER and POV-RAY.[13,14] LAYER was used to study systematic absences from the intensity data collected in order to visually confirm the space group suggested by XPREP.[3] Molecular structure and crystal packing images were generated by MERCURY and POV-RAY. Molecular parameters were calculated using the program PLATON.[15] MERCURY was also used to calculate the free void space (with a probe radius of 1.2 Å and grid spacing of 0.7 Å) present in the host framework.

2.11 Appendices

Results obtained from thermal experiments (TGA and DSC) as well as data obtained from single crystal X-ray studies can be found in attached appendices.

Table 2.1: Crystallographic data files that can be found in the Appendices

File Extensions	Contents
.hkl	Reflection data
.cif	Crystallographic information data
.res	SHELX coordinate data
.lis	PLATON output file
.lst/.xl	SHELX output file
.sup	Tabulated supplementary data
.pdf	CheckCif Report
.fcf	Observed and calculated intensities

2.12 References

1 Milli-Q Water, Millipore Corporation, Billerica, Massachusetts*, USA*.

2 Paratone N oil (Exxon Chemical Co., Texas, USA).

3 Bruker (2007), *Bruker AXS Inc., Madison, Wisconsin USA*, 2007, **1**.

4 G. M. Sheldrick, *SADABS, Version 2.05,* University of Göttingen*,* Germany, 2007.

5 G. M. Sheldrick, *Acta Crystallogr. Sect. A: Found. Crystallogr.*, 2008, **64**, 112–122.

6 L. J. Barbour, *J. Supramol. Chem.*, 2001, **1**, 189–191.

7 O. V. Dolomanov, L. J. Bourhis, R. J. Gildea, J. A. K. Howard and H. Puschmann, *J. Appl. Crystallog.*, 2009, **42**, 339–341.

8 C. F. Macrae, I. J. Bruno, J. A. Chisholm, P. R. Edgington, P. McCabe, E. Pidcock, L. Rodriguez-Monge, R. Taylor, J. Van De Streek and P. A. Wood, *J. Appl. Crystallogr.*, 2008, **41**, 466–470.

9 Soft Imaging System GmbH, *Digital Solutions for Imaging and Microscopy*, Version 3.1 for Windows (Copyright 1987-2000).

10 M. Klimakow, P. Klobes, A. F. Thünemann, K. Rademann and F. Emmerling, *Chem. Mater.*, 2010, **22**, 5216–5221.

11 Burdick and Jackson solvents, *Polarity Index*, <http://macro.lsu.edu/howto/solvents/Polarity%20index.htm>, (accessed 20 October 2016)

12 Cambridge Structural Database and Cambridge Structural Database System, Version 5.37, Cambridge Crystallographic Data Centre, University Chemical Laboratory, Cambridge, 2016.

13 L. J. Barbour, *J. Appl. Crystallogr.*, 1999, **32**, 351–352.

14 C. Cason, T. Froehlich, N. Kopp and R. Parker, POV-Ray for Windows, Version 3.631aicl8.win32, The Persistence of Version Raytracer Pty. Ltd., 2003.

15 A. L. Spek, *Acta Crystallogr. Sect. D: Biol. Crystallogr.*, 2009, **65**, 148–155.

CHAPTER 3: $[Zn_3(BTC)(4,4'\text{-bpdo})(OH)(SO_4)(H_2O)_3]_n \cdot n(H_2O)_{2.33}$ (1)

A novel mixed-ligand, 2D MOF was prepared using zinc(II), 4,4'-bipyridine-*N*,*N*'-dioxide (4,4'-bpdo) and 1,3,5-benzenetricarboxylic acid (H_3BTC) as the starting materials. The 2D MOF has a molecular formula of $[Zn_3(BTC)(4,4'\text{-bpdo})(OH)(SO_4)(H_2O)_3]_n \cdot n(H_2O)_{2.33}$ (**1**) and was fully characterised using X-ray diffraction studies (SCXRD, VT-SCXRD, PXRD and VT-PXRD), thermal analysis (TGA, DSC and HSM), Fourier transform infrared spectroscopy and elemental analysis. Gas and water vapour sorption experiments were performed in order to investigate the porosity of the compound. VT-PXRD along with SCXRD results confirmed that dehydration and rehydration of the framework were reversible and occurred *via* single-crystal-to-single-crystal transformations.

3.1 Synthesis

The metal salt, $ZnSO_4 \cdot 7H_2O$ (27 mg, 0.095 mmol), was dissolved in 2 ml H_2O. In a separate vial, the organic linkers 4,4'-bipyridyl-*N*,*N*'-dioxide (18 mg, 0.095 mmol) and 1,3,5-benzenetricarboxylic acid (20 mg, 0.095 mmol) were dissolved in a solvent mixture of 1 ml H_2O, 3 ml ethanol and 3 ml *N*,*N*'-dimethylformamide (DMF). Both solutions were heated while stirring and the clear solutions were combined and left in the oven at 90 °C for 17 hours. Clear, triangular crystals were obtained after slow cooling for 7 hours.

3.2 Single Crystal X-Ray Diffraction Analysis

3.2.1 Structure Solution and Refinement

A single crystal of **1** was removed from the mother liquor and immediately placed in Paratone N oil, before being mounted on a nylon loop. Single crystal X-ray diffraction (SCXRD) data collections were carried out on a Bruker DUO APEX II CCD diffractometer at 104 K (SCXRD data presented in table 3.1). Unit cell refinement and data reductions were carried out using SAINT-Plus.[1] Structure solution and refinement were performed using the crystallographic suite OLEX2.[2] The structure was solved using direct methods in SHELXT-97.[3] The initial space group suggested by XPREP[1] was $P3_1$ for the structure. However, structure solution and refinement yielded an *R*-factor of ~20%. Visual inspection of the reciprocal lattice using the program LAYER[4] revealed a considerable number of systematic absences for

the space group $P3_1$ and also indicated a rhombohedral lattice centring. The space group *R*3 was forced even though a significant percentage of systematic absence violations were observed (~23%) for this space group. The structure was then refined to ~7% with high peaks present around the metal centres and F_o » F_c for reflections with $l = 3n$. The unusual diffraction pattern that was observed along with the F values seemed to be consistent with a case of obverse/reverse twinning.[5] The TwinRotMat routine in PLATON[6] recommended the twin law [0 -1 0 -1 0 0 0 0 -1] and a twin fraction estimation of 0.15. Additional refinement was done on the structure by applying this twin law and twin fraction and yielded an *R*-factor of ~4% with a refined twin fraction of 0.184(3) for the minor component as well as the absence of peaks close to the metal centres. However, a peak of 2.49 occurred close to the solvent molecule, which could still possibly be due to twinning that occurred in the structure, despite that it was treated for this phenomenon.

The hydrogen atoms in **1** were placed in idealised positions using a riding model. The hydrogen atoms were assigned temperature factors 1.2 times that of the parent atom for hydrogen atoms attached to carbon atoms as well as the hydrogen of the hydroxide ion and 1.5 times that of the parent atom for water hydrogen atoms.

3.2.2 Structure Description

Compound **1** crystallises in the trigonal crystal system in the space group *R*3. The asymmetric unit (ASU) of **1** consists of three Zn(II) cations, one bridging, fully deprotonated 1,3,5-benzenetricarboxylate (BTC) ligand, one 4,4'-bipyridine-*N*,*N*'-dioxide (4,4'-bpdo) ligand, one capping sulfate anion, a bridging hydroxide ion and 5.33 water molecules (**Figure 3.1**). Water molecules labelled O1W, O2W and O3W are coordinated to the zinc metal centres, while water molecules O4W, O5W and O6W are uncoordinated. Water molecule O5W resides on a three-fold rotation axis and thus has a site occupancy factor (sof) of 1/3, while O6W is disordered over two positions (labelled O6WA and O6WB) with sofs of 0.69 and 0.31, respectively.

Zn01 has an octahedral coordination geometry and is coordinated to the O2 and $O3^{ii}$ atoms of two different BTC ligands, the O7 atom of the 4,4'-bpdo ligand, the O1S atom of the sulfate group, the O9 atom of the hydroxide ligand and the O3W atom of a water molecule. Angles present around Zn01 are in the range of a regular octahedron. The angle between

the bridging hydroxide group, sulfate ligand and Zn01 (O9-Zn01-O1S) lies almost at an exact right angle at 90.9(2)°.

Zn02 also has an octahedral coordination environment. It is ligated to the O1 and O6^{i} oxygen atoms of two different BTC ligands, the O3S atom of the sulfate ligand, the O9 atom of the hydroxide group and to the O1W and O2W atoms of two different water molecules. The angles around Zn02 are also in the range of a regular octahedron. The angle that forms between Zn02 with the hydroxide group and sulfate ligand (09-Zn02-03S) is 91.9(2)°.

Zn03 has a tetrahedral coordination geometry and is ligated to the O4^{ii} and O5^{i} atoms of two different BTC ligands, the O2S atom of the sulfate ligand and the O9 atom of the hydroxide ligand. The angles around Zn03 are in the range of a regular tetrahedron. The angle between O9-Zn03-O2S is 97.8(2)°, which is slightly larger than O9-Zn01-O1S and O9-Zn02-O3S angles. All bond angles related to **1** can be found in Appendix A.

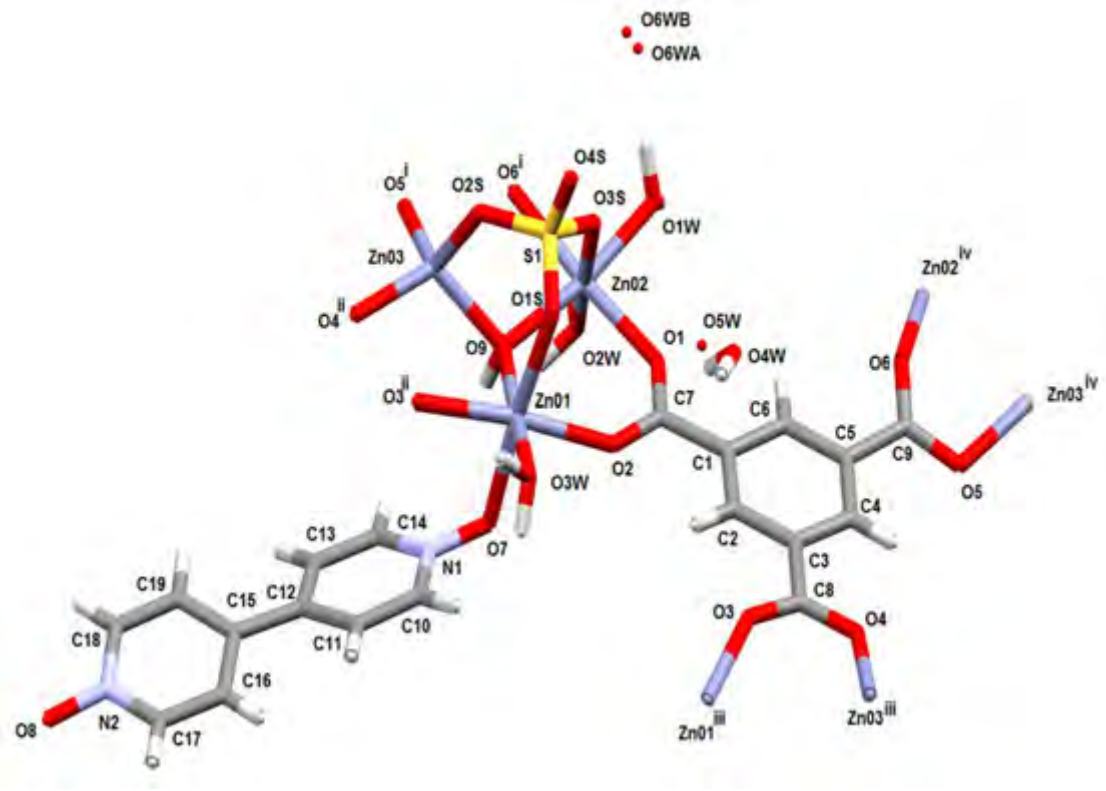

Figure 3.1: Basic chemical unit of **1** showing the coordination environments around the unique Zn(II) centres

Related by symmetry: ^{i}1+y-x, 1-x, z; ^{ii}1-y, 1+x-y, z; ^{iii}y-x, 1-x, z, ^{iv}1-y, x-y, z

The Zn01-O bond lengths, which were obtained from PLATON, range from 2.037(4)-2.158(4) Å, the Zn02-O bond lengths range from 2.056(5)-2.179(5) Å and the Zn03-O bond lengths range from 1.939(5)-1.990(5) Å. These values are close to those reported in the literature for similar complexes.[7–9] Selected bond lengths are summarised in table 3.2. All bond lengths related to **1** can be found in Appendix A.

The charges of the three Zn(II) cations add up to 6+ which are counter-balanced one fully deprotonated BTC ligand (3-), one sulfate ion (2-) and one hydroxide ion (1-). The three unique Zn(II) metal centres form a triangular arrangement bridged by the oxygen atom of the hydroxide ligand, six oxygen atoms of three carboxylate groups from different BTC ligands and three oxygen atoms from the single sulfate ion. This arrangement forms the secondary building unit $[Zn_3(COO^-)_3OH^-SO_4^{2-}]$. Although three metal centres linked by a hydroxide ion and capped by a single sulfate anion has been observed in a number of structures, whilst three metal centres bridged by carboxylate groups has been reported in other structures, a motif where three metals are linked by three carboxylate groups, a hydroxide ion and a capping sulfate ion, as observed in **1** has not yet been reported in the CSD.[10]

Table 3.1: Crystal data and refinement parameters of **1** at 104 K

Empirical formula	$C_{19}H_{20}N_3O_{18.3}SZn_3$
Formula weight (g mol^{-1})	2393.62
Temperature (K)	104
Wavelength (Å)	0.71073
Crystal system	Trigonal
Space group	*R*3
a (Å)	18.816
b (Å)	18.816
c (Å)	21.441
α (°)	90
β (°)	90
γ (°)	120
Volume (Å^3)	6574(3)
Z	9
Calculated density, ρ (g cm^{-3})	1.814
μ (mm^{-1})	2.598
***F* (000)**	3606
Crystal size (mm^3)	0.47 x 0.34 x 0.32
2θ Range scanned (°)	4.33 – 61.34
Index range	-25 ≤ h ≤ 25, -26 ≤ k ≤ 19, -29 ≤ l ≤ 30
No. reflections collected	19838
No. unique reflections	7900
R_{int}	0.0233
Data/Restraints/Parameters	7900/2/408
Goodness-of-fit on F^2	1.071
Final *R* indices [I>2σ(*I*)]	R_1=0.0383, wR_2=0.1085
***R* indices (all data)**	R_1=0.0394, wR_2=0.1090
$\Delta\rho_{min,max}$ (e Å^{-3})	2.49, -0.69
Flack parameter	0.01(5)
Refined minor twin component fraction	0.180(2)

Table 3.2: Selected bond lengths (Å) around Zn(II) metal centres in **1**

Bond	Bond length (Å)	*Literature bond length (Å)	Bond type
Zn01-O9	2.065(4)	1.990, 2.089, 2.096[7]	μ_3-OH
Zn02-O9	2.079(4)		
Zn03-O9	1.978(4)		
Zn01-O2	2.037(4)	2.033 ± 0.05[7]	Zn-Carboxylate
Zn01-O3^{ii}	2.134(4)		
Zn02-O6^{i}	2.179(5)		
Zn02-O1	2.056(5)		
Zn03-O4^{ii}	1.939(5)		
Zn03-O5^{i}	1.940(6)		
Zn01-O3W	2.093(4)	2.097 ± 0.05[7]	Octahedral Zn Terminal H_2O
Zn02-O1W	2.091(5)		
Zn02-O2W	2.104(5)		
Zn01-O1S	2.158(4)	2.071(2)-2.150(2)[8]	Zn···O-S
Zn02-O3S	2.069(4)		
Zn03-O2S	1.990(5)		
Zn01-O7	2.097(4)	2.063(3)-2.109(3)[9]	Zn···O-N

*From selected literature examples of similar complexes[7-9]

3.2.3 Crystal Packing

The coordination bonds that form in compound **1** lead to the formation of a 2D MOF. The Zn-BTC 2D layers are capped with the sulfate and 4,4'-bpdo ligands on opposite sides of the 2D layer (**Figure 3.2**). These layers stack along the *c*-direction, with the sulfate and 4,4'-bpdo ligands on the same sides, illustrating the polar arrangement of the crystal structure as required by the polar space group *R*3 (**Figure 3.3**). The extension of the 2D network along the *ab*-plane is determined by the three carboxylate groups of the BTC ligands, which if the centroids of the three trigonally arranged Zn(II) ions are taken as one node and the centroid of the BTC ligands are taken as the other type of node, form a honeycomb uninodal net of type 3*c* (3-connected) and is shown in **Figure 3.4**. The 4,4'-bpdo ligands are arranged in groups of three, extending at an angle of approximately 21° with respect to the Zn-BTC layer to form a unique, flat, bowl-shaped structure (**Figure 3.5**).

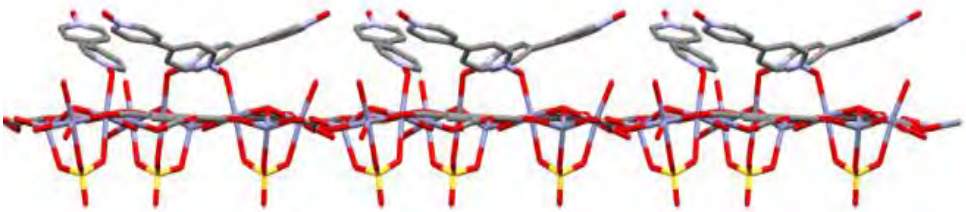

Figure 3.2: Side view of 2D network showing sulfate and 4,4'-bpdo ligands on opposite sides

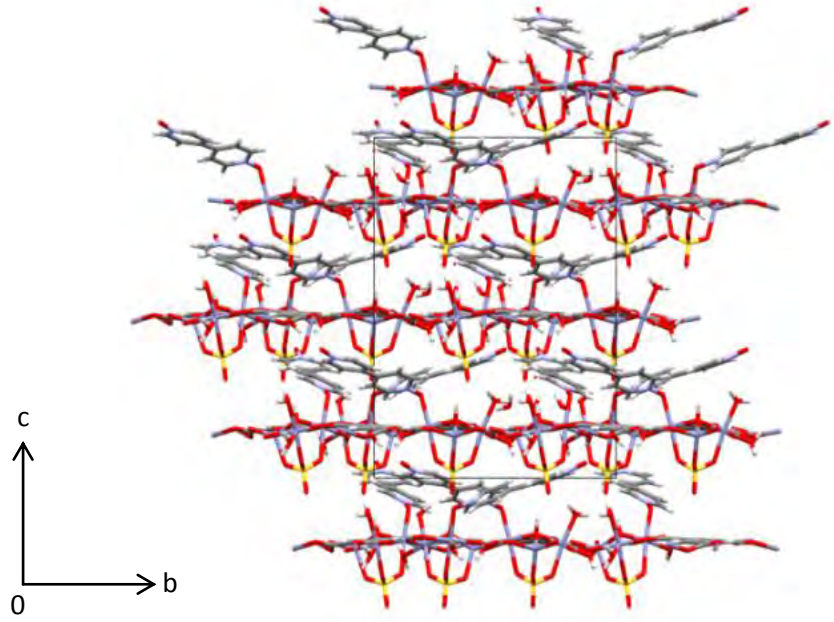

Figure 3.3: View of **1** along the *a*-axis illustrating polar stacking arrangement along the *c*-axis

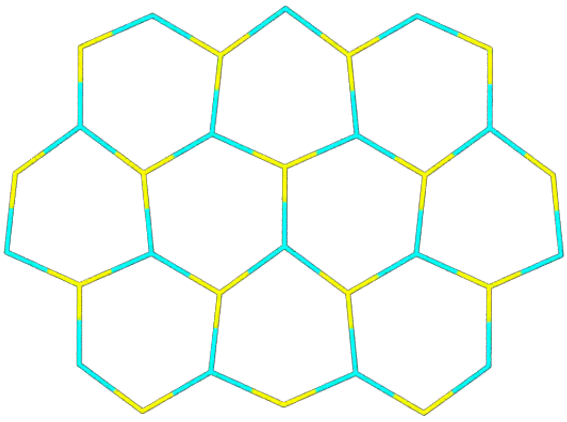

Figure 3.4: Honeycomb motif formed by the nodes taken at the centroid of the metal clusters (blue) and BTC ligands (yellow), respectively

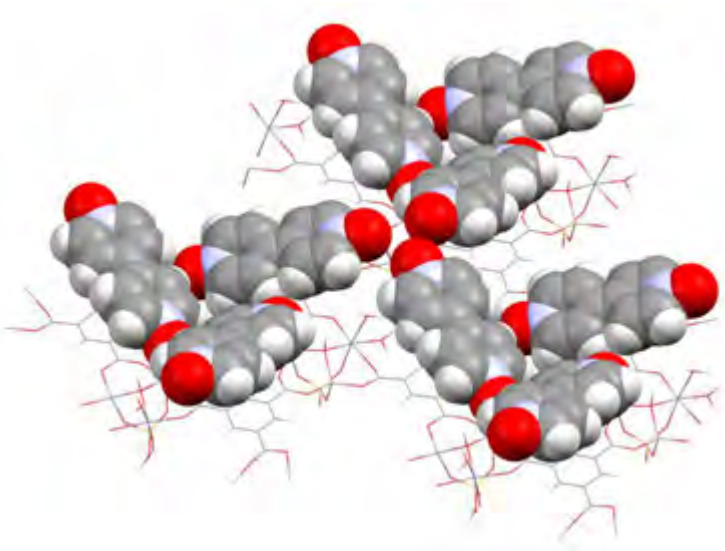

Figure 3.5: Oblique view of the 2D layer showing the "flat" bowl formed by three trigonally arranged 4,4'-bpdo ligands in compound **1**

Mercury[11] revealed that the 2D network contained isolated cavities and that the total potential solvent area volume (with uncoordinated water molecules artificially deleted) is 1004.18 $Å^3$ which equates to 15.3% of the total unit cell volume (6574 $Å^3$) as shown in **Figure 3.6**.

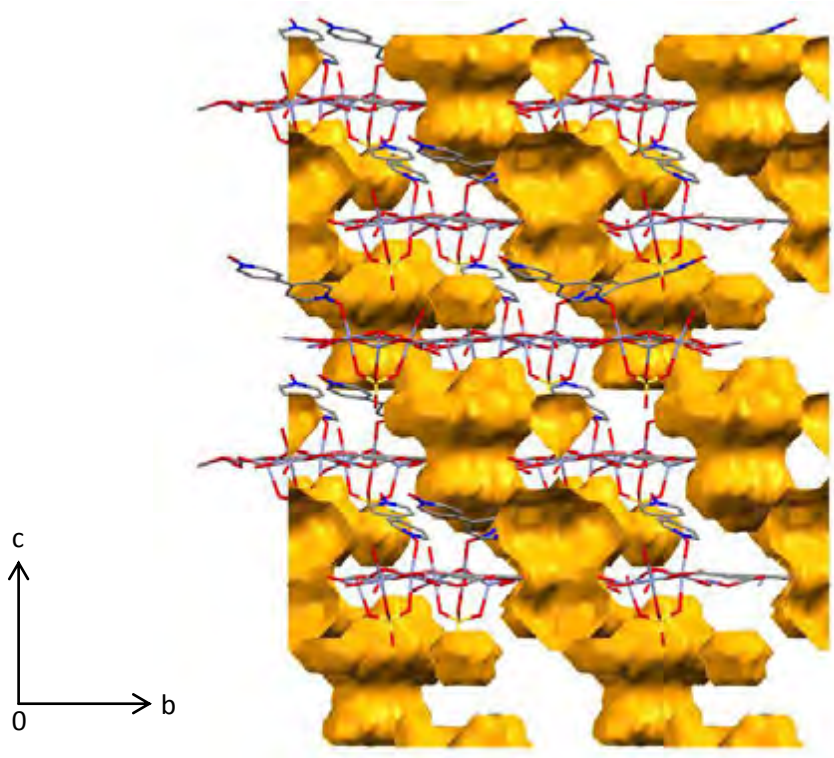

Figure 3.6: Crystal packing of **1** showing isolated voids in the 104 K along *c*-axis (uncoordinated water molecules artificially deleted)

3.2.4 Hydrogen Bonding

It was found that interactions between the solvent molecules, as well as solvent-host interactions, are present in the crystal structure (**Figure 3.7**). The uncoordinated water molecules interact with each other through hydrogen bonding (O4W-H4WA···O5W), while hydrogen bonding interactions between the uncoordinated water molecules (O4W and O6WA/B) and the framework occur *via* O4W-H4WB···O1 and O1W-H1WA···O6WA/B. Graph sets are used to define patterns of hydrogen bonded arrays. Assigning graph sets start with identifying the hydrogen bonds present in the specific structure. The designator for motifs produced by intermolecular hydrogen bonds, in this case, is R (ring) and the number of acceptors and donors are represented by a superscript and a subscript, respectively. The size of the motif corresponds to the number of atoms in the repeat unit and is shown in parentheses.[12]

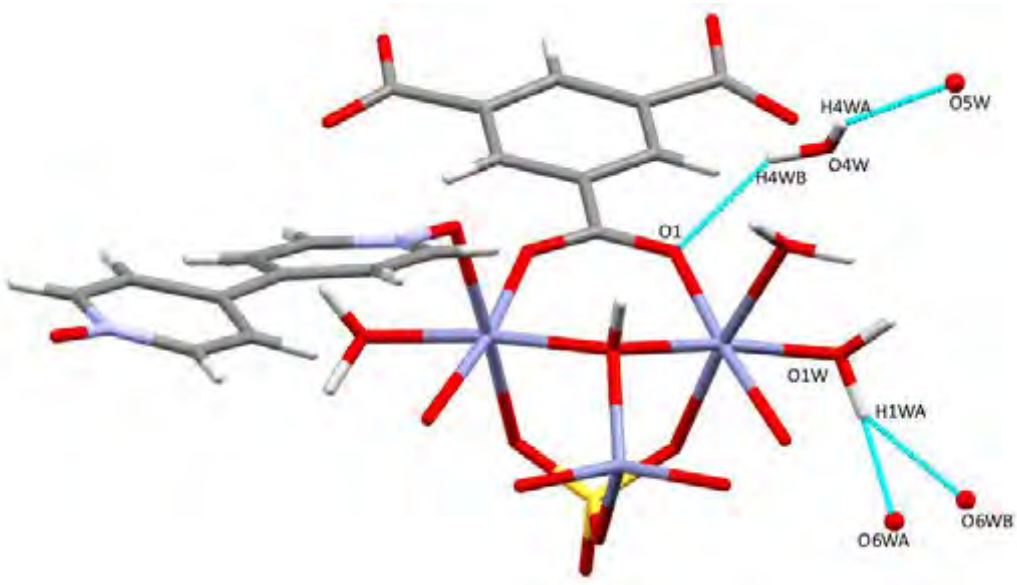

Figure 3.7: Hydrogen bonding in the structure of **1** showing uncoordinated water molecules interacting with each other and with the framework

Hydrogen bonding also occurs between the 4,4'-bpdo ligand and a coordinated water molecule (O3W-H3WB···O8), which forms a hydrogen-bonded ring motif of $R_3^3(12)$ due to the three fold rotation axis. The 2D layers are hydrogen bonded to each other *via* O3W-H3W···O8 and *via* the hydroxide ion and coordinated water molecule hydrogen bonding to a sulfate ion (O9-H9···O4S and O2W-2WB···O4S) shown in **Figure 3.8**. This arrangement forms a hydrogen-bonded ring motif with graph set notation $R_2^1(6)$. Selected hydrogen bond angles and distances present in **1** are shown in table 3.3.

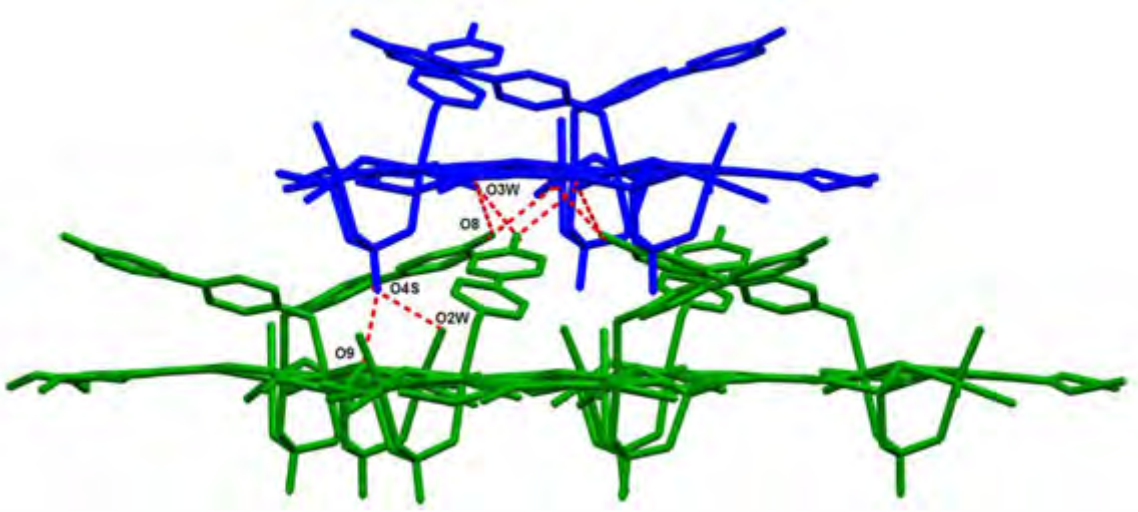

Figure 3.8: Hydrogen bonding that occurs between two adjacent 2D layers in **1**

Table 3.3: Hydrogen bonding parameters in the crystal structure of **1**

Donor – H···Acceptor	D-H (Å)	H···A(Å)	D···A (Å)	D – H···A (°)
O1W-H1WA···O6W	0.97	1.75	2.71	171
O1W-H1WB···O4W	0.97	2.03	2.94	157
O2W-H2WA···O4W	1.02	1.90	2.73	136
O2W-H2WB···O4S	1.02	1.75	2.70	153
O3W-H3W···O8	0.95	1.82	2.76	171
O4W-H4WA···O5W	0.87	2.08	2.78	137
O4W-H4WB···O1	0.87	2.09	2.84	144
O9-H9···O4S	1.00	1.83	2.79	159

3.3 Variable-Temperature X-Ray Diffraction Experiments

3.3.1 Variable-Temperature Powder X-Ray Diffraction

Ground crystals were placed on a sample holder and the temperature was increased from 30–190 °C. The patterns obtained at the higher temperatures (100–190 °C) show that the crystallinity of the compound is retained as the temperature increases (**Figure 3.9**). The crystalline phase also remains the same throughout the temperature range, indicating that the 2D MOF structure is retained.

The pattern obtained at 30 °C confirmed that the bulk material was a match to that of the calculated pattern. An artefact peak at 2θ position 4.5° occurs for all the PXRD patterns

taken from 30–190 °C and is due to the heating stage of the Bruker D8 Advance powder X-ray diffractometer. Slight changes in the VT-PXRD pattern include the peak at 2θ position 11.6° in the calculated pattern, which has a higher intensity at temperatures 170 °C and 180 °C (depicted in **Figure 3.9**). According to VT-PXRD studies, the compound is stable up to 190 °C before crystallinity is lost and the compound becomes amorphous.

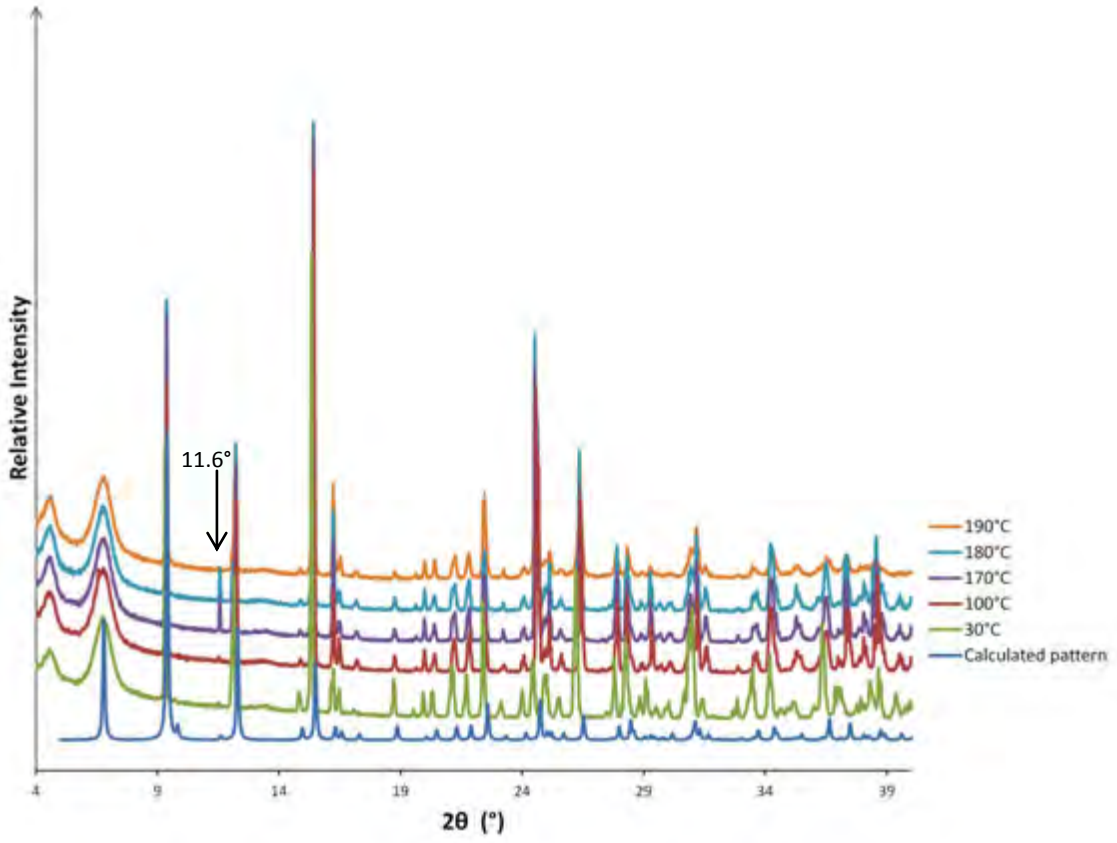

Figure 3.9: Variable temperature PXRD of **1** from 30–190 °C

3.3.2 Variable-Temperature Single Crystal X-Ray Diffraction

A single crystal of **1** was subjected to consecutive data collections at 104 K, 298 K, 323 K and 373 K in order to ascertain whether structural changes can be monitored upon solvent loss (SCXRD data presented in table 3.4). The 104 K structure was described in **section 3.2**. The space group *R*3 was also used for the higher temperature structures with their corresponding refined twin fractions being in close agreement. Variable-temperature single crystal X-ray diffraction (VT-SCXRD) analysis showed subtle differences in the ASU of **1** at higher temperatures to that of the 104 K structure. The main difference was the loss of water molecules from the structure as the temperature was increased.

As discussed in **section 3.2.2**, 5.33 water molecules were modelled in the 104 K structure (3 coordinated and 2.33 uncoordinated water molecules). In the 298 K structure, electron density peaks were present in the same positions as the O5W and O6WA water molecules in the 104 K structure, but could not be refined satisfactorily due to high isotropic temperature factors, this being most likely due to the sites not being fully occupied. Therefore, the sofs of the uncoordinated water molecules were refined freely with O4W, O5W and O6W refining to final values of 0.93, 0.13 and 0.34 respectively. The reader is reminded that O5W is on a 3-fold rotation axis and thus that a sof value of 0.33 represents full occupancy. In the 323 K structure, only one uncoordinated water molecule was modelled (O4W) with its refined sof value equal to 0.32. At 373 K, structure analysis revealed that all uncoordinated water molecules (O4W, O5W and O6W) as well as two coordinated water molecules (O1W and O2W) were absent from the crystal structure. The loss of O1W and O2W results in a change in coordination geometry around metal centre Zn02, from octahedral to tetrahedral with shortening of the distance between Zn02···Zn03 from 3.215(1) Å in the 104 K structure to 3.137(4) Å in the 373 K structure. Also, the hydroxide ligand oxygen atom was found to be closer to the Zn02 metal centre in the 373 K structure (1.989(6) Å) than in the 104 K structure (2.079(4) Å). Overlays of the ASU of **1** at 104 K with those of the higher temperatures are shown in **Figure 3.10** and reveal a near identical match. According to Mercury, the root-mean-square deviation for the 298 K, 323 K and 373 K overlays with the ASU of **1** at 104 K is 0.0474 Å, 0.0645 Å and 0.156 Å, respectively.[11] This trend indicates that an increasing difference occurs with an increase in temperature as the structure loses water molecules. Nevertheless, the resulting conformational changes are small.

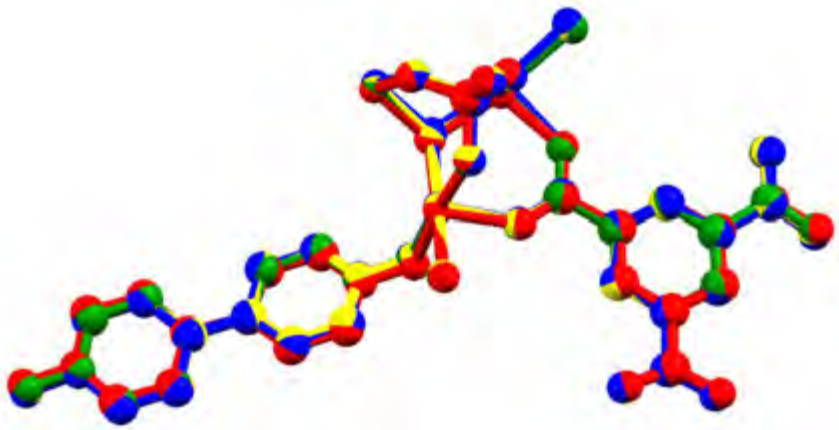

Figure 3.10: Overlay of ASU of **1** at 104 K (blue) with the ASUs of the 298 K (yellow), 323 K (green) and 373 K (red) structures, respectively

Table 3.4: Crystal Data and refinement parameters of **1** at 104 K, 298 K, 323 K and 373 K

	104 K	**298 K**	**323 K**	**373 K**
Empirical formula	$C_{19}H_{20}N_2O_{18.33}SZn_3$	$C_{19}H_{18}N_2O_{17.4}SZn_3$	$C_{19}H_{18}N_2O_{16.32}SZn_3$	$C_{19}H_{14}N_2O_{14}SZn_3$
Formula weight (g mol^{-1})	2393.62	2326.82	2290.93	2167.47
Temperature (K)	104	298	323	373
Crystal system	Trigonal	Trigonal	Trigonal	Trigonal
Space group	*R*3	*R*3	*R*3	*R*3
a (Å)	18.816(4)	18.798(19)	18.795(18)	18.889(19)
b (Å)	18.816(4)	18.798(19)	18.795(18)	18.889(19)
c (Å)	21.441(5)	21.57(2)	21.47(2)	21.67(2)
α (°)	90	90	90	90
β (°)	90	90	90	90
γ (°)	120	120	120	120
Volume (Å^3)	6574(3)	6602(15)	6568(14)	6695(15)
Z	9	9	9	9
ρ (g cm^{-3})	1.814	1.756	1.738	1.613
μ (mm^{-1})	2.598	2.581	2.591	2.532
***F* (000)**	3606	3497	3443	3240
Crystal size (mm^3)	0.47 x 0.34 x 0.31	0.47 x 0.34 x 0.32	0.47 x 0.34 x 0.32	0.47 x 0.34 x 0.32
2θ Range scanned (°)	4.33 – 61.336	4.33-61.748	3.14-61.81	3.12-60.796
Index range	-25 ≤ h ≤ 25, -26 ≤ k ≤ 19, -29 ≤ l ≤ 30	-25 ≤ h ≤ 26, -26 ≤ k ≤ 20, -29 ≤ l ≤31	-25 ≤ h ≤ 26, -26 ≤ k ≤ 21, -29 ≤ l ≤ 31	-22 ≤ h ≤ 26, -24 ≤ k ≤ 25, -29 ≤ l ≤ 30
No. reflections collected	19838	20095	20037	13265
No. unique reflections	7900	7886	7879	7012
R_{int}	0.0233	0.0301	0.0383	0.0476
Data/Restraints/ Parameters	7900/2/408	7888/1/390	7879/1/378	7012/1/354
Goodness-of-fit on F^2	1.071	1.081	1.066	1.024
Final *R* indices [I>2σ(*I*)]	R_1=0.0383, wR_2=0.1085	R_1=0.0519, wR_2=0.1465	R_1=0.0482, wR_2=0.1347	R_1=0.0508, wR_2=0.1377
***R* indices (all data)**	R_1=0.0394, wR_2=0.1090	R_1=0.0608, wR_2=0.1524	R_1=0.0539, wR_2=0.1372	R_1=0.0635, wR_2=0.1473
$\Delta\rho_{min,max}$ (e Å^{-3})	2.49, -0.69	1.22, -0.67	1.00, -0.88	0.97, -0.50
Flack parameter	0.001(5)	0.057(6)	0.016(7)	-0.002(11)
Refined minor twin component fraction	0.180(2)	0.186(1)	0.185(3)	0.188(1)

Figure 3.11 shows an overlay of the packing arrangement of **1** at 104 K and 373 K. Although the uncoordinated water molecules (O4W, O5W, O6W) and two coordinated water molecules (O1W and O2W) are absent in the 373 K structure, the overlay indicates that the two crystal structures are in close agreement. As discussed in **section 3.2.3**, Mercury revealed that the channels present in the network are not continuous and the void space is made up of isolated cavities. This was the case for the structures collected at the higher temperatures as well. The void space for the 373 K structure is shown in **Figure 3.12**. The voids are isolated even if the last coordinated water molecule (O3W) is artificially removed. Cooperative structural changes within the framework have to occur when the guest molecules are evacuated in order for monocrystallinity of **1** to be retained. These types of changes are referred to as dynamic structural changes and have been observed in single crystals.[13] Due to the low and high temperature structures being so similar, it was not evident how these changes occur. It is suggested that these changes are transient in that the "before" and "after" structural conformations are the same because they are energetically favoured. The void space per unit cell volume (as calculated by Mercury[11] with a 1.2 Å probe radius) for **1** at all four temperatures is presented in table 3.5, showing a slight increase in void space due to the structure being more dehydrated with an increase in temperature.

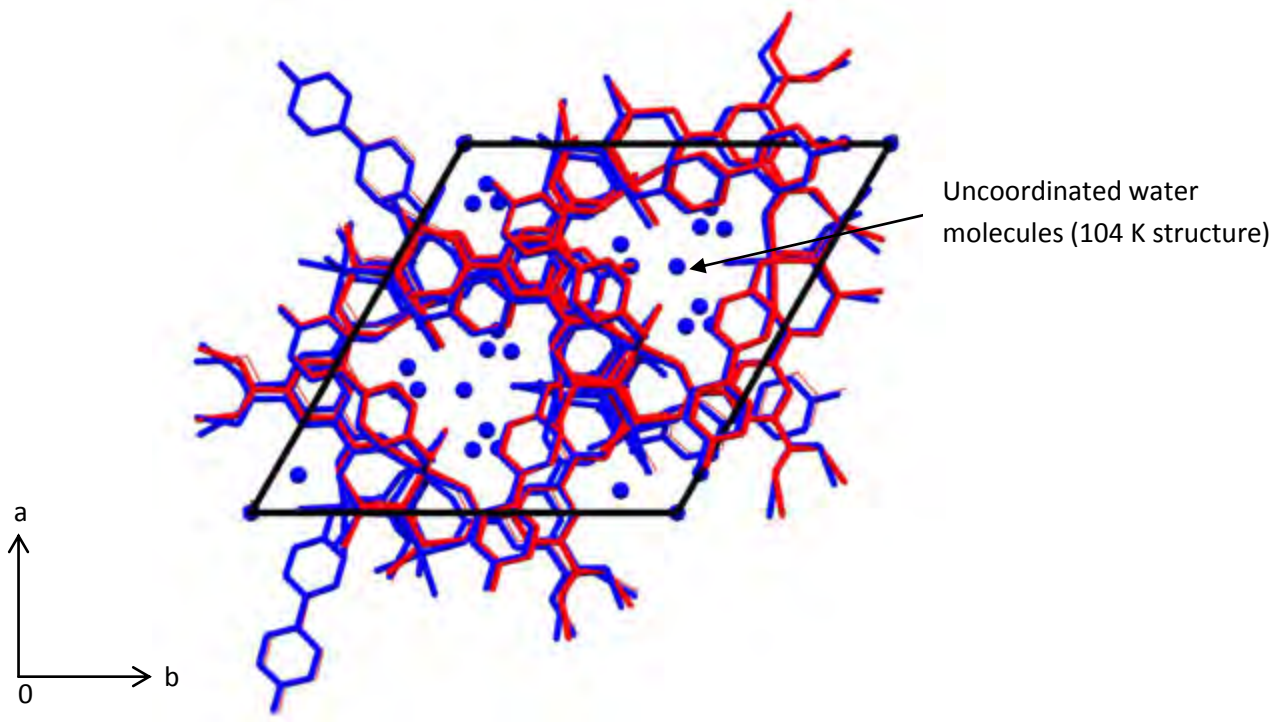

Figure 3.11: Overlay of packing arrangement of **1** at 104 K (blue) and 373 K (red) along the *c*-axis

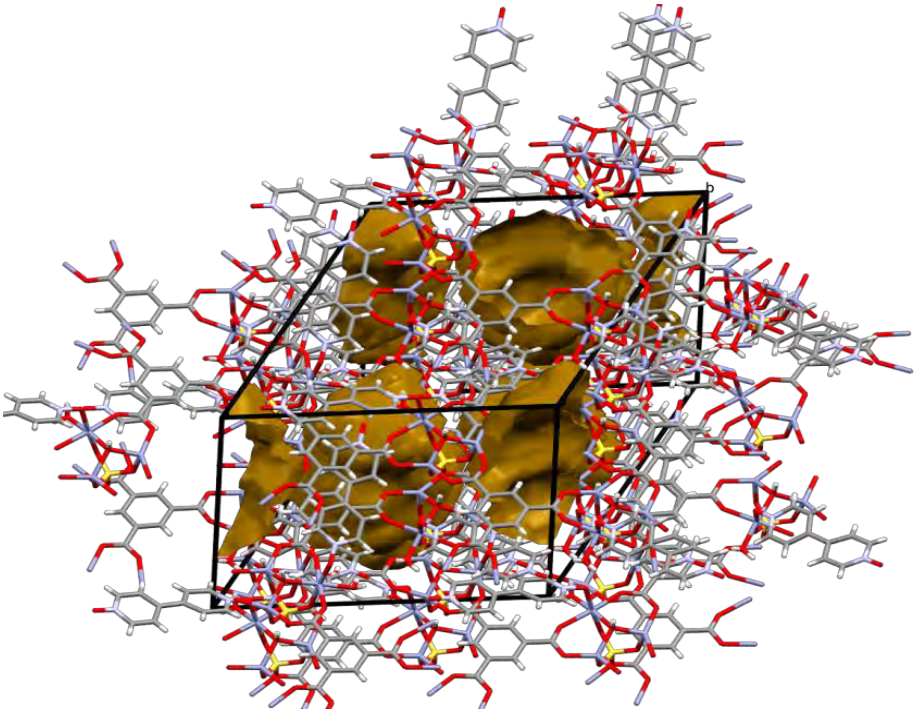

Figure 3.12: Crystal packing of **1** showing isolated voids in the 373 K structure

Table 3.5: Void space per unit cell volume of **1** at various temperatures

Temperature (K)	Void space per unit cell volume (Å^3)	Total unit cell volume (Å^3)	%	Water molecules present in structure
104	526.53	6574	8.0	O1W,O2W,O3W,O4W,O5W,O6WA/O6WB
298	714.83	6602	10.8	O1W,O2W,O3W,O4W,O5W,O6WA
323	934	6568	14.2	O1W,O2W,O3W,O4W
373	1599	6574	24.6	O3W

3.4 Thermal Analysis

3.4.1 Thermogravimetric and Differential Scanning Calorimetry Analysis

The thermal stability of **1** was investigated by thermogravimetric analysis (TGA) and differential scanning calorimetry (DSC) studies. **Figure 3.13** depicts the overlay of the thermograms for **1**. The TGA trace of the as-synthesised MOF shows a two-step mass loss. The initial mass loss of 9.81% occurs in the temperature range 30-150 °C and accounts for 4.25 water molecules. This corresponds to the 2.33 uncoordinated water molecules (O4W, O5W, O6W) and two coordinated water molecules O1W and O2W (O3W was still present in

the crystal structure at 373 K). The second mass loss of 2.57% was observed between 150-220 °C and accounts for 1.03 water molecules corresponding to the loss of the last coordinated water molecule O3W. DSC analysis displays two broad endotherms in the temperature range 50–150 °C and 150–220 °C which is in agreement with the mass losses observed in the TGA thermogram.

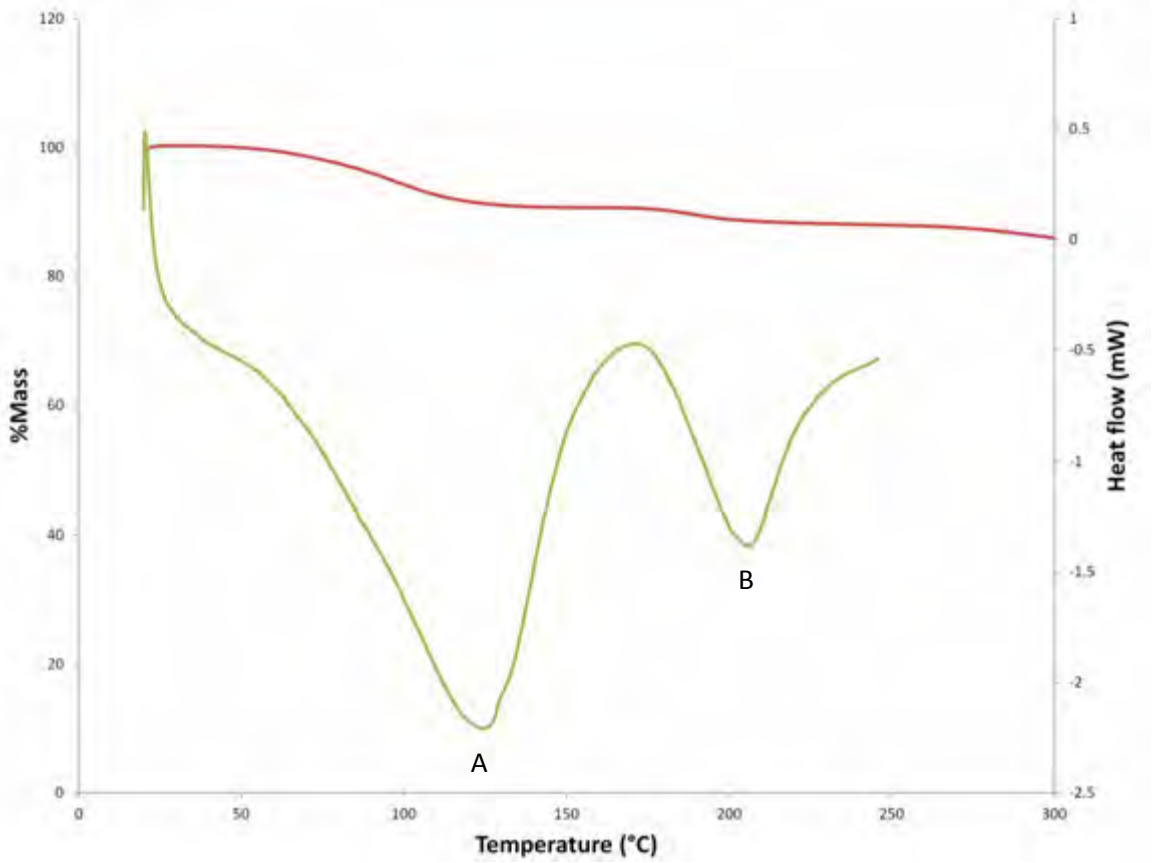

Figure 3.13: Overlay of TGA (red) and DSC (green) thermograms for **1**

The structure determinations of **1** at 104 K, 298 K, 323 K and 373 K (**section 3.2**) together with TGA suggests that the order of water release is O5W/O6W, O4W, O1W/O2W followed by O3W. The results obtained for TGA and DSC experiments are summarised in table 3.6 and table 3.7, respectively. The calculated and experimental values are in close agreement.

Table 3.6: TGA data obtained for **1**

Temperature range	**SCXRD water molecules**	**Experimental values**	**Calculated %mass loss**	**Experimental %mass loss**
30-150 °C	4.33 H_2O	4.25 H_2O	9.79	9.81
150-220 °C	1.00 H_2O	1.03 H_2O	2.56	2.57

Table 3.7: DSC data obtained for **1**

Peak	Temperature range	Enthalpy change	T_{onset}
A (Desolvation)	50-150 °C (endotherm)	248 $J.g^{-1}$	125.22
B (Desolvation)	150-220 °C (endotherm)	55.5 $J.g^{-1}$	205.99

3.4.2 Hot Stage Microscopy

The thermal events that were observed in hot stage microscopy (HSM) experiments occurred at slightly different temperatures than those in the TG and DSC analyses. This could be due to the different geometry of the experimental setup, nevertheless, the sequence of events remain the same. HSM studies provide a visual indication of the loss of solvent from the crystal structure as bubbles form when the crystals are heated in the range 25–300 °C (**Figure 3.14)**. The first sign of solvent loss occurs at 92 °C and continues up to 175 °C. Between this range, the crystal displays minor cracks but remains intact. According to VT-PXRD (**section 3.3.1**, **Figure 3.9**), the material is crystalline up to 190 °C and HSM provides a visual indication that the dehydration process is a SCSC transformation since the loss of crystallinity is usually associated with crystals becoming opaque. At 250 °C the crystals begin turning brown, indicating the onset of decomposition and by 284 °C the crystals are fully decomposed.

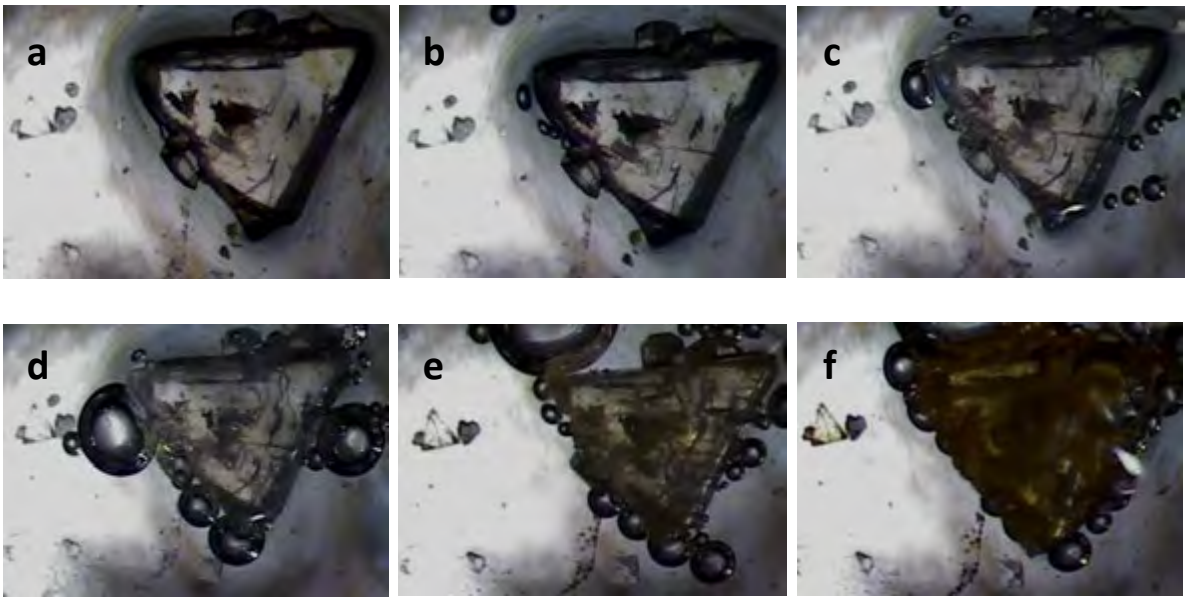

Figure 3.14: HSM images of **1** at **a)** 25 °C **b)** 92 °C **c)** 143 °C **d)** 175 °C **e)** 250 °C **f)** 284 °C

3.5 Dehydration and Rehydration Studies

In a separate experiment, as-synthesised crystals were subject to TGA in the temperature range 30–190 °C, the crystals were then cooled and immediately reheated to 190 °C. The TGA trace of these crystals showed no mass loss, indicating that there were no guest molecules present in the framework (**Figure 3.15**). The crystals were then placed in a small vial and submerged in a larger vial that contained water in order to create a humid atmosphere. After 24 hours, TGA was performed on the crystals which showed an 11.27% mass loss (30–150 °C), indicating that more water was absorbed than obtained from crystallisation (9.64% mass loss).

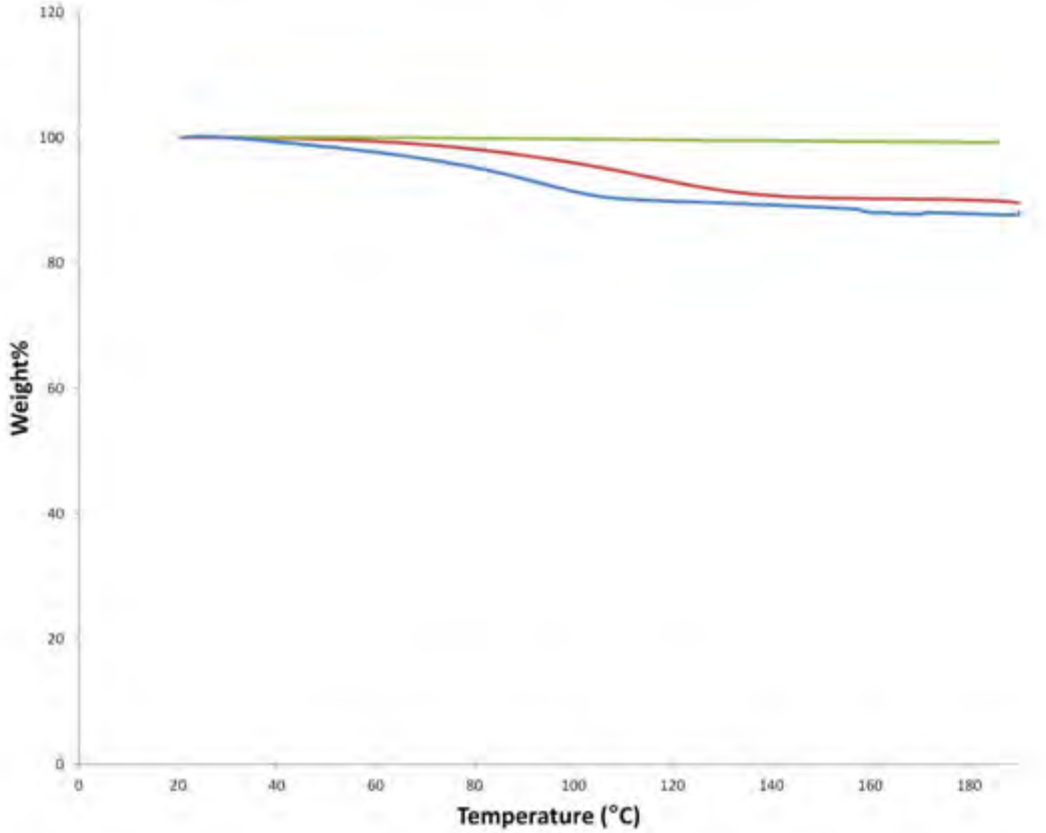

Figure 3.15: Traces of TGA for **1** up to 190 °C (red), immediately repeated run (green) and crystals exposed to water vapour for one day (blue)

In a separate experiment, a single crystal was removed from the mother liquor and covered in a small amount of Paratone N oil before being mounted on a nylon loop and subjected to a VT-SCXRD experiment. Results obtained from the first data collection at 373 K (over two hours) confirmed the absence of all the uncoordinated water molecules (O4W, O5W and O6W) and the two coordinated water molecules (O1W and O2W). The crystal was subsequently cooled to 298 K and a second data collection set immediately collected at this

temperature, which showed that the crystal structure at 298 K was nearly the same as that of the 373 K structure (**Figure 3.16**). The crystal was then left on the diffractometer at room temperature for 24 hours, with no dry air flowing over the crystal. The structure was re-determined at 298 K, which showed water molecules were partially reabsorbed to their original positions (O4W, O5W and O6W) with sof values equal to 0.40, 0.27 and 0.31 respectively. The partial reabsorption of the uncoordinated water molecules (sofs <100%) could be due to the barrier posed by the Paratone N oil in which the crystal was mounted. The coordinated water molecules (O1W and O2W) were also reabsorbed and coordinated to Zn02. In addition to the coordination geometry of Zn02 changing from tetrahedral back to octahedral, there was an increase in the bond distance between Zn02···Zn03 from 3.101(2) Å (dehydrated structure) to 3.218(2) Å (rehydrated structure). The hydroxide ion was also found to be closer to Zn02 in the dehydrated structure *vs*. the rehydrated structure (1.981(6) *vs*. 2.061(6) Å). The results obtained from this experiment proved that the SCSC dehydration of **1** is reversible. There are very few examples in the literature where the loss of coordinated water molecules in MOFs is reversible.[13,14] It was suggested by Su *et al*. that the loss of coordinated and uncoordinated water molecules in their cobalt 3D MOF was due to the existence of clear channels.[14] In compound **1** the lack of open channels does not seem to hinder the reversible loss of water molecules. It was noted that when the crystals were subjected to the TG experiments up to 190 °C (**section 3.4.1**), their monocrystallinity was lost. Visual indication of the loss of crystallinity was given by the crystals turning opaque at 190 °C during this TGA experiment as well as the VT-PXRD experiments. This suggested that in order for the dehydration of **1** to be a SCSC process, the presence of the coordinated water molecule O3W is required in the crystal structure.

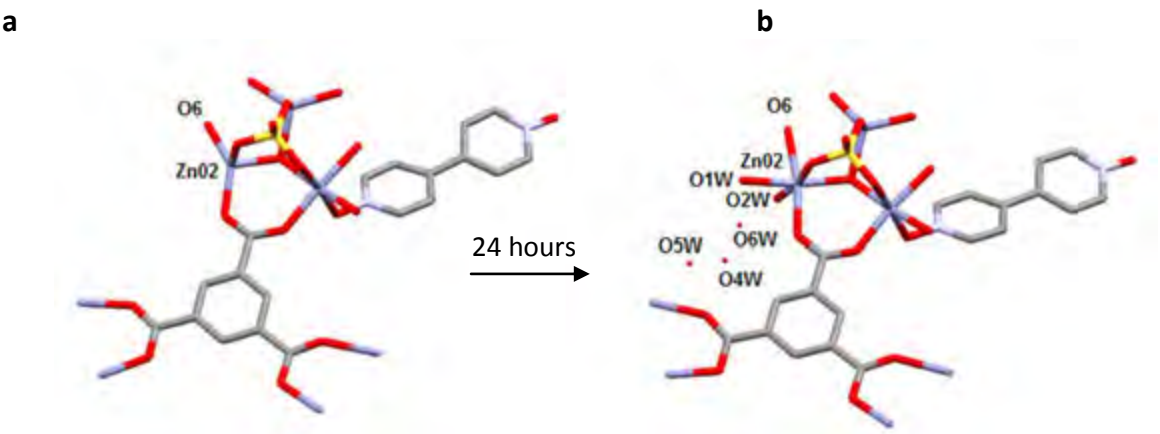

Figure 3.16: a) Structure of **1** after crystal was cooled from 373 K to cool 298 K **b)** structure of **1** after crystal was left on diffractometer for 24 hours at 298 K

3.6 Cogrinding Experiments

Cogrinding experiments were performed in order to determine whether **1** could be produced *via* mechanochemical synthesis (details of this method in **section 2.5**) since this method has the potential to produce high yields of the desired product. The experiment involved kneading of the organic ligands (4,4'-bpdo and H_3BTC) and metal salt ($ZnSO_4.7H_2O$) in a 1:1:1 ratio for 20 minutes using a mortar and pestle. A few drops of DMF were added to assist the kneading process. The characterisation of the resulting powder was carried out by comparison of the PXRD pattern of the material with the calculated pattern (**Figure 3.17**) from SCXRD studies (298 K). The pattern obtained for the kneaded material contained many extra peaks that were not found in the calculated pattern throughout the 4-40° two theta range.

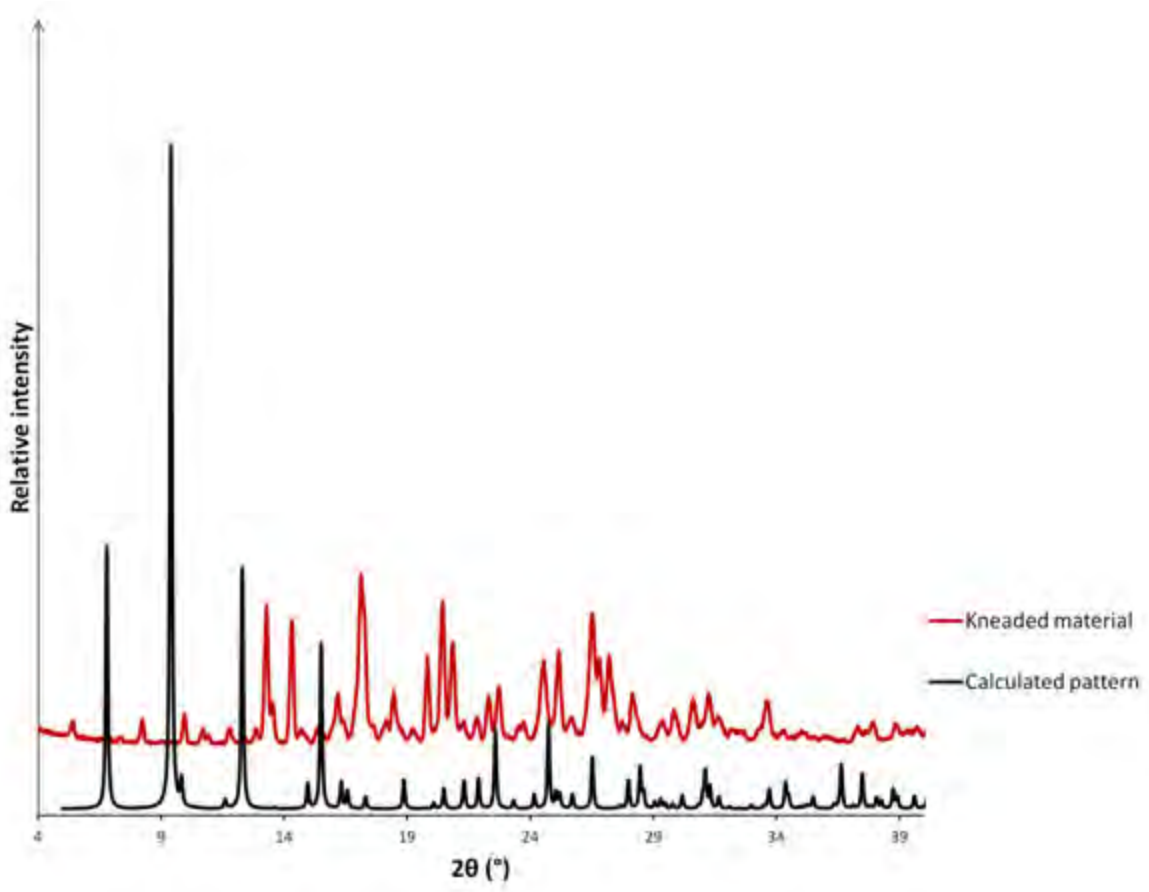

Figure 3.17: PXRD trace of kneaded material and calculated pattern of **1**

The PXRD pattern of the kneaded material was then compared to the patterns of the starting materials (**Figure 3.18**). Peaks present in the two theta region of 14.8-23° and 24.5-40° from the PXRD trace of $ZnSO_4.7H_2O$ matched that of the kneaded material. Overlapping of peaks occurred throughout the two theta range of 4-40° for the H_3BTC ligand. The few peaks present in the PXRD pattern of the 4,4'-bpdo ligand, which occurred at 2θ positions 12.1°, 21.0°, 25.6°, 26.7° and 30-40° also corresponded to the kneaded material, indicating that the kneaded material was a physical mixture of the starting materials. It was evident that **1** could not be produced *via* the cogrinding method.

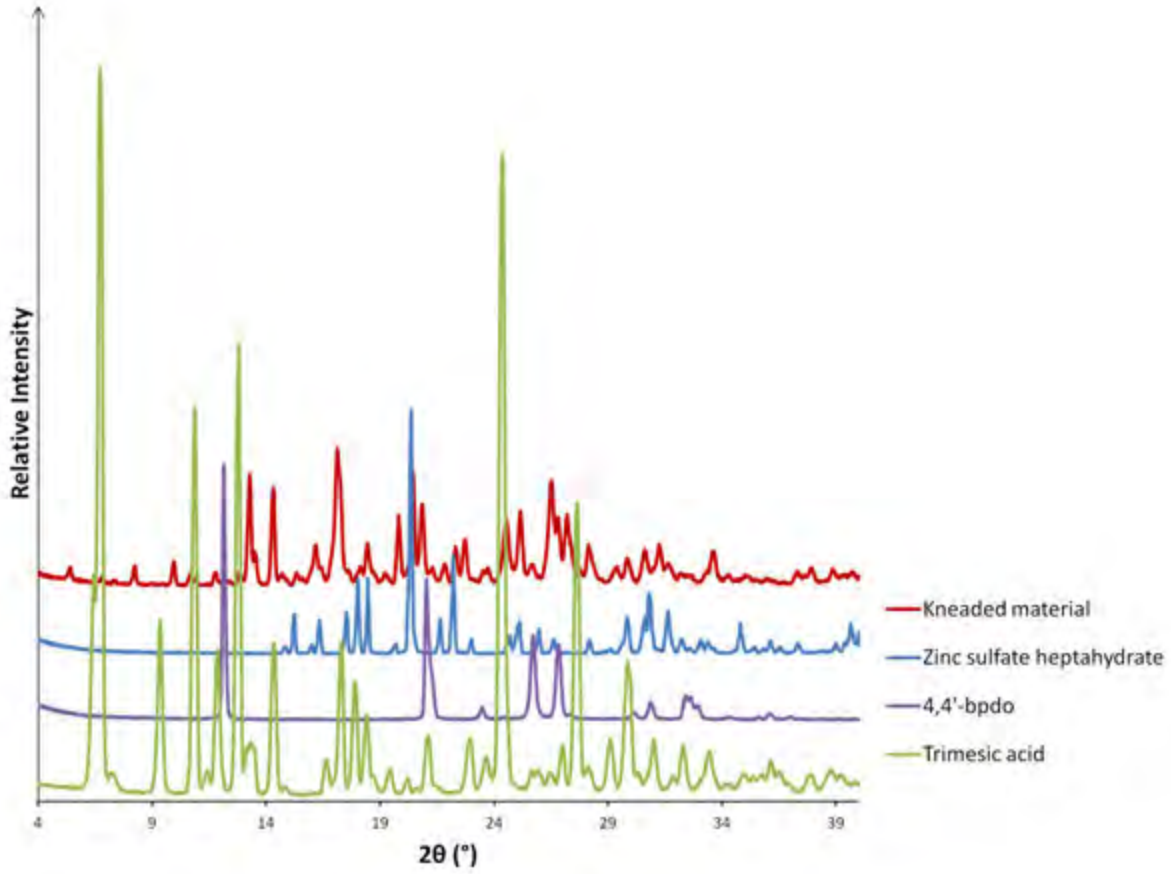

Figure 3.18: PXRD pattern of kneaded material and starting materials of **1**

3.7 Fourier Transform Infrared Spectroscopy

Fourier transform infrared (FT-IR) spectroscopy analysis provides evidence that the ligands are coordinated to the metal centres in **1** and also confirms the deprotonation of the carboxylic acid groups. A shift in the absorption bands to a lower wavenumber (compared to free ligand) is expected if the carboxylate functional groups are coordinated to the metal. The presence of the asymmetric stretching vibration mode, $\nu_{asym}(-COO^-)$, at 1622 cm^{-1} in the

IR spectrum of **1** (**Figure 3.19**) indicates that the BTC ligand is coordinated to the Zn(II) ions (1690 cm^{-1} in free ligand illustrated in **Figure 3.20**). The peak that occurs at 1473 cm^{-1} is due to the symmetric stretching vibrational mode, ν_s(-COO^-), with the difference between ν_{asym}(-COO^-) and ν_s(-COO^-) being 149 cm^{-1}. This result is consistent with a carboxylate group bridging two Zn(II) ions in a bidentate mode.[15] Proof that the carboxylic acid groups are fully deprotonated in the sample is also given by the absence of the shoulder on the peak at 1622 cm^{-1}, which indicates the absence of a hydroxyl hydrogen atom (specific to the carboxylic acid hydroxyl).[16] The N-O coordination bond to Zn(II) from the 4,4'-bpdo ligand is represented by the peak at 1220 cm^{-1},[15] which occurs at a lower frequency than the N-O bond in the free ligand (1235 cm^{-1} in **Figure 3.21**). The peak at 3260 cm^{-1} is accounted for by the presence of hydrogen-bonded lattice water molecules in the structure.

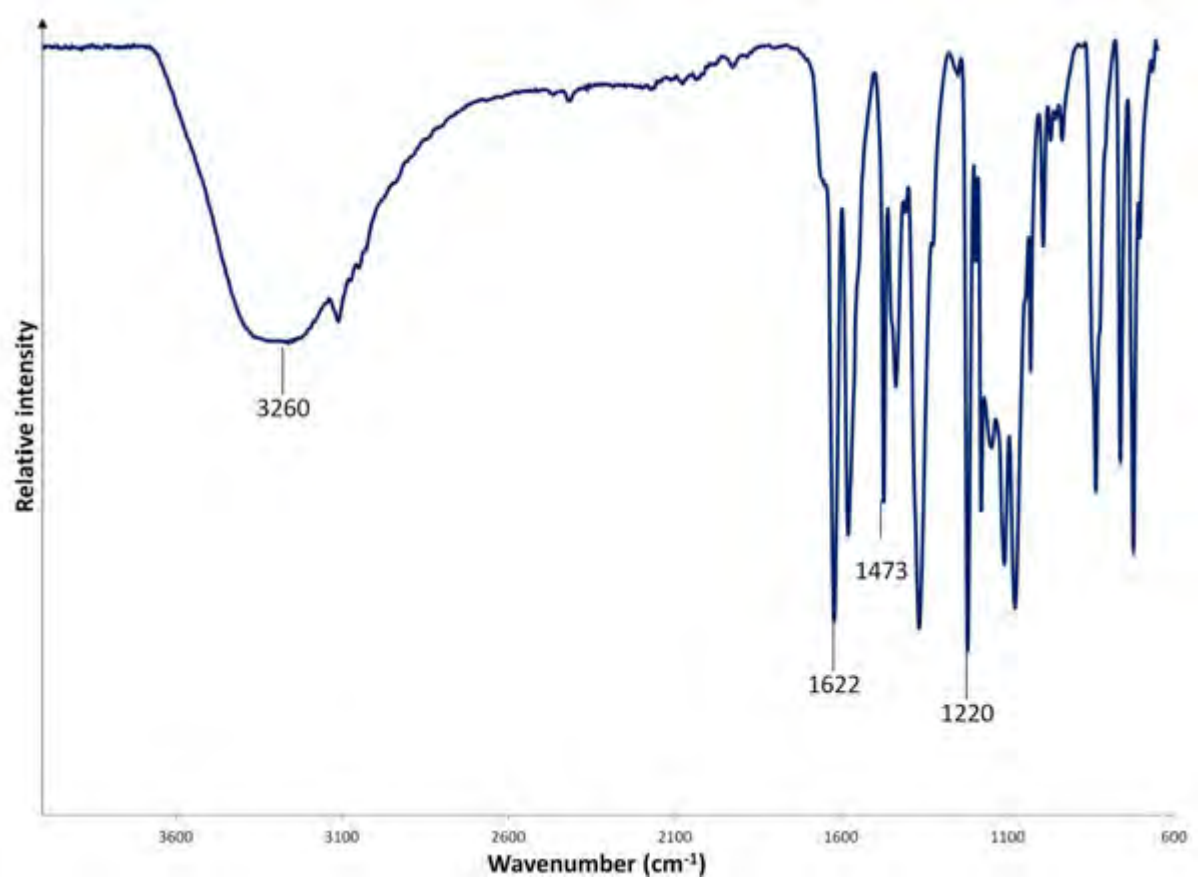

Figure 3.19: IR spectrum of **1**

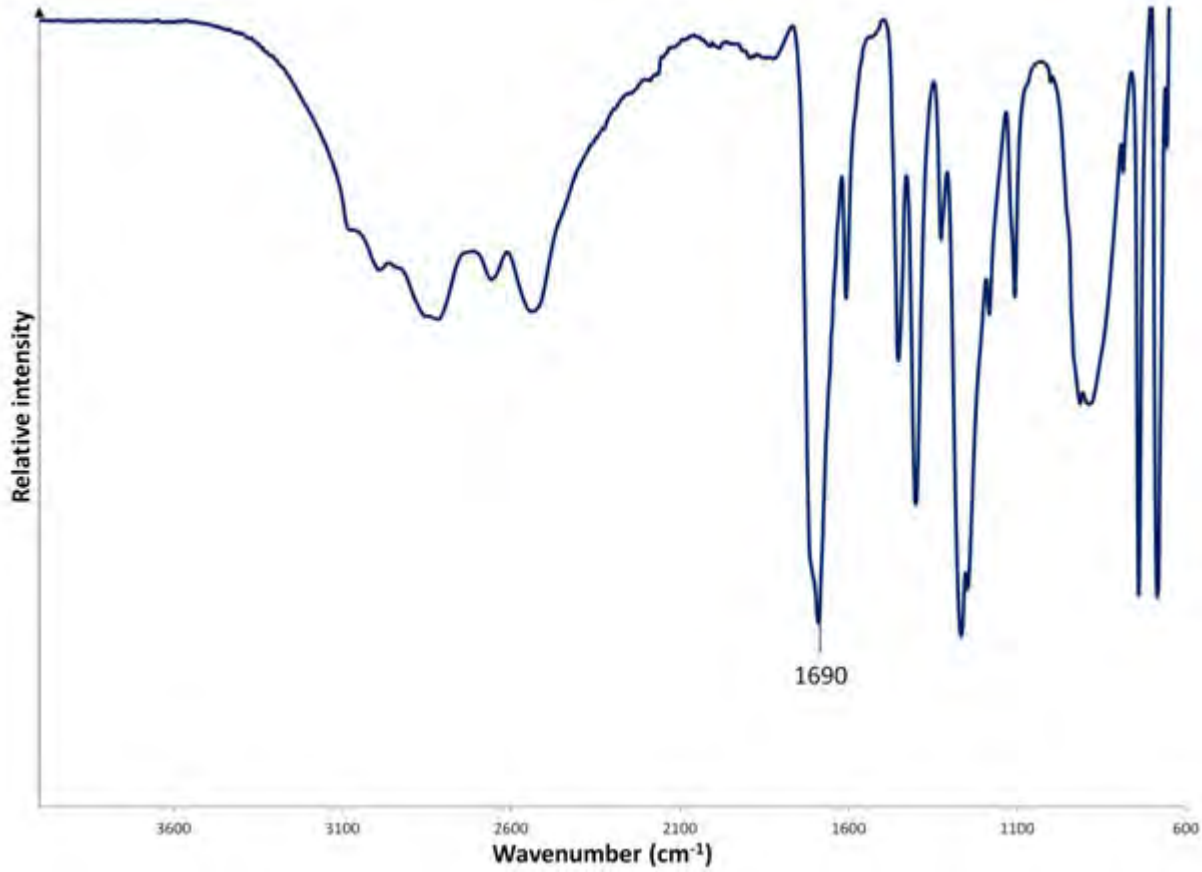

Figure 3.20: IR spectrum of 1,3,5 benzenetricarboxylic acid (H_3BTC)

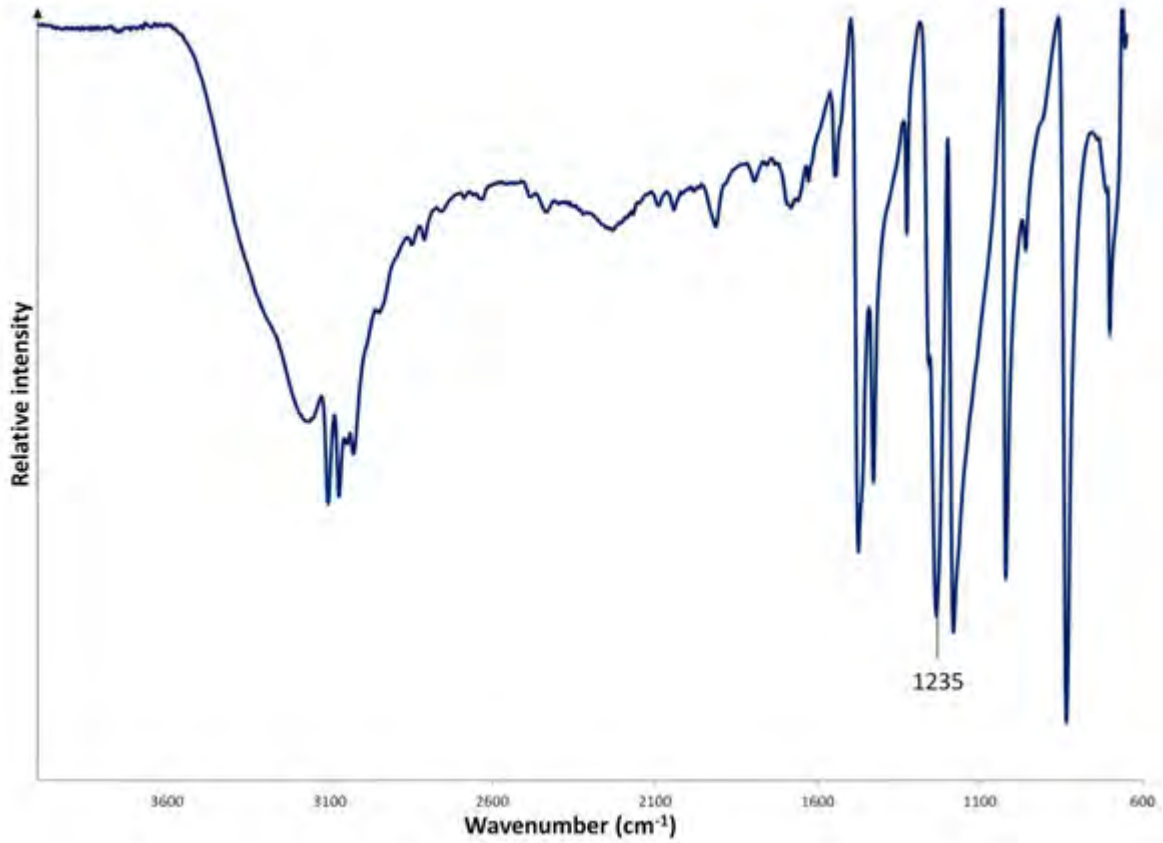

Figure 3.21: IR spectrum of 4,4'-bipyridine-*N*,*N*'-dioxide ligand (4,4'-bpdo)

3.8 Elemental Analysis

Crystals of as-synthesised compound **1** were subjected to elemental analysis (EA) to determine the percentage carbon, hydrogen, nitrogen and sulfur present in the as-synthesised structure. Prior to analysis, the crystals were rinsed with ethanol and dried using filter paper to get rid of any impurities that might be present on the surface of the compound. The results obtained from EA are a relatively good match. However, values for %C and %S deviate by 0.69 % and 0.51 % respectively, which is more than the general accepted value of 0.4% according to the Journal of Organic Chemistry.[17] Elemental analysis was repeated several times (n) on **1** with all the results being in close range of each other. Average values are given in table 3.8. Although there is a slight discrepancy between the calculated and experimental values, PXRD experiments validated the purity of the bulk sample.

Table 3.8: Elemental analysis results obtained for **1**

$[Zn_3(BTC)(4,4'bpdo)(OH)(SO_4)(H_2O)_3](H_2O)_{5.33}$	**Calculated values**	**Average Experimental values (n=4)**
%C	28.50	29.20
%H	2.85	3.24
%N	3.50	3.43
%S	4.01	3.52

3.9 Liquid Sorption Experiments

Various organic solvents were used to test whether water molecules present in **1** could be exchanged. The organic solvents with different polarities (P') included methanol (5.1), 1,4-dioxane (4.8), chloroform (4.1) and tetrahydrofuran (4.0). Experiments were conducted on **1** in an attempt to exchange the water molecules with the various organic solvents. These experiments were unsuccessful, indicating the strong affinity that **1** has for water.

3.10 Gas and Water Vapour Sorption Experiments

Gas sorption experiments were conducted in order to investigate the ability of **1** to absorb gases such as carbon dioxide and nitrogen. The isotherms obtained for nitrogen, carbon dioxide (195 K) and water vapour are depicted in **Figure 3.22**. Carbon dioxide (273 K) and nitrogen (77 K) sorption isotherms showed low sorption values of 1.1 cm^3 (STP) g^{-1} and 2.7 cm^3 (STP) g^{-1} respectively. However, improved sorption of carbon dioxide was observed at 195 K, showing a type-I isotherm. The total carbon dioxide gas absorbed at a relative pressure P/P_0 of 0.89 was 17.3 cm^3 (STP) g^{-1} (at 195 K) and BET surface equal to 60 $m^2 g^{-1}$ for carbon dioxide gas. Water vapour sorption of **1** showed that it readily absorbs water vapour at low relative pressures. The compound displayed a type-I isotherm that is representative of microporous materials. The total water absorbed at a relative pressure P/P_0 of 0.81 was 195.5 cm^3 (STP) g^{-1} at 298 K. The BET surface had a calculated value of 477 $m^2 g^{-1}$ for water vapour, while minor hysteresis occurred with the desorption isotherm.

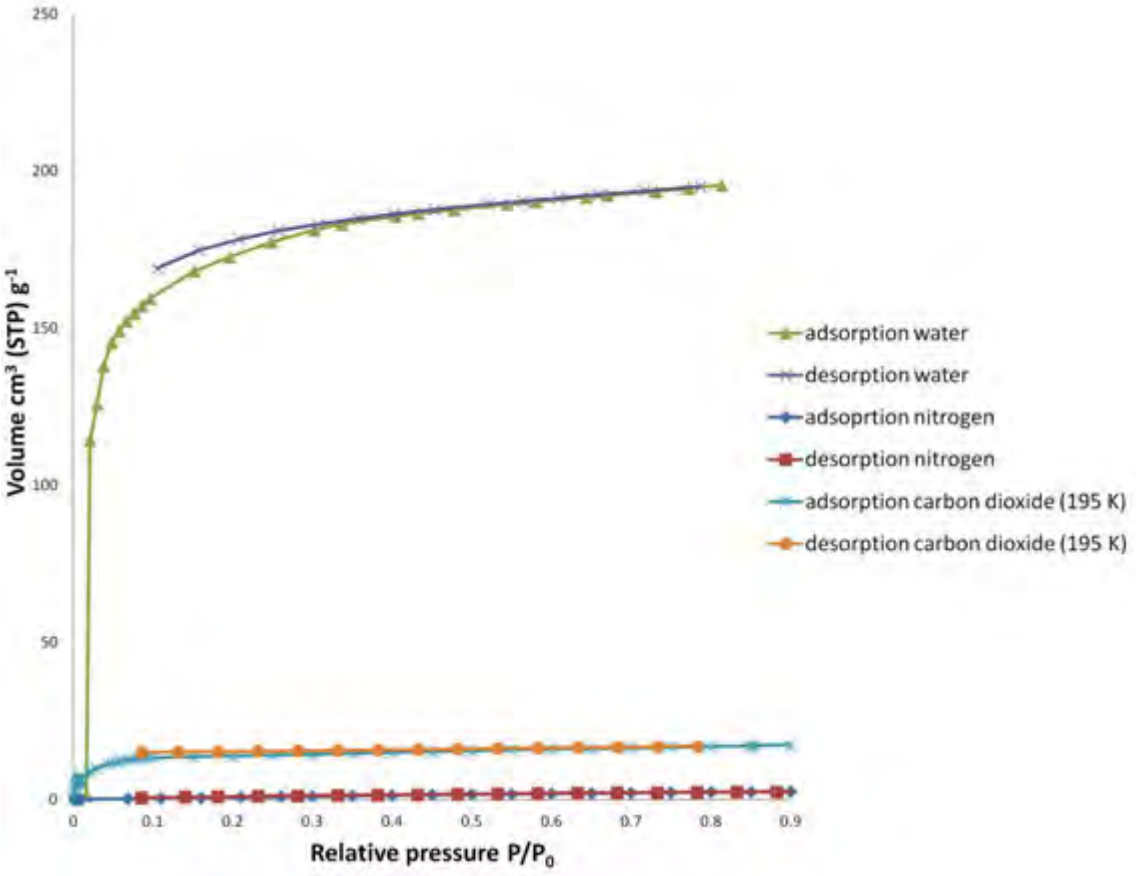

Figure 3.22: Nitrogen, carbon dioxide (195 K) and water vapour adsorption and desorption isotherms of **1**

3.11 Co-crystals of organic molecules used as ligands in the synthesis of 1

Further experiments were carried out in order to investigate the effect pH has on the formation of **1**. During the preparation of the solutions for the synthesis of the 2D MOF, the pH was altered to ~0 and ~2 using 3 M H_2SO_4 and placed in the oven at 90 °C. This yielded crystals of **1** with the resulting solution having a pH of 4. The experiment was repeated using triethylamine instead of H_2SO_4 to test whether **1** would form under basic conditions. The pH was altered to ~8 and ~10 and respectively. In both cases, a milky white solution formed, indicating that **1** could not be formed under basic conditions.

Additional experiments were performed in order to test the stability of **1** under acidic conditions. Crystals of **1** were added to a solution of water, upon heating and stirring at 80 °C. After a few drops of H_2SO_4 (3 M) were added the crystals dissolved. The solution was heated for 3 hours followed by slow cooling and clear, rod-shaped crystals were obtained. SCXRD analysis performed on these crystals (**1a**) revealed that the ASU consisted of a fully protonated H_3BTC molecule and a 4,4'-bpdo molecule (**Figure 3.23**).

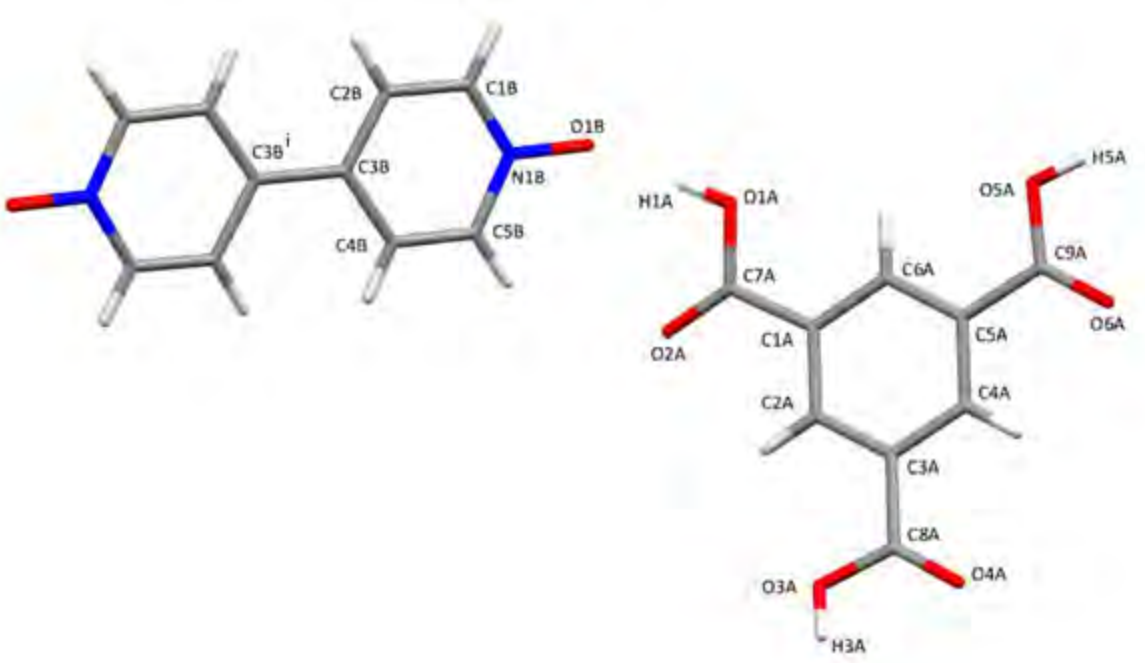

Figure 3.23: Crystal structure obtained for **1a**
Related by symmetry: ^{i}-x, 1-y, -z

Hydrogen bonds are formed between a H_3BTC molecule and a 4,4'-bpdo molecule (O1A-H1A···O1B and O3A-H3A···O1B^{ii}) and between two H_3BTC molecules related by symmetry (O5A-H5A···O6A^{iii} and O5A^{iii}-H5A^{iii}···O6A) and as shown in **Figure 3.24**. The packing diagram of **1a** is shown in **Figure 3.25**.

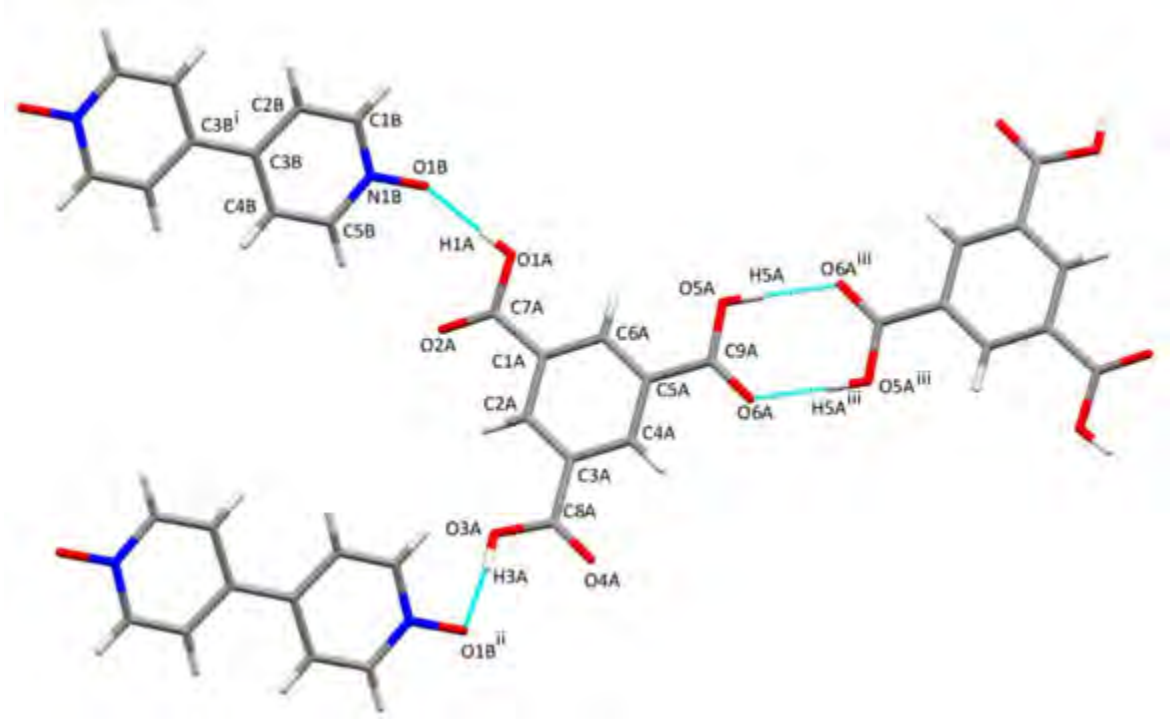

Figure 3.24: Hydrogen bonding occurring in **1a**
Related by symmetry: ^{i} -x, 1-y, -z ; ^{ii}1+x, y, z; ^{iii} 1-x, -y-1, -z

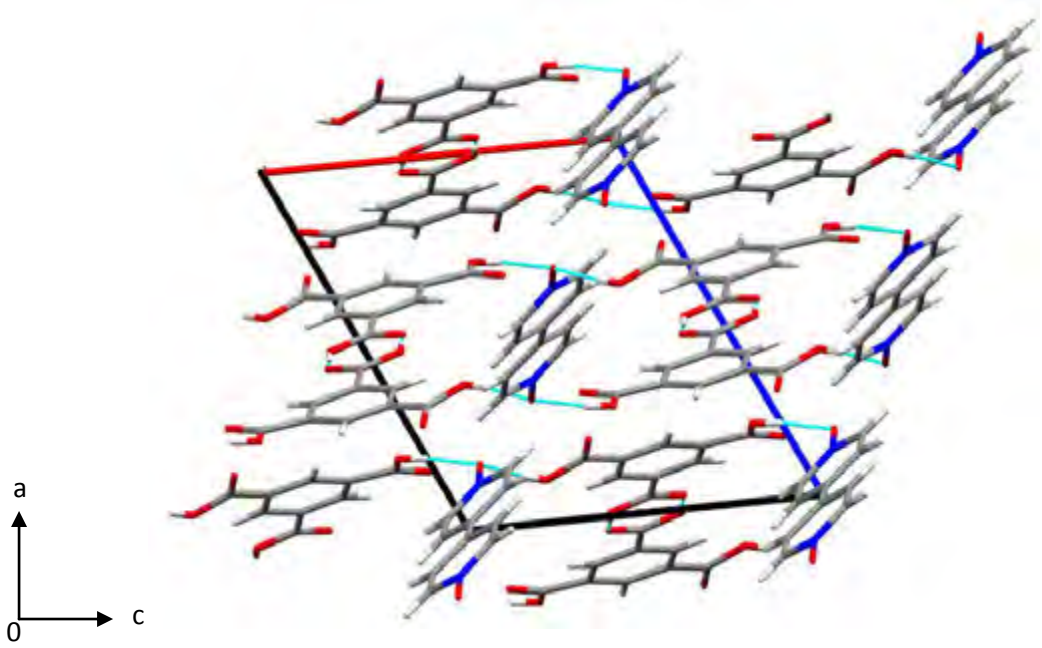

Figure 3.25: Packing arrangement of **1a** along *b*-axis

3.11.1 Thermogravimetric and Differential Scanning Calorimetry analysis

The thermal stability of **1a** was investigated by TGA and DSC experiments (**Figure 3.26**). According to TGA, there is no mass loss of the compound in the temperature range 21-283 °C. This is expected as there is no solvent present in the crystal structure. The crystals decompose at 350 °C. A complicated DSC thermogram was obtained each time the DSC experiment was repeated, possibly indicating complex phase changes.

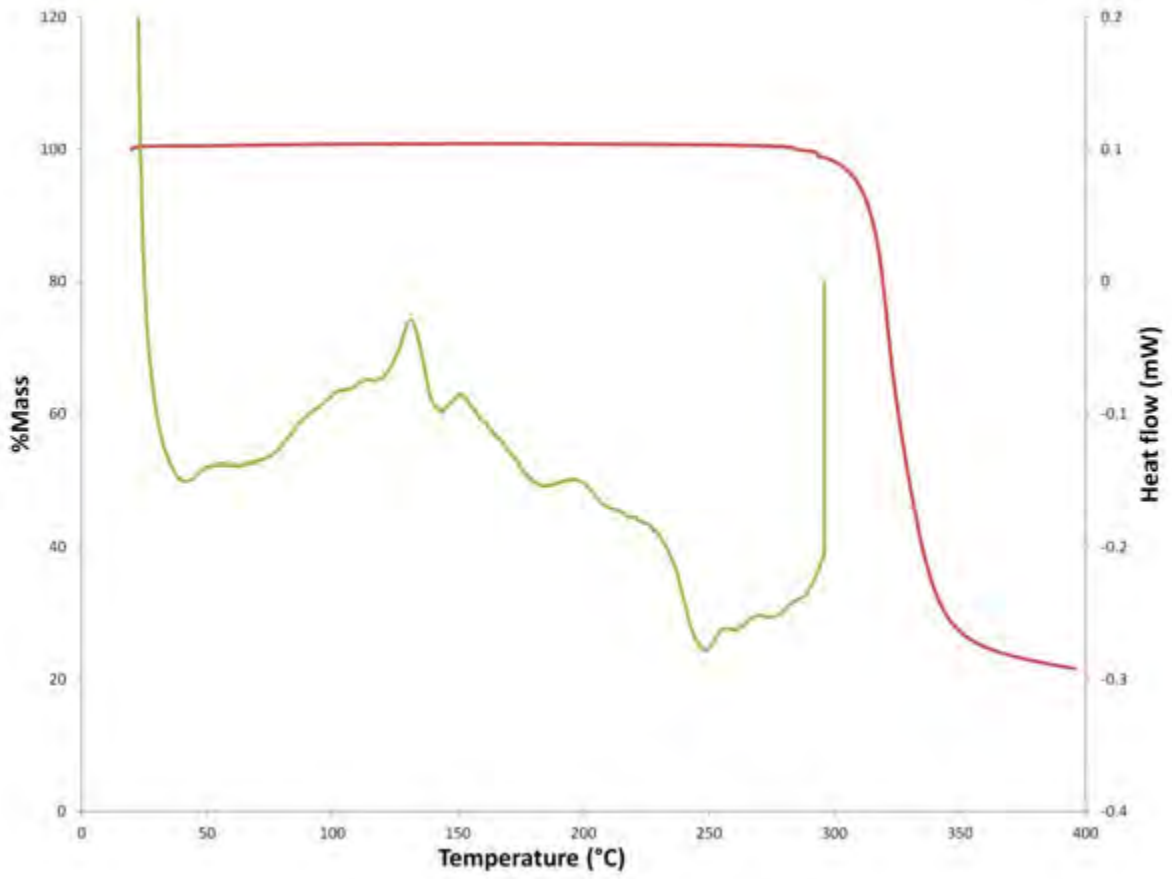

Figure 3.26: Overlay of TGA (red) and DSC (green) thermograms for **1a**

3.11.2 Hot stage microscopy

Hot stage microscopy studies were performed on **1a** in the range of 30-300 °C in order to observe possible phase changes (**Figure 3.27**). The crystals show no solvent loss from 30-260 °C. The crystal begins to crack at 150 °C and this continues up to 260 °C. The first sign of bubbling occurs at 260 °C associated with decomposition and by 300 °C the crystals are fully decomposed. Since the co-crystal was not the main focus of this research project, no further analysis on this material was pursued.

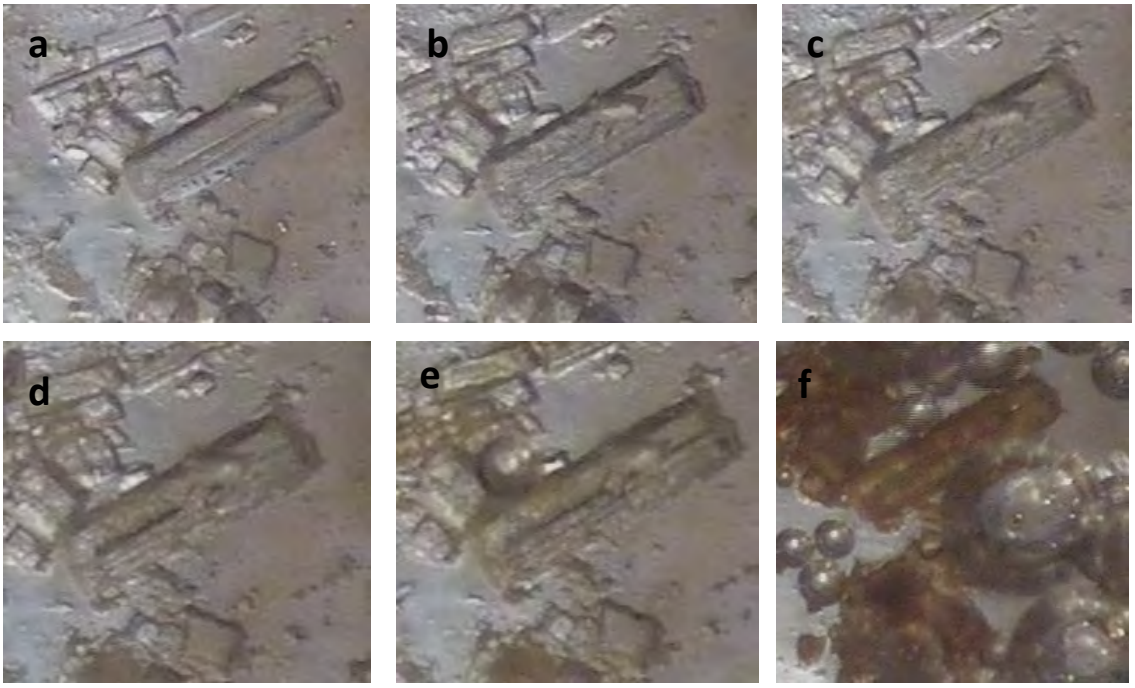

Figure 3.27: HSM images of **1a** at **a)** 30 °C **b)** 150 °C **c)** 180 °C **d)** 220 °C **e)** 260 °C **f)** 300 °C

3.12 Summary

A novel 2D MOF has been synthesised using $ZnSO_4 \cdot 7H_2O$, 4,4'-bipyridyl-*N*,*N'*-dioxide and 1,3,5-benzenetricarboxylic acid as the starting materials. VT-PXRD experiments provided evidence that the bulk sample remains crystalline and that structural changes are minimal at higher temperatures (30-190 °C). SCXRD analysis was performed at 104 K, 298 K, 323 K and 373 K on the same crystal in order to observe any structural changes upon solvent loss. The results show that the dehydration process is reversible and that it occurs *via* a SCSC process. Gas sorption experiments showed type-I isotherms for water vapour and low temperature carbon dioxide sorption (195 K).

3.13 References

1 Bruker (2007), *Bruker AXS Inc., Madison, Wisconsin USA*, 2007, **1**.

2 O. V. Dolomanov, L. J. Bourhis, R. J. Gildea, J. A. K. Howard and H. Puschmann, *J. Appl. Crystallog.*, 2009, **42**, 339–341.

3 G. M. Sheldrick, *Acta Crystallogr. Sect. A Found. Crystallogr.*, 2008, **64**, 112–122.

4 L. J. Barbour, *J. Appl. Crystallogr.*, 1999, **32**, 351–352.

5 R. Herbst-Irmer and G. M. Sheldrick, *Acta Crystallogr. Sect. B Struct. Sci. Found. Crystallogr.*, 2002, **58**, 477–481.

6 A. L. Spek, *Acta Crystallogr. Sect. D Biol. Crystallogr.*, 2009, **65**, 148–155.

7 A. G. Orpen, L. Brammer, F. H. Allen, O. Kennard, D. G. Watson and R. Taylor, *J. Chem. Soc. Dalt. Trans.*, 1989, S1–S83.

8 K. K. Bisht and E. Suresh, *J. Am. Chem. Soc.*, 2013, **135**, 15690–15693.

9 D. L. Long, A. J. Blake, N. R. Champness and M. Schroder, *Chem. Commun.*, 2000, **22**, 2273–2274.

10 F. H. Allen, *Acta Crystallogr. Sect. B Struct. Sci.*, 2002, **58**, 380–388.

11 C. F. Macrae, I. J. Bruno, J. A. Chisholm, P. R. Edgington, P. McCabe, E. Pidcock, L. Rodriguez-Monge, R. Taylor, J. Van De Streek and P. A. Wood, *J. Appl. Crystallogr.*, 2008, **41**, 466–470.

12 M. C. Etter, *Acc. Chem. Res*, 1990, **23**, 120–126.

13 D. Sarma and S. Natarajan, *Cryst. Growth Des.*, 2011, **11**, 5415–5423.

14 Z. Su, M. Chen, T. Okamura, M. sheng Chen, S. Chen and W. Sun, *Inorg. Chem.*, 2011, **50**, 985–991.

15 R. Sarma and J. B. Baruah, *Solid State Sci.*, 2011, **13**, 1692–1700.

16 X. Wang, J. Li, H. Lin, H. Hu, B. Chen and B. Mu, *Solid State Sci.*, 2009, **11**, 2118–2124.

17 Guidelines for Authors, *J. Org. Chem.*, 2016, <http://pubs.acs.org/paragonplus/submission/joceah/joceah_authguide.pdf>, (accessed 5 October 2016).

CHAPTER 4: $[Cd(bpe)_{1.5}nbdc]_n \cdot nDMF$ (2)

A mixed-ligand, two-fold interpenetrated 2D MOF was prepared using cadmium(II), 1,2-bis(4-pyridyl)ethane (bpe) and 5-nitro-1,3-benzenedicarboxylic acid (H_2nbdc) as the starting materials. The compound has a molecular formula of $[Cd(bpe)_{1.5}nbdc]_n \cdot nDMF$ (**2**) and was characterised using X-ray diffraction studies (SCXRD, VT-SCXRD, PXRD and VT-PXRD), thermal analysis (TGA, DSC and HSM), Fourier transform infrared spectroscopy (FT-IR) and elemental analysis (EA). Gas and water vapour sorption experiments were conducted in order to investigate the porosity of the compound. Compound **2** was compared with a similar structure found in the literature. VT-PXRD and VT-SCXRD showed that structural changes occur in compound **2** with an increase in temperature.

4.1 Synthesis

The metal salt, $Cd(NO_3)_2 \cdot 4H_2O$ (29 mg, 0.095 mmol), was dissolved in 3.6 ml H_2O and 0.2 ml H_2SO_4 (3 M). In a separate vial, the organic linkers 1,2-bis(4-pyridyl)ethane (18 mg, 0.095 mmol) and 5-nitro-1,3-benzenedicarboxylic acid (20 mg, 0.095 mmol) were dissolved in 4.8 ml *N*,*N*'-dimethylformamide (DMF). Both solutions were heated while stirring and the clear solutions were combined and left in the oven at 80 °C. Clear, block-shaped crystals were obtained after 48 hours.

4.2 Single Crystal X-Ray Diffraction Analysis

4.2.1 Structure Solution and Refinement

A single crystal of **2** was removed from the mother liquor and placed in Paratone N oil, before being mounted on a nylon loop. Single crystal X-ray diffraction (SCXRD) data collections were carried out on a Bruker DUO APEX II CCD diffractometer. Unit cell refinement and data reductions were carried out using SAINT-Plus.[1] The space group suggested by XPREP[1] for the 298 K structure was $P\bar{1}$ and it was solved using direct methods in SHELXS-97.[2] All non-hydrogen atoms were placed and initially refined isotropically using SHELXL-2014/7.[3] The atoms of the bpe ligand were disordered over two positions, labelled "A" and "B". The hydrogen atoms in **2** were placed in idealised positions using a riding model and assigned temperature factors relative to the parent atom. The temperature

factors are 1.2 times that of the parent atom for phenyl hydrogen atoms and 1.5 times that of the parent atom for methyl hydrogen atoms. DFIX restraints were applied to the solvent molecule to achieve ideal bond lengths (± 0.005 Å) for non-hydrogen atoms.

4.2.2 Structure Description

The crystal structure obtained for compound **2** at 298 K will be described next and a comparison will be made with a similar compound reported by Luo et *al*. (CSD reference code UJOJUY).[4] Compound **2** crystallises in the triclinic crystal system in the space group $P\bar{1}$. The asymmetric unit (ASU) of **2** consists of one Cd(II) cation, one fully deprotonated 5-nitro-1,3-benzenedicarboxylic acid ligand (nbdc), one disordered 1,2-bis(4-pyridyl)ethane ligand (bpe), one-half of a bpe ligand and one DMF molecule with its sof value refined to 1.00 (**Figure 4.1**). Cd01 has an octahedral coordination geometry and is coordinated to the O1D, O2D and O4D^{i} atoms of the carboxylate functional groups of the nbdc ligand and the N1A, N2A^{ii} and N1C atoms of the bpe ligands. The 2+ charge on the cadmium ion is counter balanced by the 2- charge of the nbdc ligand, with the bpe ligand contributing no charge to the framework.

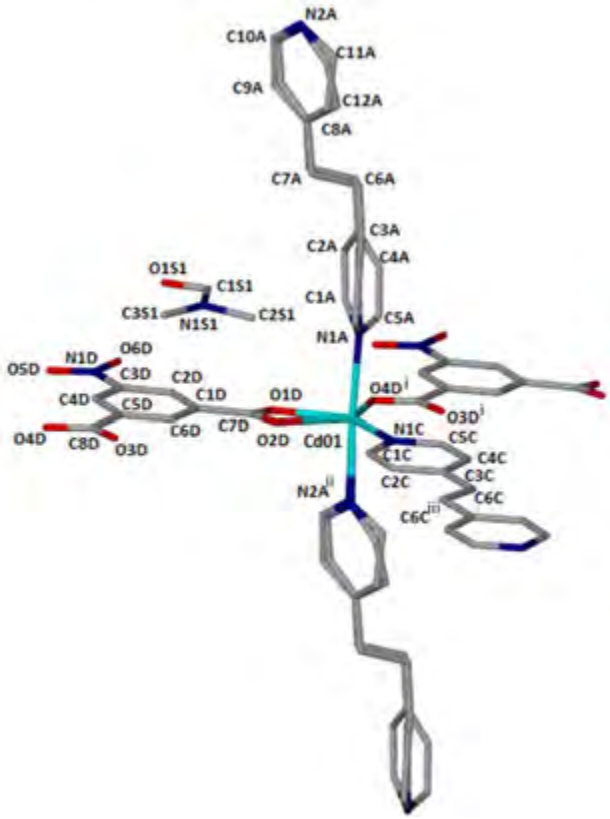

Figure 4.1: Basic chemical unit of **2** showing the coordination environment around Cd(II). Hydrogen atoms were omitted and disordered "B" component of the bpe ligand is not labelled for clarity
Related by symmetry: ^{i}1+x, y, z; ^{ii}x, y, z-1; ^{iii}1-x, -y, -z

The bond lengths around Cd01 range between 2.3065(16)-2.6522(18) Å in the 298 K structure. These values are relatively close to the values found in the literature for a similar structure (at 293 K) using the same ligands as compound **2** and Cd(II) as the metal, with the formula $[Cd(bpe)_{1.5}nbdc]0.25H_2O$ (UJOJUY).[4] A comparison of compound **2** with UJOJUY shows that the main difference between the two compounds is the solvent molecule, the coordination around the metal centre at similar temperatures and the degree of interpenetration of the frameworks. The solvent present in **2** is a DMF molecule, while a water molecule is present in UJOJUY (synthesised hydrothermally).[4] In UJOJUY, the coordination around Cd(II) is pentagonal bipyramidal with the nbdc ligands coordinating in a bidentate fashion. UJOJOY has been reported as a three-fold interpenetrated network, while compound **2** is two-fold interpenetrated. Compound **2** is considered a two-fold interpenetrated network since each motif is not interlaced with all the other ones.[5] **Figure 4.2** displays the basic chemical unit of UJOJUY at 293 K. The crystallographic data of **2** and UJOJUY are shown in table 4.1 and the bond lengths of are summarised in table 4.2. All bond lengths related to **2** and the angles around the metal centre of **2** can be found in Appendix B.

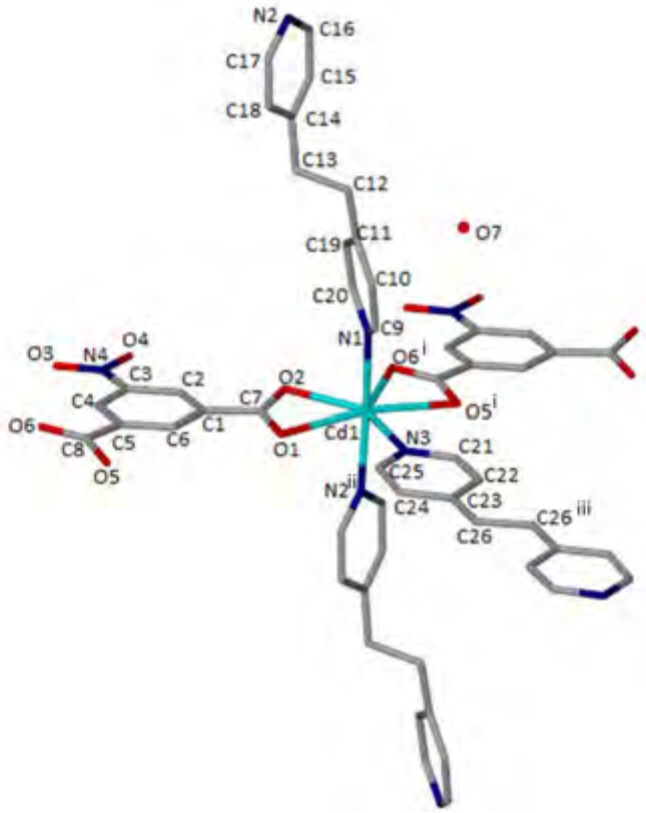

Figure 4.2: Basic chemical unit of literature structure (UJOJUY) showing the coordination environment around Cd(II). Hydrogen atoms omitted for clarity.
Related by symmetry: [i]x-1,y, z; [ii]x,y,z+1; [iii]-x-2, -y-4, -z

Table 4.1: Crystal Data and refinement parameters of **2** (298 K) and UJOJUY (293 K)

	Compound 2	**UJOJUY**[4]
Empirical formula	$CdC_{29}H_{28}N_5O_7$	$CdC_{26}H_{21.5}N_4O_{6.25}$
Formula weight (g mol^{-1})	670.97	602.37
Space group	$P\bar{1}$	$P\bar{1}$
a (Å)	10.270(1)	10.2414(8)
b (Å)	10.9495(11)	10.9924(8)
c (Å)	13.9134(13)	13.8482(9)
α (°)	101.807(2)	109.940(3)
β (°)	100.473(2)	99.410(3)
γ (°)	109.366(2)	109.142(3)
Volume (Å^3)	1391(2)	1316.3(2)
Z	2	2
Calculated density, ρ (g cm^{-3})	1.602	1.520
μ (mm^{-1})	0.842	0.877
***F* (000)**	682	607
Reflections collected	17445	3148
Unique reflections	8571	1672
Parameters	354	343
Goodness-of-fit on F^2	1.09	1.12
***R* Indices [I>2σ(*I*)]**	0.0285	0.0553
wR_2 indices (all data)	0.0722	0.1435

Table 4.2: Selected bond lengths (Å) around Cd(II) metal centre in **2** (298 K) and UJOJUY[4]

Bond in compound 2	**Bond length (Å)**	**UJOJUY bond length (Å)**
Cd01-O1D	2.3452(18)	2.322(10)
Cd01-O2D	2.544(2)	2.592(10)
Cd01-O3D^{i}	2.6522(18)	2.599(9)
Cd01-O4D^{i}	2.3065(16)	2.315(11)
Cd01-N1A	2.375(10)	2.361(12)
Cd01-N1C	2.3486(15)	2.345(12)
Cd01-N2A^{ii}	2.368(18)	2.328(13)

4.2.3 Crystal Packing

The bpe ligands in **2** adopt a *trans* conformation (within the ligand) and link the metal centres into a $[Cd(bpe)_{1.5}]_n$ ladder unit and adopt two ligand conformations in the framework, namely a type 1 and type 2 conformation, respectively (**Figure 4.3a**). Type 1 represents the sides of the ladder, while type 2 represents the rungs of the ladder with the pyridyl rings being co-planar. An extension of the ladder unit reveals that **2** forms a square lattice motif containing rectangular channels (**Figure 4.3b**). The nbdc ligand serves as a μ_2-bridge through two, bidentate coordinated carboxylate functional groups linking the ladders into a 2D bilayer (**Figure 4.4**). The nitro groups of the nbdc ligand prevent the 2D network from extending into a 3D network. The packing arrangement of **2** reveals a two-fold interpenetrated 2D MOF (See **section 4.3.1**).

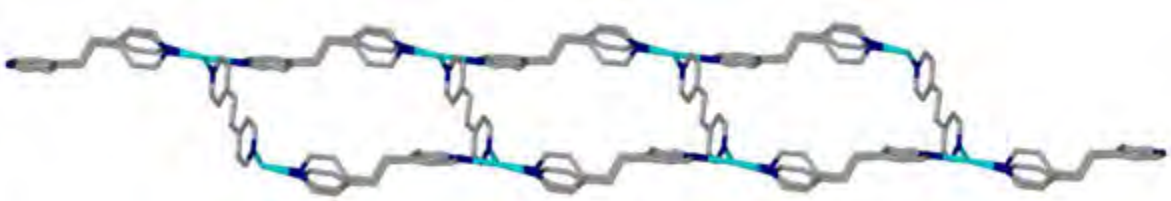

Figure 4.3a: View of the $[Cd(bpe)_{1.5}]_n$ ladder in **2**

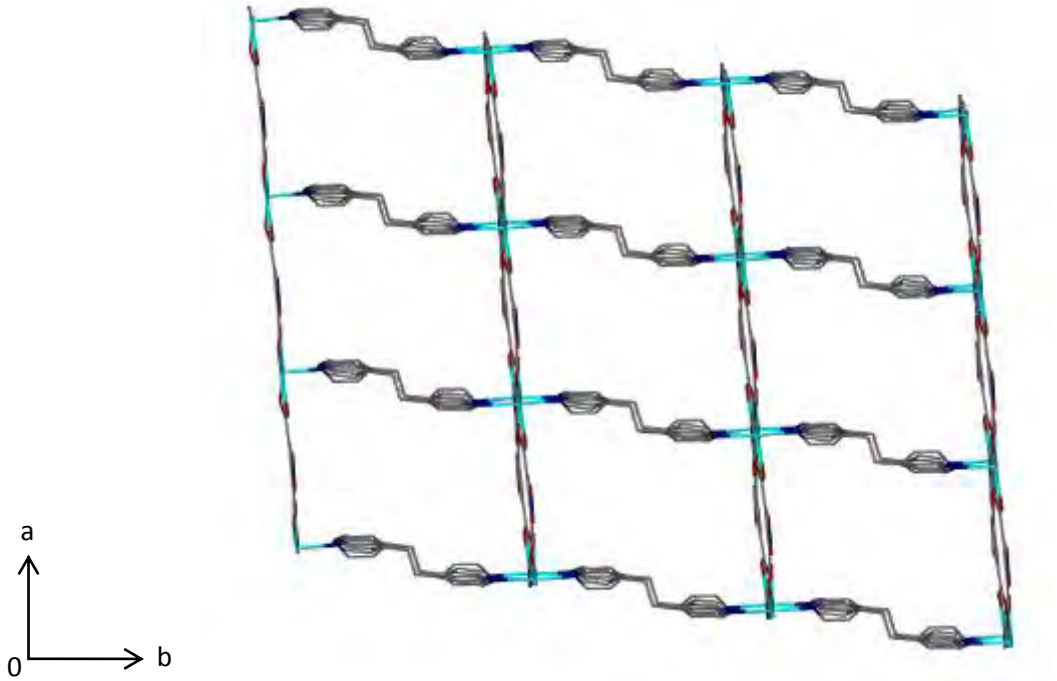

Figure 4.3b: Square lattice formation of **2** showing rectangular channels along the *b*-axis

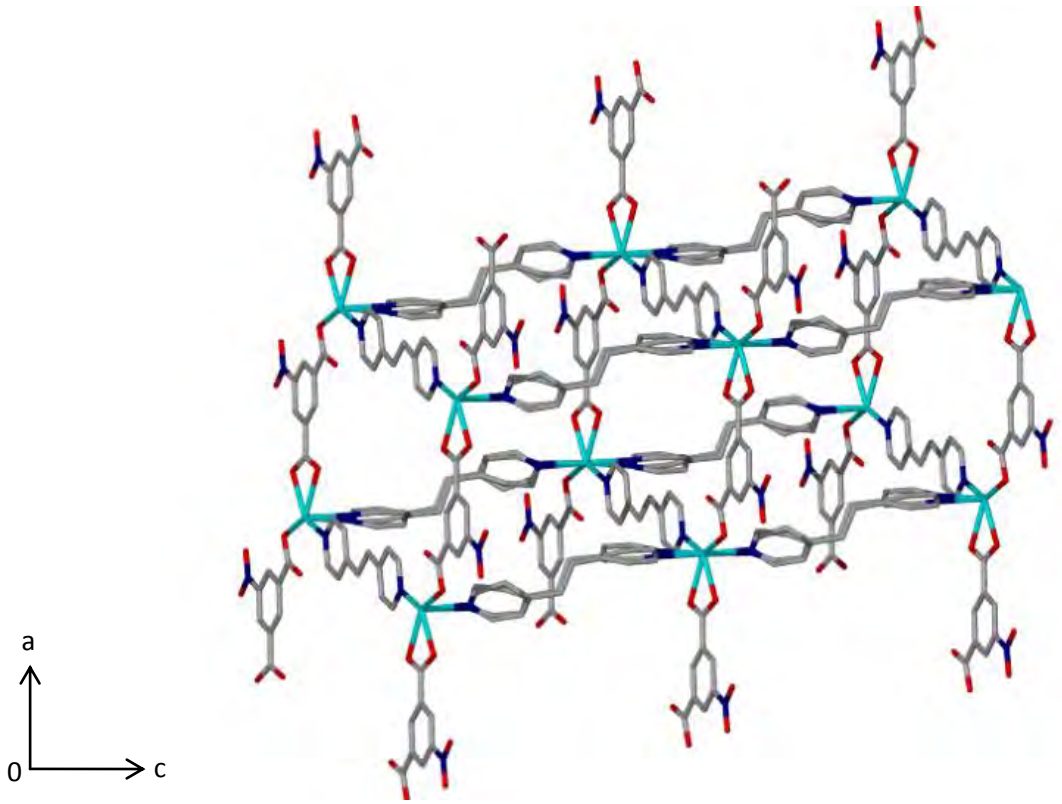

Figure 4.4: View of 2D bilayer of **2** viewed along the *b*-axis

From SCXRD analysis, it was shown that single DMF molecules occupy the voids of the structure. MERCURY revealed that there is one void per unit cell and that these voids seem to be connected into channels (**Figure 4.5** and **Figure 4.6**).[6] The estimated total potential solvent volume, as calculated by MERCURY, with the DMF molecule deleted from the structure, is 162.29 $Å^3$ per unit cell, which equates to 11.7% of the total unit cell volume (1391 $Å^3$). No classic hydrogen bonding occurs between the DMF molecule and the framework. Intermolecular and intramolecular interactions (C-H···O bonding) that do occur in **2** are suggested to reinforce the geometry and impart stability in the MOF. These interactions are summarised in table 4.3. It is noted, however, that the intermolecular interactions between the frameworks were absent in the 373 K structure.

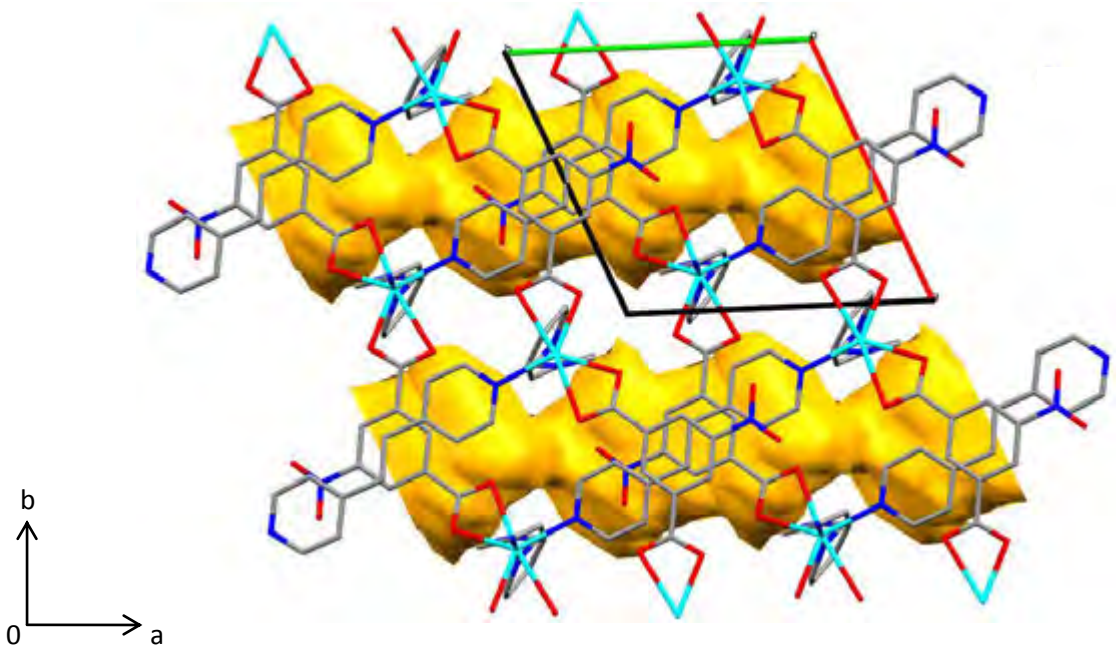

Figure 4.5: Crystal packing of **2** showing voids in 298 K structure along the *c*-axis

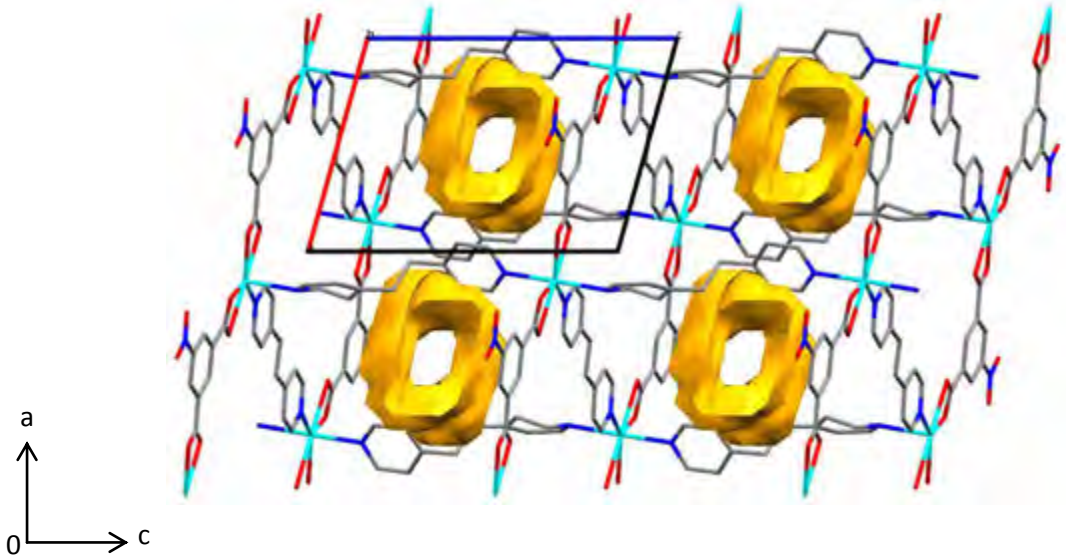

Figure 4.6: Channels present in **2** viewed along the *b*-axis

Table 4.3: Intermolecular and intramolecular interactions present in **2**

Donor – H···Acceptor	D-H (Å)	H···A(Å)	D···A (Å)	D – H···A (°)
C1C-H1C···O2D (intra)	0.93	2.43	3.132(3)	133
C5A-H5A···O6D^{i} (inter)	0.93	2.44	3.169(8)	136
C5C-H5C···O3D^{ii} (intra)	0.93	2.44	3.190(3)	138
C9A-H9A···O4D^{iii} (inter)	0.93	2.50	3.396(11)	163

Symmetry operations: ^{i}x,y-1,z; ^{ii}1+x,y,z; ^{iii}1-x,2-y,1-z

4.3 Variable-Temperature X-Ray Diffraction Experiments

4.3.1 Variable-Temperature Powder X-Ray Diffraction

Crystals of **2** were gently ground and then placed on a sample holder which was heated from 30-250 °C, followed by cooling to 30 °C (**Figure 4.7**). The patterns obtained at higher temperatures (100-250 °C) show that the crystallinity of the compound is retained as the temperature increases. However, a few differences were observed in this temperature range and upon cooling to 30 °C, indicating the occurrence of possible phase transitions in the compound.

The pattern obtained at 30 °C confirmed that the bulk material was a match to that of the calculated pattern. An artefact peak at 2θ position 4.3° occurs for all the PXRD patterns taken from 30–250 °C, including cooling to 30 °C and is due to experimental setup. The peak that occurs at 2θ position 9.5° in the calculated pattern (298 K) is shifted to slightly lower 2θ values in the experimental patterns as the temperature increases from 30-250 °C. New peaks occur at 2θ 10.6° and 11.7° in the temperature range 150-250 °C and 100-200 °C, respectively. The peak at 2θ 16.2° occurs from 100-250 °C, but is absent in the calculated pattern. The peaks that occur in the 2θ region 12-14.5°, match closely in the calculated pattern and the pattern obtained at 30 °C. However, as the temperature increases, slight changes occur and the peak at 14.2° (30 °C and 100 °C) is absent from 150-250 °C.

On cooling to 30 °C, the pattern is slightly different from the calculated pattern (differences are indicated by arrows in **Figure 4.8**). When comparing the calculated pattern to the trace of the sample cooled to 30 °C, differences included new peaks occurring at 2θ positions 9.8° and 11.7°. There is also an absence of the peak 12.2°, which is present in the calculated pattern. A slight shift in the peak at 15.7° (15.3° in the calculated pattern) also occurs. The differences mentioned above could be due to the loss of DMF from the structure and small structural changes that follow with an increase in temperature.

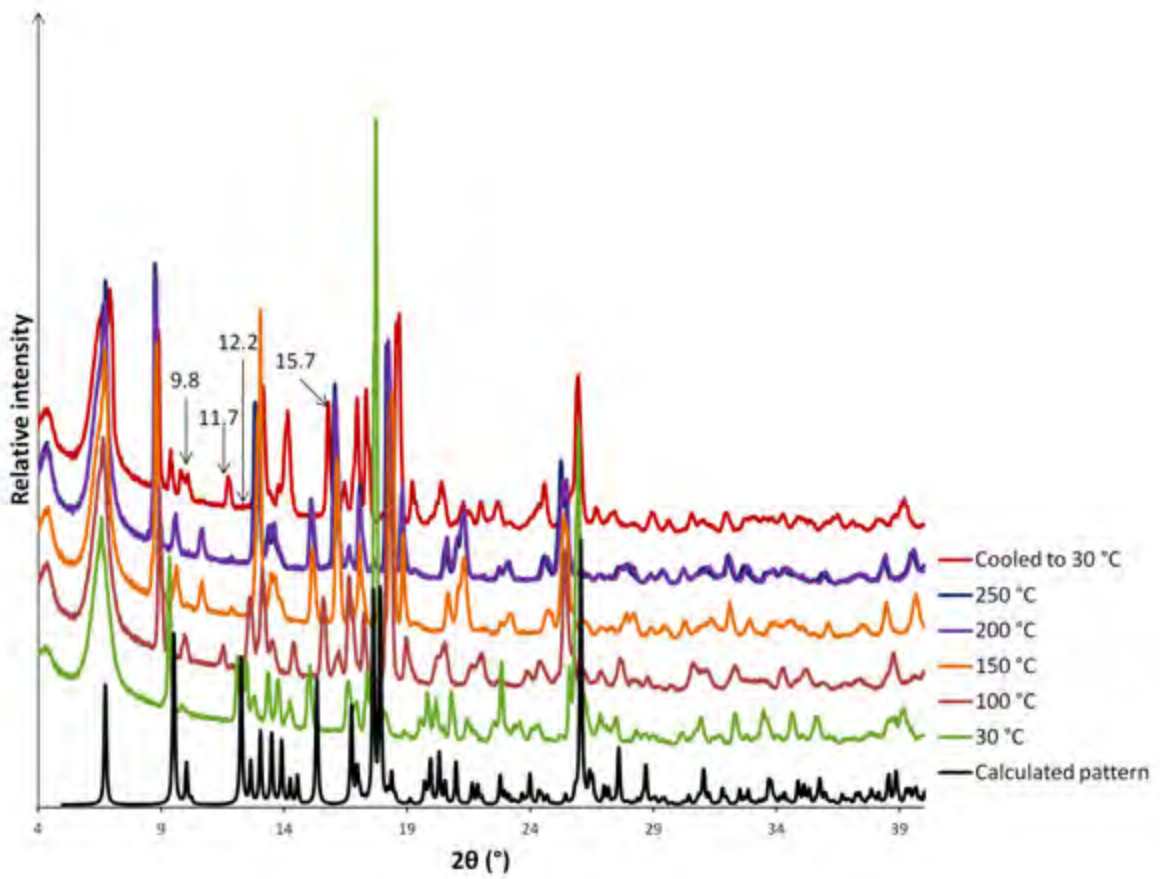

Figure 4.7: Variable-temperature PXRD of **2** from 30–250 °C and cooling to 30 °C

A sample of the as-synthesised material was dried on filter paper and placed under vacuum for 12 hours at 100 °C. This sample was then subjected to TGA, which showed a negligible mass loss in the temperature range 30-350 °C, thus indicating that the framework was solvent-free. A PXRD experiment was performed on the solvent-free sample and compared to the calculated PXRD pattern (at 373 K) and the "cooled to 30 °C" PXRD pattern (**Figure 4.8**). The dried material was slightly different to the calculated PXRD pattern (absence of a peak at 2θ 10.8°), but closely matched the PXRD pattern of the material cooled to 30 °C from the VT-PXRD experiment apart from a slight shift in 2θ.

The PXRD pattern of the trace cooled to 30 °C and the calculated pattern of UJOJUY[4] was then compared. It was concluded that the sample cooled to 30 °C is closer to UJOJUY[4] than compound **2** at 298 K. This was also the case with the material dried under vacuum. The crystals became opaque in both experiments (dried under vacuum and VT-PXRD), indicating that monocrystallinity may have been lost, however, the sample remains crystalline.

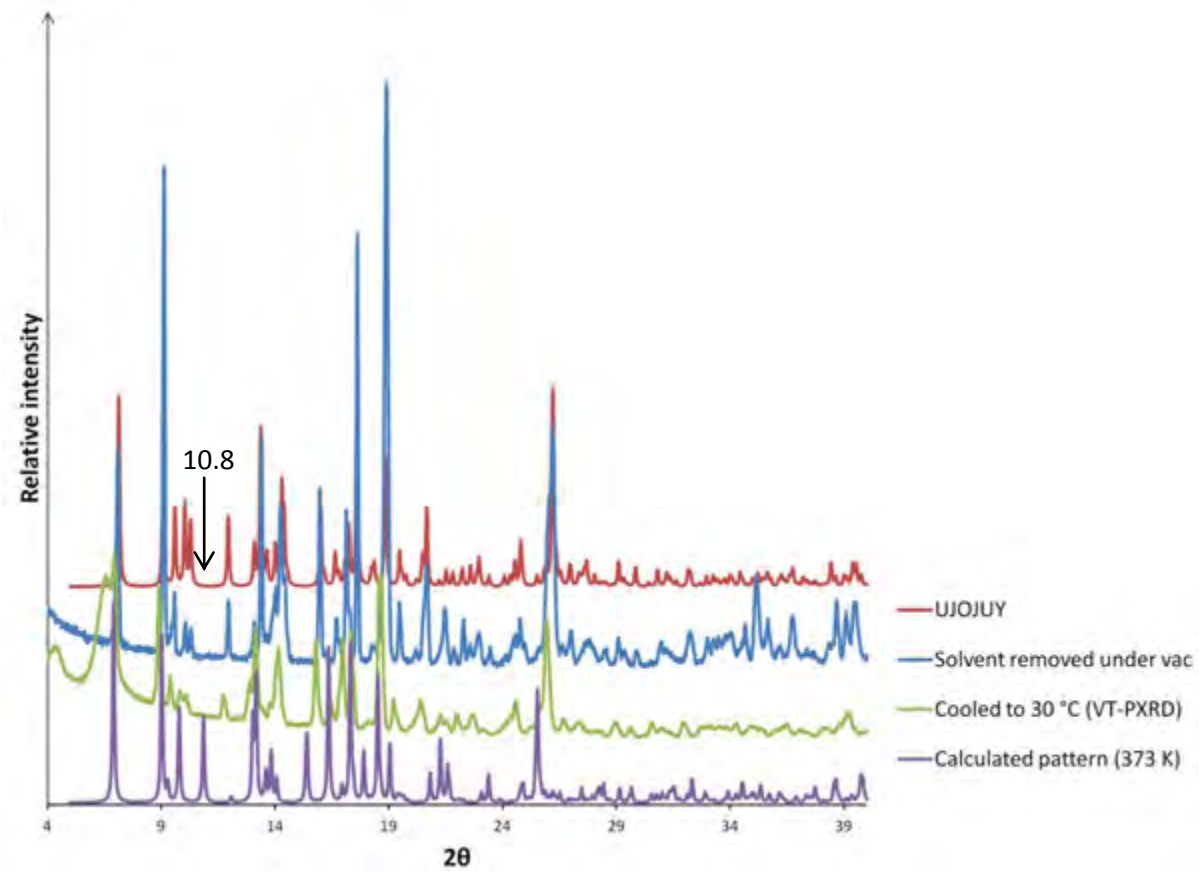

Figure 4.8: PXRD patterns of evacuated compound **2**, pattern obtained from VT-PXRD of compound **2** heated to 250 °C and then cooled to 30 °C, the calculated pattern of **2** at 373 K and the calculated pattern of UJOJUY (293 K)

4.3.2 Variable-Temperature Single Crystal X-Ray Diffraction

A single crystal of **2** was subjected to successive data collections at 104 K, 298 K, 323 K and 373 K in order to determine whether structural changes can be monitored upon solvent loss (SCXRD data presented in table 4.4). The space group suggested by XPREP[1] for the 104 K, 298 K and 323 K structures was $P\bar{1}$ and was solved using direct methods in SHELXS-97, while the space group *C*2/*c* was suggested for the structure at 373 K and was solved using direct methods in SHELXT-97.[2] Variable-temperature single crystal X-ray diffraction (VT-SCXRD) analysis revealed subtle differences in the ASU of **2** as the temperature increases. Overlays of the ASU at 104 K with those of the higher temperature structure are shown in **Figure 4.9**. As the temperature increases, there is a change in the orientation of the pyridyl rings of the bpe ligand, with the most prominent difference occurring at 373 K. The overlays (using Mercury[5]) showed a close match for the 298 K and 323 K ASU structures with root-mean-square deviations of 0.0227 Å and 0.0353 Å, whilst the 373 K structure was significantly more different with a root-mean-square deviation value of 0.195 Å.

It was noted that the DMF molecule is present in the structure from 104 K to 323 K (sof equal to 0.49). At 373 K, changes include the absence of the DMF molecule, a space group change from $P\bar{1}$ to $C2/c$, a quadrupling of the unit cell volume and a lattice type change of the structure. The refined sof values for the "A" and "B" components of the 104 K, 298 K and 323 K structures are 0.58 and 0.42, 0.54 and 0.46 and 0.76 and 0.24, respectively. The structure at 373 K consists of a disordered bpe ligand labelled "A" and "B" as well as a disordered nbdc ligand labelled "D" and "E". The refined sof values for "A" and "B" are 0.55 and 0.45, while the sof values for "D" and "E" are 0.54 and 0.46, for the 373 K structure, respectively. However, it was observed that the disorder of the bpe ligand occurred mostly at the pyridyl ring closest to the solvent molecule (**Figure 4.9**) at all four temperatures.

Figure 4.9: Overlay of ASU of **2** at 104 K (blue) with the ASUs of the 298 K (yellow), 323 K (green) and 373 K (red) structures, respectively. Disorder omitted for clarity.

Comparisons were made between the 104 K and 373 K structures using common viewpoints. **Figure 4.10a** shows the absence of disorder in the nbdc ligand in the 104 K structure, which is present in the 373 K structure. The fact that the disorder of the nbdc ligand is absent at the lower temperatures, indicates that the disorder of this ligand is dynamic at 373 K and may be described as a 'flapping'. **Figure 4.10b** indicates the difference in the square lattice motif between the 104 K and 373 K structures, with the "flaps" appearing in the channels of the 373 K structure. Therefore, in order to determine the void space in the 373 K structure, the major and minor component of the nbdc ligand were

deleted respectively to calculate the average void space available in the 373 K structure. The orientation of the pyridyl rings in the bpe ligand also varies between the 104 K structure and 373 K structure (**Figure 4.10b**). The tilted rectangular channels in the 104 K structure, viewed along the *c*-axis, can be seen in **Figure 4.10c**.

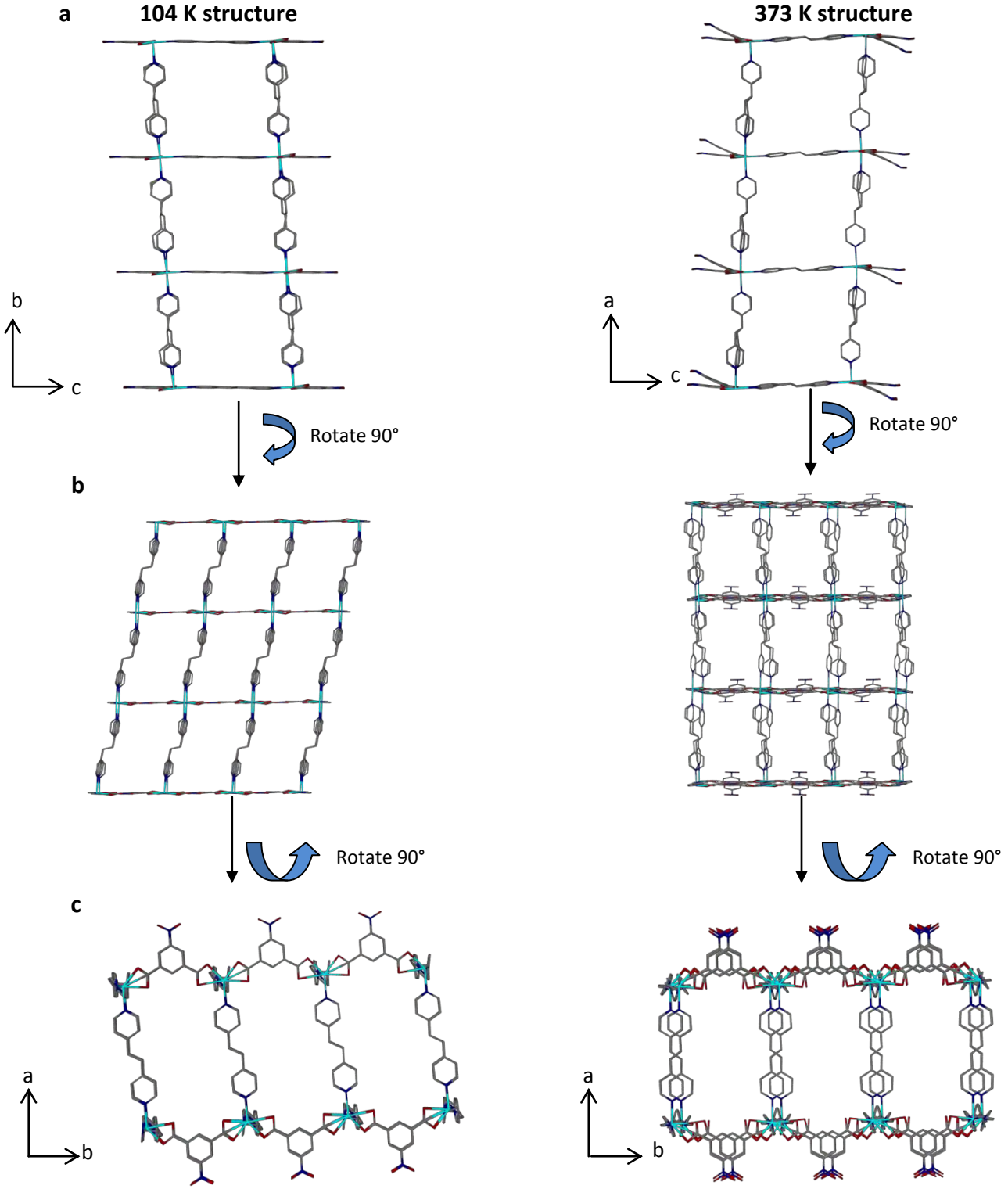

Figure 4.10: Common view points of 104 K (left) and 373 K (right) structures **a)** viewed along *a*-axis (104 K) and *b*-axis (373 K) **b)** square lattice motif **c)** rectangular channels viewed along *c*-axis

The void space per unit cell volume (DMF molecule artificially deleted in 104 K, 298 K and 323 K structures), calculated using MERCURY with a probe radius of 1.2 Å, for **2** at all four temperatures is shown in table 4.5. The degree of interpenetration between the 104 K and 373 K structures were compared in order to ascertain whether the degree of interpenetration changes with the removal of DMF from the structure (**Figure 4.11**). The compound remains two-fold interpenetrated in the 373 K structure, with each bilayer interlocked by two identical, adjacent frameworks. However, there is a decrease in the number of inter-framework interactions (C-H···O interactions) in the 373 K structure.

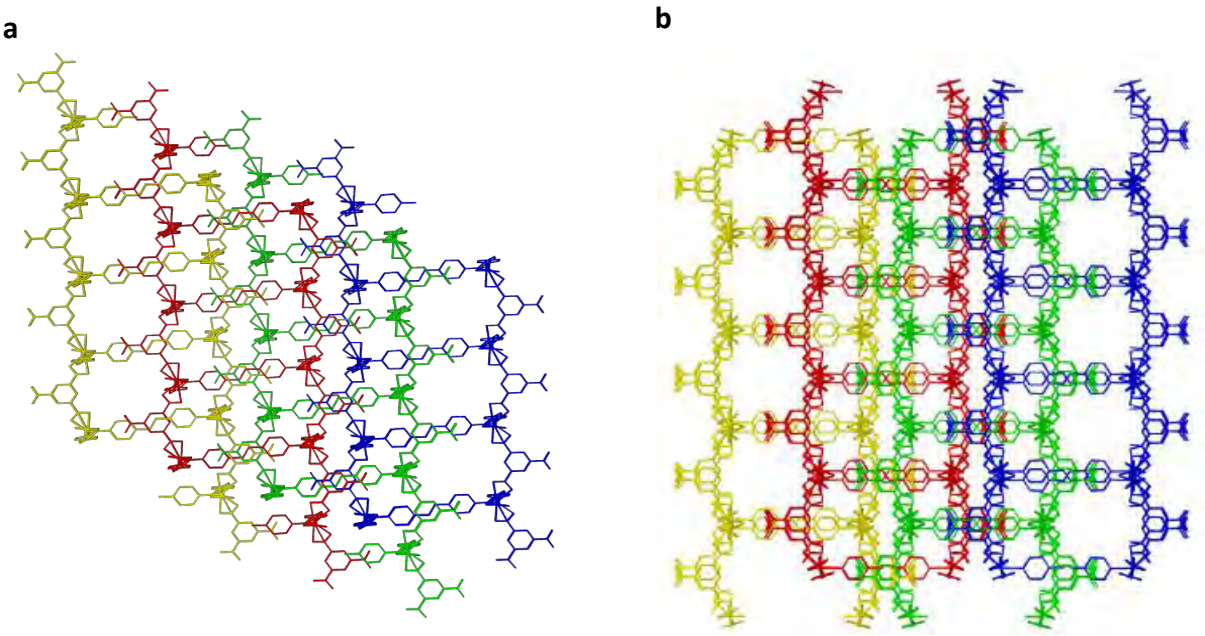

Figure 4.11: Two-fold interpenetration in **a)** 104 K structure and **b)** 373 K structure

Table 4.4: Crystal data and refinement parameters for **2** at 104 K, 298 K, 323 K and 373 K

	104 K	**298 K**	**323 K**	**373 K**
Empirical formula	$C_{28.5}H_{26.9}N_{4.8}O_{6.8}Cd$	$C_{28.5}H_{26.9}N_{4.8}O_{6.8}Cd$	$C_{27.4}H_{24.4}N_{4.4}O_{6.4}Cd$	$C_{26}H_{20.1}N_4O_6Cd$
Formula weight (g mol^{-1})	659.64	659.79	633.55	596.97
Temperature (K)	104	298	323	373
Wavelength (Å)	0.71073	0.71073	0.71073	0.71073
Crystal system	Triclinic	Triclinic	Triclinic	Monoclinic
Space group	$P\bar{1}$	$P\bar{1}$	$P\bar{1}$	*C2/c*
a (Å)	10.2340(5)	10.270(1)	10.278(3)	27.330(6)
b (Å)	10.8368(6)	10.9495(11)	10.999(3)	10.234(2)
c (Å)	13.8265(7)	13.9134(13)	14.002(4)	20.922(5)
α (°)	100.767(1)	101.807(2)	102.274(7)	90
β (°)	102.256(1)	100.473(2)	100.019(7)	110.635(7)
γ (°)	108.843(1)	109.366(2)	109.594(6)	90
Volume (Å^3)	1363.02(12)	1391(2)	1404.5(7)	5476(2)
Z	4	4	4	8
ρ (g cm^{-3})	1.607	1.575	1.498	1.448
μ (mm^{-1})	0.857	0.840	0.827	0.842
***F* (000)**	670	670	641	2401
Crystal size (mm^3)	1.22 x 0.49 x 0.31	1.22 x 0.49 x 0.31	1.22 x 0.49 x 0.31	1.22 x 0.49 x 0.31
θ Range scanned (°)	2.92-30.65	2.82-30.77	2.82-30.88	1.592-30.643
Index range	-14 ≤ h ≤ 14, -15 ≤ k ≤ 15, -19 ≤ l ≤ 18	-14 ≤ h ≤ 14, -15 ≤ k ≤ 15, -19 ≤ l ≤ 19	-14 ≤ h ≤ 14, -15 ≤ k ≤ 15, -19 ≤ l ≤ 19	-38 ≤ h ≤ 36, -14 ≤ k ≤ 14, -29 ≤ l ≤ 27
Reflections collected	17010	17445	15371	23205
Unique reflections	8338	8571	8545	8102
R_{int}	0.014	0.014	0.047	0.071
Data/Restraints/ Parameters	8338/27/509	8571/54/509	8545/346/479	8102/889/516
Goodness-of-fit on F^2	1.17	1.08	1.11	1.02
Final *R* indices [I>2σ(*I*)]	R_1=0.0304, wR_2=0.0764	R_1=0.0267, wR_2=0.0711	R_1=0.704, wR_2=0.2066	R_1=0.0598, wR_2=0.1519
***R* indices (all data)**	R_1=0.0311, wR_2=0.0768	R_1=0.0285, wR_2=0.0722	R_1=0.0792 wR_2=0.2139	R_1=0.1189, wR_2=0.1832
$\Delta\rho_{min,max}$ (e Å^{-3})	1.70, -1.18	1.05, -0.84	5.10, -2.12	1.48, -1.11

Table 4.5: Void space per unit cell volume of **2** at various temperatures, with DMF artificially deleted in the 104 K, 298 K and 323 K structures and absent in the 373 K structure

Temperature (K)	Void space per unit cell volume (Å^3)	Total unit cell volume (Å^3)	%
104	147.09	1363	10.8
298	162.29	1391	11.7
323	169.43	1404.5	12.1
373	362.80	5476	6.6

4.4 Thermal Analysis

4.4.1 Thermogravimetric and Differential Scanning Calorimetry Analysis of 2

Crystals of **2** were subjected to thermogravimetric analysis (TGA) and differential scanning calorimetry (DSC) experiments to investigate the thermal stability of the compound. **Figure 4.12** shows the thermograms obtained for **2**. The TGA trace of the as-synthesised compound shows a one-step mass loss of 10.51% (calculated 10.89%), which occurs in the temperature range 50-240 °C and accounts for 0.96 DMF molecules per asymmetric unit. According to TGA, the sample begins to decompose at 350 °C and by 370 °C a substantial amount of sample is lost due to decomposition. In the DSC experiments of **2**, the peak at 30-50 °C is an artefact peak while four endotherms occur in the temperature range 75-130 °C, 130-152 °C, 200-218 °C and 230-260 °C, respectively. The DSC experiment was repeated several times with these endotherms constantly appearing in the same temperature ranges. The first endotherm between 75-130 °C is associated with desolvation of the compound, while the subsequent endotherms correspond to phase transitions in the structure. As noted in the VT-PXRD experiments, differences in the PXRD patterns compared to the calculated pattern occur at 100 °C and between 150-250 °C. The endotherm between 130-152 °C could be due to changes that occurred in the structure at 100 °C. Structural changes between 150-250 °C (VT-PXRD experiments) could be represented by the endotherms between 200-218 °C and 230-260 °C. Temperature programmes are different in TGA and VT-PXRD experiments, however, the sequence of events remain the same. The TGA and DSC results are summarised table 4.6 and table 4.7, respectively.

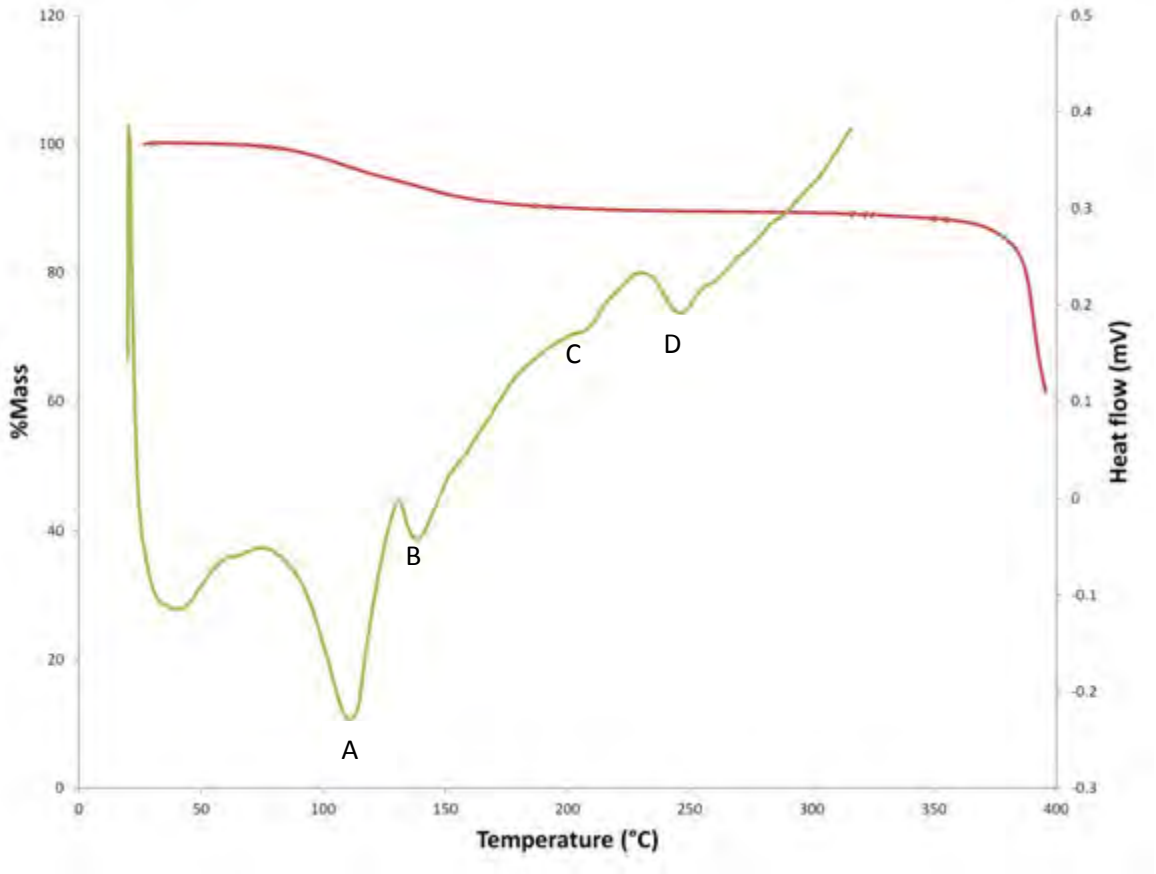

Figure 4.12: Overlay of TGA (red) and DSC (green) thermograms for **2** with desolvation indicated by A and possible phase transitions indicated by B, C and D

Table 4.6: TGA data obtained for **2**:

Temperature range	SCXRD molecules	Experimental values	Calculated %mass loss	Experimental %mass loss
50-240 °C	1.00	0.96	10.89	10.51

Table 4.7: DSC data obtained for **2**:

Peak	Temperature range (°C)	Enthalpy change (J g^{-1})	T_{onset} (°C)
A (Desolvation)	75-130	14.96	111.69
B (Phase transition)	130-152	2.00	141.28
C (Phase transition)	200-218	0.32	210.34
D (Phase transition)	230-260	1.55	241.19

4.4.2 Hot Stage Microscopy

Hot stage microscopy (HSM) experiments provide a visual indication of solvent loss and sample decomposition. The thermal events that were observed in HSM experiments occurred at slightly different temperatures than those in the TG and DSC analyses, due to differences in geometries of the experimental setup. Crystals of **2** were heated in the temperature range 25-380 °C (**Figure 4.13**). At 109 °C, the larger crystals started becoming opaque, while the smaller crystals start becoming opaque at 125 °C. The loss of monocrystallinity is associated with the crystals turning opaque. However, it was observed in VT-PXRD studies that **2** remained crystalline up to 250 °C. The first sign of solvent loss occurs at 136 °C and continues up to 267 °C as indicated by bubbles forming. The onset of decomposition occurs at 330 °C and the crystals are decomposed at 350 °C, which is consistent with the observation from TGA experiments.

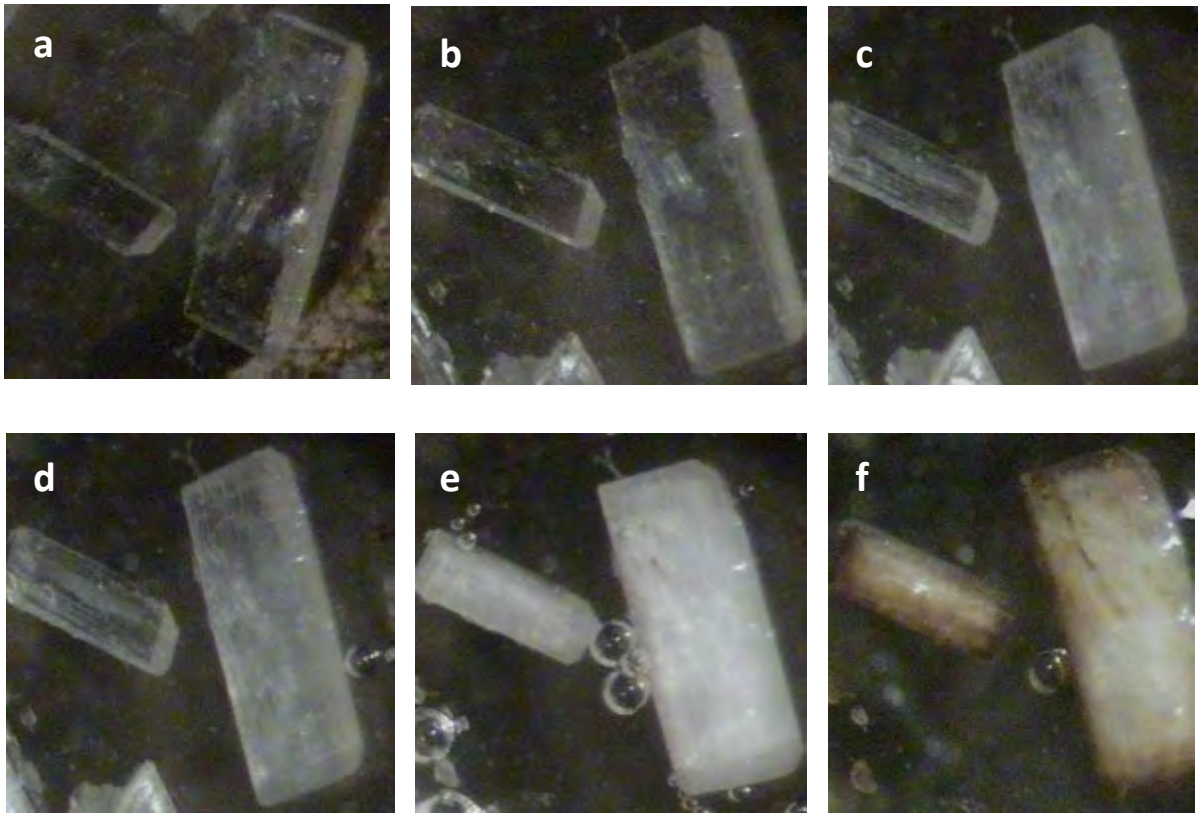

Figure 4.13: HSM images of **2** at **a)** 25 °C **b)** 109 °C **c)** 125 °C **d)** 136 °C **e)** 267 °C **f)** 350 °C

4.5 Cogrinding Experiments

Cogrinding experiments were performed on **2** in order to investigate whether the compound could be produced *via* the mechanochemical method (details of this method in **section 2.5**) since this method has the potential to produce high yields of the product. The experiment involved kneading the metal salt, $[Cd(NO_3)_2.4H_2O]$, and organic ligands (bpe and H_2nbdc) in a 1:1:1 ratio for 20 minutes using a mortar and pestle. A few drops of DMF were added to the mixture to assist the kneading process. The paste that formed was left to dry overnight. The characterisation of the resulting powder was carried out by comparison of the PXRD pattern of the material with the calculated pattern (**Figure 4.14**) obtained from SCXRD studies. The PXRD pattern of the kneaded material did not match that of the calculated pattern. Amongst the differences were peaks that were present in the kneaded material at 2θ positions 6.0°, 7.7° and 11.1° which were absent in the calculated pattern (298 K).

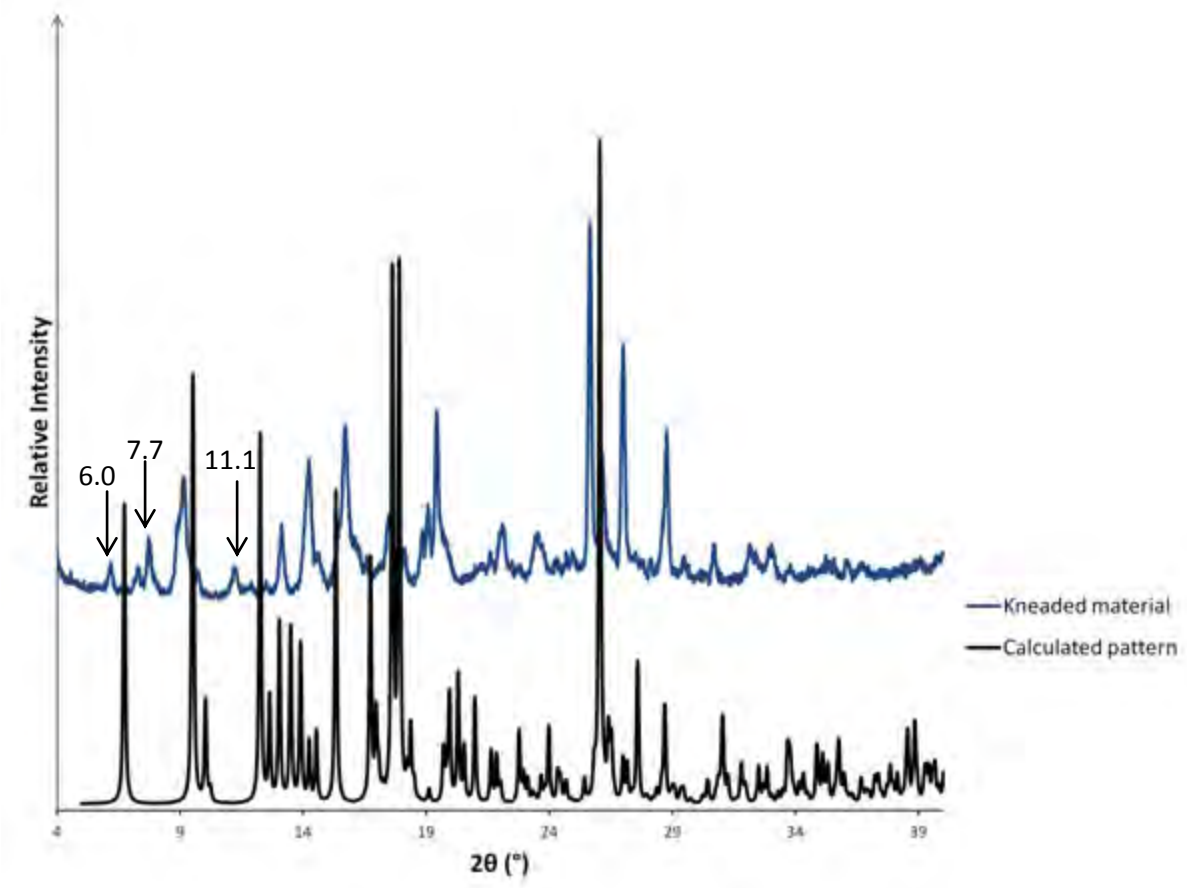

Figure 4.14: PXRD trace of kneaded material and calculated pattern of **2**

The PXRD trace of the kneaded material was compared to the patterns obtained for the starting materials used to synthesise **2**. However, the PXRD trace of cadmium(II) nitrate tetrahydrate could not be obtained directly, due to the hygroscopic nature of this starting material. **Figure 4.15** indicates that the PXRD pattern of the kneaded material does not match the patterns of the organic ligands. Therefore, it did not appear that the kneaded material was a physical mixture of the organic ligand starting materials. Further experiments were performed on the kneaded material in order to identify whether a new complex might have formed.

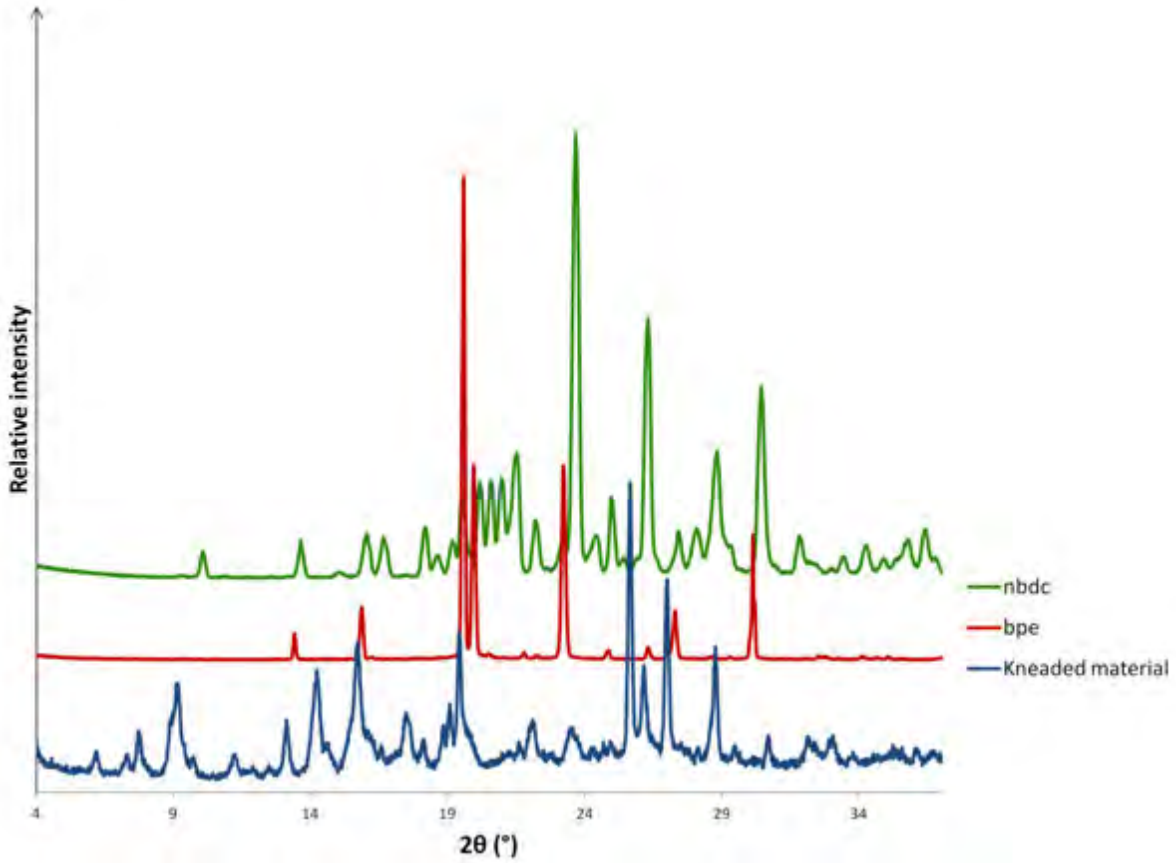

Figure 4.15: PXRD pattern of kneaded material and organic starting materials of **2**

4.6 Fourier Transform Infrared Spectroscopy

Fourier transform infrared (FT-IR) spectroscopy experiments were performed on the kneaded material to investigate the nature of the sample and whether any complexation had occurred. A shift to a lower wavenumber (compared to free ligand) in the absorption band is anticipated if the carboxylate functional groups are coordinated to the metal. FT-IR also confirms the deprotonation of the carboxylic acid groups. The asymmetric stretching

vibration mode, ν_{asym} (-COO^-), at 1610 cm^{-1} in the IR spectrum of the kneaded material (**Figure 4.16**) indicate that the carboxylic acid group is coordinated to the Cd(II) ion (1704 cm^{-1} in the free ligand shown in **Figure 4.17**). There is also an absence of the shoulder peak, which occurs at 1625 cm^{-1} in the H_2nbdc ligand IR spectrum. The results obtained from FT-IR provide evidence that the carboxylate group could be coordinated to the metal and a new complex might have formed. The nitro group occurs between the regions 1555–1485 cm^{-1} (asymmetric stretch) and 1355–1320 cm^{-1} (symmetric stretch), which is not indicated in the spectrum.[7] The kneaded material was not the desired product of this research project and no further investigation on the complex was performed.

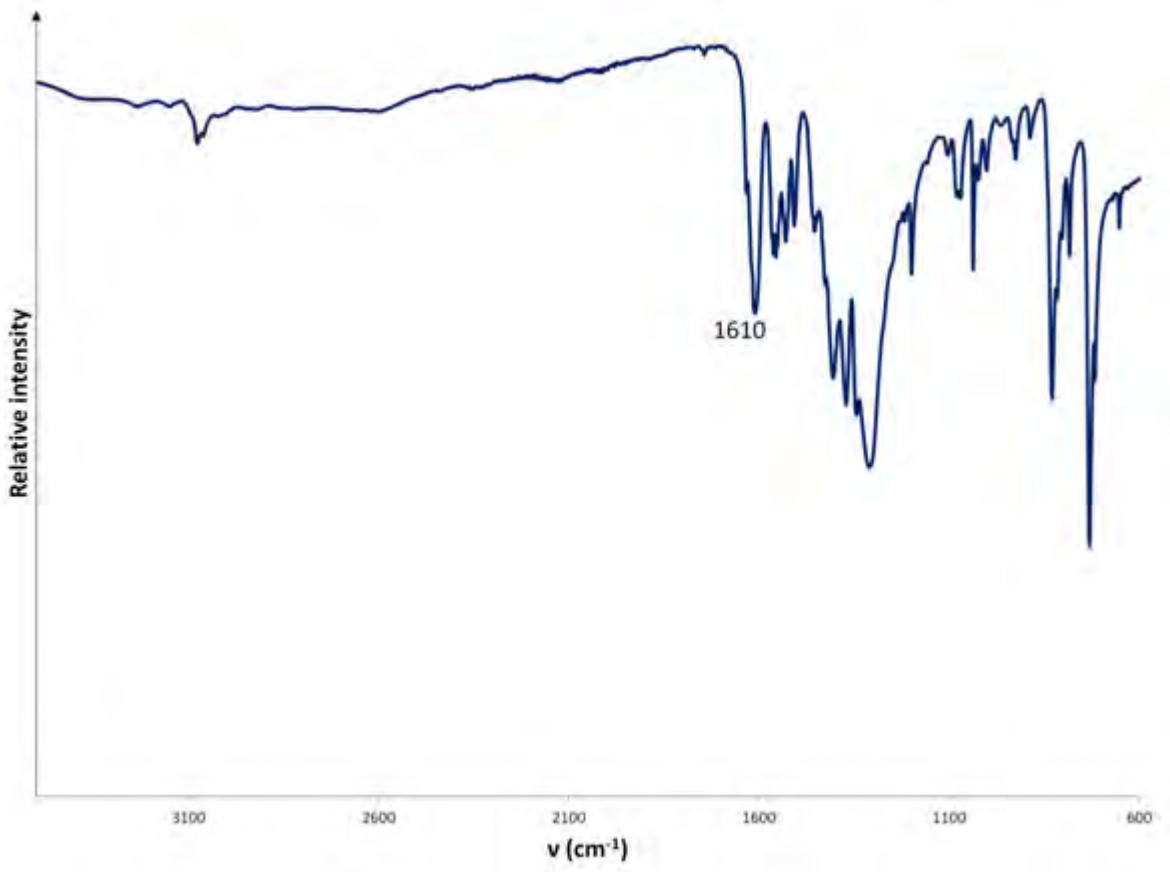

Figure 4.16: IR spectrum of kneaded material

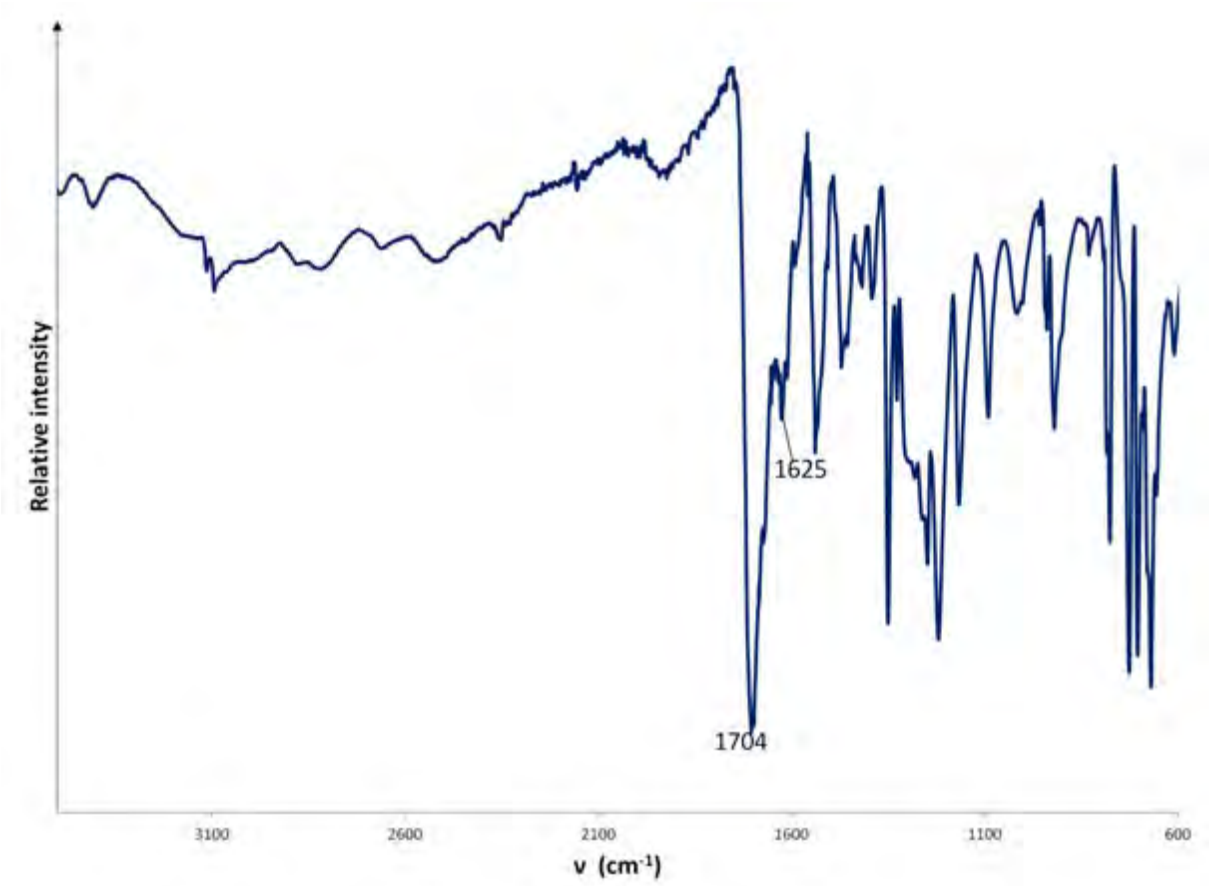

Figure 4.17: IR spectrum of 5-nitro-1,3-benzenedicarboxylic acid (H_2nbdc)

FT-IR experiments were performed on **2** to confirm the coordination of the nbdc ligand to the Cd(II) metal centre in the bulk sample. The presence of the asymmetric stretching vibration mode, ν_{asym}(-COO$^-$), at 1606 cm^{-1} in the IR spectrum of **2** indicates that the nbdc ligand is coordinated to the cadmium metal centre (**Figure 4.18**). Evidence that the nbdc ligand is fully deprotonated is given by the absence of the shoulder peak in the IR spectrum of **2** that occurs at 1625 cm^{-1} in the H_2nbdc IR spectrum. This result indicates the absence of hydroxyl hydrogen atoms.[8] The peak at 1343 cm^{-1} corresponds to the symmetric stretching vibrational mode, ν_s(-COO$^-$), with the difference between ν_{asym}(-COO$^-$) and ν_s(-COO$^-$) being 263 cm^{-1}. This suggests that the carboxylate group is coordinated in a bidentate fashion, which is consistent with the result obtained from SCXRD analysis for the ASU of compound **2**.[9] The values obtained for ν_{asym}(-COO$^-$) and ν_s(-COO$^-$) of **2** are close to those given for UJOJUY, which were reported as 1150-1620 cm^{-1} and 1390-1420 cm^{-1} for ν_{asym}(-COO$^-$) and ν_s(-COO$^-$), respectively.[4] The absorption band at 1678 cm^{-1} is associated with $\nu_{C=O}$ of the DMF molecule.[10]

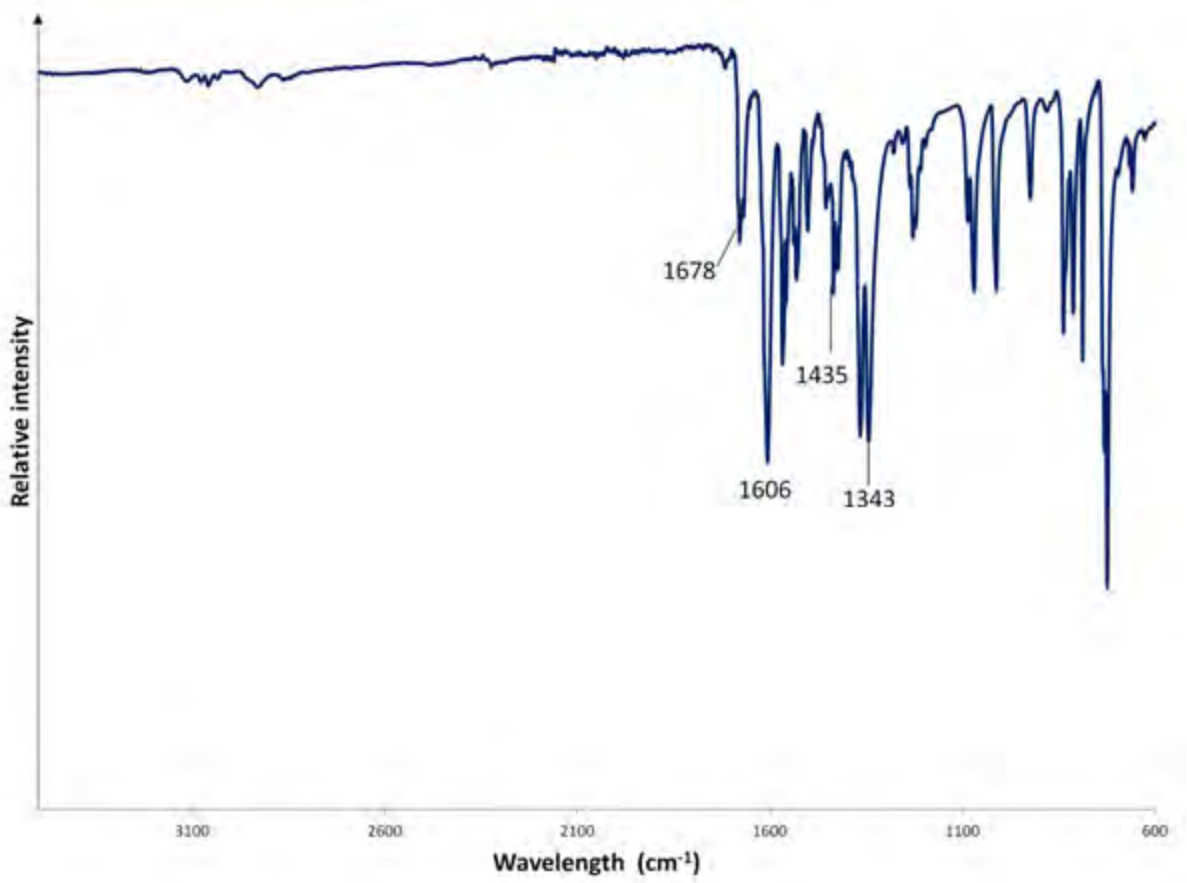

Figure 4.18: IR spectrum of **2**

4.7 Elemental Analysis

Crystals of **2** were subjected to elemental analysis (EA) to determine the percentage carbon, hydrogen and nitrogen present in the as-synthesised structure. The crystals were rinsed with ethanol and dried using filter paper prior to the analysis in order to remove any impurities that could have been present on the surface of the compound. The results obtained from EA are a relatively good match. Average values (n) are given in table 4.8. The results obtained for nitrogen and hydrogen deviate by 0.23% and 0.42%, respectively. These values are within in the general accepted value of 0.40%, according to the Journal of Organic Chemistry.[11] However, the results obtained for %C deviate by 0.76%. Nevertheless, PXRD experiments validated the purity of the bulk material.

Table 4.8: Elemental analysis results obtained for **2**

[Cd(bpe)$_{1.5}$nbdc]·DMF	**Calculated values**	**Average Experimental values (n=4)**
%C	51.90	51.14
%H	4.20	3.78
%N	10.44	10.21

4.8 Liquid Sorption Experiments

Various organic solvents were used to test the porosity of **2**. The organic solvents with different polarities (P') included DMF (6.4), methanol (5.1), chloroform (4.1) and toluene (2.4). Prior to solvent sorption studies, crystals of **2** were dried under vacuum at 100 °C for 12 hours in an attempt to remove the guest molecule. TGA confirmed no mass loss for the sample, thus confirming that the solvent was removed from the framework. The crystals were immersed in various solvents for 24 hours. TGA experiments were performed on the samples exposed to the various solvents but showed no mass loss for methanol, chloroform, and toluene. However, a mass loss of 14.62%, in the temperature range 21-220 °C, was observed for the crystals exposed to DMF. This is higher than the 9.71% observed for the as-synthesised compound in the same temperature range (**Figure 4.19**). The results obtained from solvent sorption experiments indicate that **2** absorbs the original guest molecule over the other solvents. The experiment also proved that the guest molecule was able to leave and enter the structure, indicating the porous nature of **2**, despite being a two-fold interpenetrated framework.

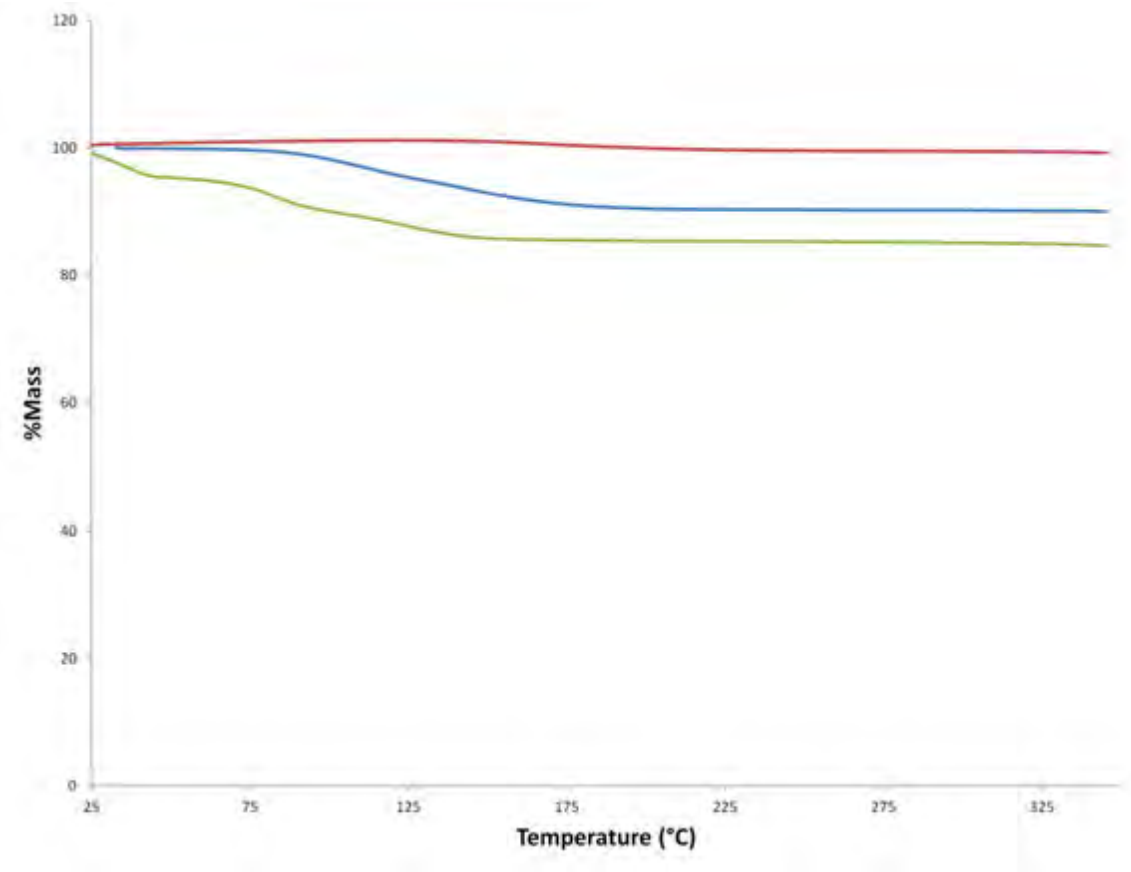

Figure 4.19: TGA of **2** for the as-synthesised MOF (blue), evacuated compound (red) and crystals exposed to DMF (green)

4.9 Gas and Water vapour Sorption Experiments

Gas sorption experiments were performed in order to investigate the ability of **2** to absorb gases, which included carbon dioxide and nitrogen gas as well as water vapour. The compound showed no sorption for nitrogen. Carbon dioxide sorption studies were conducted at 273 K and at 195 K (**Figure 4.20**). The sample displayed a type-I isotherm for carbon dioxide at 273 K and the total gas absorbed at absolute pressure (784 mmHg) was 18.5 cm^3 (STP) g^{-1}. The BET surface calculated value was 84 m^2 g^{-1}, with negligible hysteresis occurring for the desorption isotherm.

Interestingly, at 195 K, the compound absorbs more than double the amount of carbon dioxide compared to the experiment at 273 K at low absolute pressures and displays a type-IV isotherm. This type of isotherm is usually associated with mesoporous materials and contains clear, broad hysteresis loops. The framework behaviour responsible for this step-wise carbon dioxide adsorption could be due to, including reversible a) framework collapse,

b) conversion between interpenetrated geometries and/or c) pillar rotation of the ligand.[12] It is suggested that at the first inflection point (absolute pressure of 117 mmHg and 30.3 cm^3 (STP) g^{-1} carbon dioxide absorbed), structural events occur in the framework which further open cavities and allows the structure to absorb more of the gas. Structural changes also occur in the framework at the second inflection point (432 mmHg), which permits further gas sorption and by the absolute pressure of 710 mmHg, the total carbon dioxide absorbed was 54.7 cm^3 (STP) g^{-1} and the BET surface area calculated to a value of 127 m^2 g^{-1}. In order to observe the exact structural changes that occurred in the framework, SCXRD analysis involving pressure changes would be required, which was not performed in this study. The reason that these structural changes occur at 195 K may be that at the lower temperature there is an increase in strength of the intermolecular interactions, which induces the opening of the structure. Compound **2** was also shown to have a high affinity for water vapour (**Figure 4.21**). The total water absorbed at a relative pressure P/P_0 of 0.76 (at 298 K) was 43.2 cm^3 (STP) g^{-1} and the BET surface area calculated to 154 m^2 g^{-1}. No hysteresis occurred during the water vapour sorption experiment.

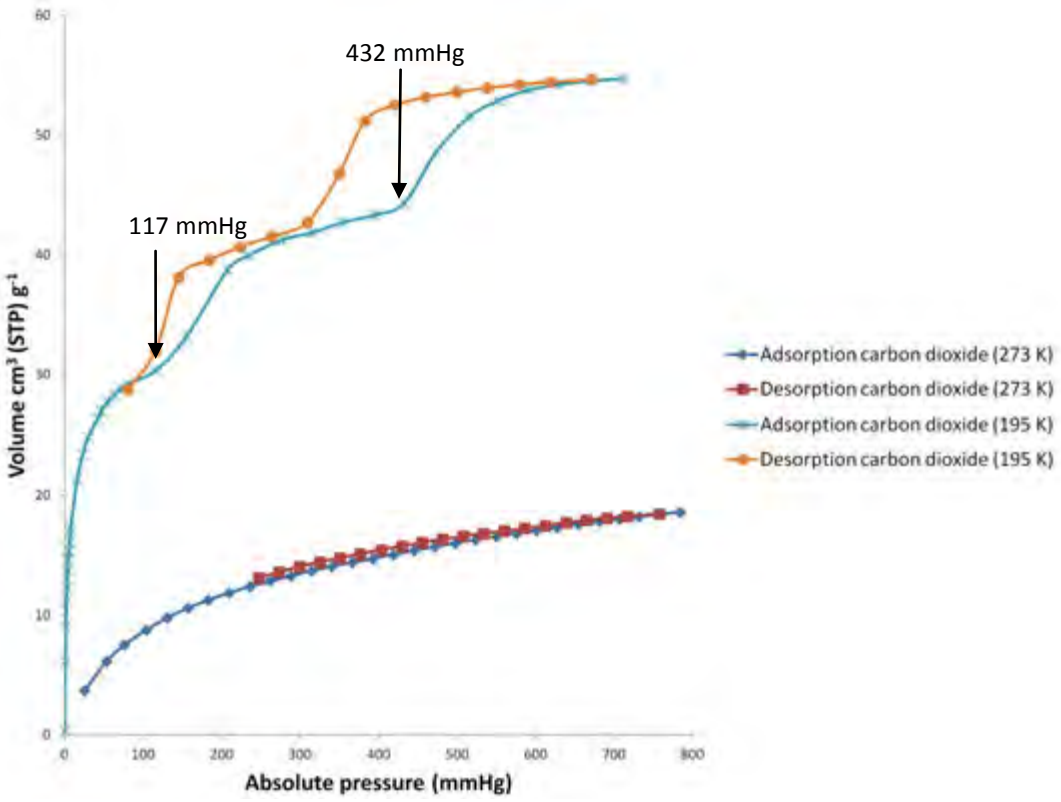

Figure 4.20: CO_2 adsorption and desorption isotherms of **2** at 273 K and 195 K

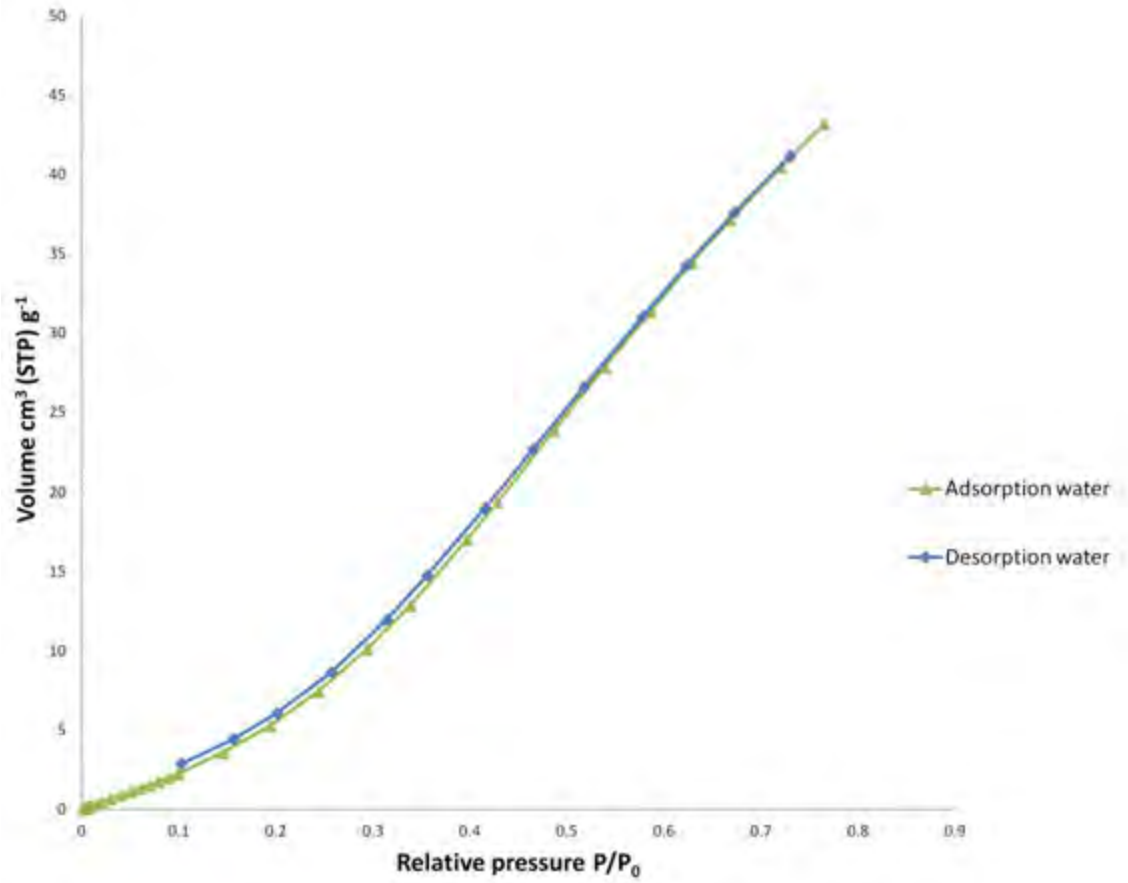

Figure 4.21: Water vapour adsorption and desorption isotherm of **2**

4.10 Summary

A two-fold interpenetrated, mixed-ligand, 2D MOF has been synthesised using $CdNO_3 \cdot 4H_2O$, 5-nitro-1,3-benzenedicarboxylic acid and 1,2-bis(4-pyridyl)ethane as the starting materials. The structure was compared with a similar compound found in the literature using the same metal ion and ligands (CSD ref UJOJUY).[4] VT-PXRD experiments confirmed that upon removal of the guest molecule, compound **2** remained crystalline. SCXRD analysis was performed at 104 K, 298 K, 323 K and 373 K on the same crystal in order to determine whether structural change can be monitored upon solvent loss. The most significant changes in the framework occurred at 373 K. Compound **2** displayed a type-I isotherm for carbon dioxide at 273 K and a type-IV sorption isotherm (containing hysteresis loops) for carbon dioxide at 195 K. Compound **2** readily absorbed water vapour at 298 K and low relative pressures.

4.11 References

1 Bruker (2007), *Bruker AXS Inc., Madison, Wisconsin USA*, 2007, **1**.

2 G. M. Sheldrick, *Acta Crystallogr. Sect. A Found. Crystallogr.*, 2008, **64**, 112–122.

3 G. M. Sheldrick, *Acta Crystallogr. Sect. A Found. Crystallogr.*, 2007, **64**, 112–122.

4 J. Luo, M. Hong, R. Wang, R. Cao, L. Han and Z. Lin, *Eur. J. Inorg. Chem.*, 2003, **14**, 2705–2710.

5 L. Carlucci, G. Ciani, D. M. Proserpio, T. G. Mitina and V. A. Blatov, *Chem. Rev.*, 2014, **114**, 7557–7580.

6 C. F. Macrae, I. J. Bruno, J. A. Chisholm, P. R. Edgington, P. McCabe, E. Pidcock, L. Rodriguez-Monge, R. Taylor, J. Van De Streek and P. A. Wood, *J. Appl. Crystallogr.*, 2008, **41**, 466–470.

7 J. Coates, *Encycl. Anal. Chem.*, 2000, 10815–10837.

8 X. Wang, J. Li, H. Lin, H. Hu, B. Chen and B. Mu, *Solid State Sci.*, 2009, **11**, 2118–2124.

9 Z. Y. Liu, X. G. Wang, E. C. Yang and X. J. Zhao, *Z. Anorg. Allg. Chem.*, 2008, **634**, 1807–1811.

10 H. Chang, M. Fu, X. J. Zhao and E. C. Yang, *J. Coord. Chem.*, 2010, **63**, 3551–3564.

11 Guidelines for Authors, *J. Org. Chem.*, 2016, <http://pubs.acs.org/paragonplus/submission/joceah/joceah_authguide.pdf>, (accessed 5 October 2016).

12 K. L. Mulfort, O. K. Farha, C. D. Malliakas, M. G. Kanatzidis and J. T. Hupp, *Chem Eur. J.*, 2010, **16**, 276–281.

CHAPTER 5: CONCLUSION

This chapter provides a summary of the results obtained for this research project. Two mixed-ligand 2D MOFs were synthesised and fully characterised using X-ray diffraction studies, thermal analysis, Fourier transform infrared spectroscopy, elemental analysis, gas and water vapour sorption studies.

5.1 Summary

5.1.1 $[Zn_3(BTC)(4,4'\text{-bpdo})(OH)(SO_4)(H_2O)_3]_n \cdot n(H_2O)_{2.33}$ (**1**)

A novel 2D mixed-ligand MOF was synthesised by the solvothermal method using zinc(II), 1,3,5-benzenetricarboxylic acid and 4,4'-bipyridine-*N*,*N*'-dioxide. The compound was fully characterised using SCXRD, VT-SCXRD, PXRD, VT-PXRD, TGA, DSC, HSM, EA and FT-IR spectroscopy. Gas and water vapour sorption experiments were performed on **1** to investigate the porosity of the MOF.

The 2D networks are arranged in a polar fashion, which is consistent with the polar space group *R*3. Single crystal structure analysis was performed at 104 K, 298 K, 323 K and 373 K in order to determine whether structural changes could be observed upon solvent loss. The results obtained from single crystal analysis confirmed a SCSC transformation at successive temperatures and indicated a probable order of water release when the as-synthesised compound was subjected to TG experiments. Structure determinations obtained from VT-SCXRD studies suggest that the order of water release from the compound is the uncoordinated water molecules (O6W/O5W, O4W) followed by the coordinated water molecules (O1W/O2W and O3W).

Mercury revealed that the compound contained isolated cavities.[1] This, however, did not interfere with the dehydration process, which according to Sun *et al*. is made possible by the presence of open channels.[2] The dehydration process indicated that structural changes occur in the framework when the water molecules leave the structure. It was ascertained that the dehydration process is reversible and that it occurs *via* a SCSC process only if the last coordinated water molecule is present in the structure. VT-PXRD experiments provided a visual indication that the crystallinity of **1** was lost at 190 °C.

Gas sorption experiments were performed on **1** using nitrogen, carbon dioxide (at 273 K and 195 K) and water vapour. Nitrogen and carbon dioxide (at 273 K) isotherms showed low sorption values of 2.7 cm^3 (STP) g^{-1} and 1.1 cm^3 (STP) g^{-1}, respectively. Although sorption values of carbon dioxide at 273 K were low, the sample seemed to absorb more of the gas at 195 K, probably due to the lower available energy in the system to overcome supramolecular interactions. At 195 K, the sample absorbed 17.3 cm^3 (STP) g^{-1} of carbon dioxide at relative pressure P/P_0 of 0.89 and the BET surface calculated from this equal to 60 m^2 g^{-1} for the compound. The water vapour sorption/desorption isotherms of the activated compound showed a type-I isotherm associated with microporous materials (pores with an internal width < 2 nm)[3] and also confirms its high affinity for water, with the total absorbed value of water equal to 195.5 cm^3 (STP) g^{-1} at relative pressure P/P_0 of 0.81 (at 298 K). The BET surface area was calculated to be 477 m^2 g^{-1} for water vapour.

The effect of pH was tested on the MOF using 3 M H_2SO_4 and triethylamine. Crystals of **1** were obtained under acidic conditions only. Co-crystals of the organic starting molecules (H_3BTC and 4,4'-bpdo) form when **1** is dissolved in an acid medium of 3 M H_2SO_4 and water. The co-crystals were characterised using SCXRD, TGA, DSC and HSM. Structure determination revealed that hydrogen bonding exists between the organic molecules.

5.1.2 $[Cd(bpe)_{1.5}nbdc]_n \cdot nDMF$ (2)

A mixed-ligand, interpenetrated 2D MOF was synthesised by the solvothermal method using cadmium(II), 5-nitro-1,3-benzenedicarboxylic acid and 1,2-bis(4-pyridyl)ethane. The compound was fully characterised using SCXRD, VT-SCXRD, VT-PXRD, TGA, DSC, HSM, EA and FT-IR spectroscopy. Gas, solvent and water vapour sorption experiments were performed to investigate the porosity of **2**.

Compound **2** is similar to a 3D MOF reported in the literature that has the formula $[Cd(bpe)_{1.5}nbdc]0.25H_2O$ (UJOJUY).[4] Differences between the compounds include different solvent molecules in the framework and the degree of interpenetration of the frameworks. Compound **2** contained a single DMF molecule and was found to be two-fold interpenetrated, whilst UJOJUY contained a water molecule and was reported as being a three-fold interpenetrated MOF.

VT-SCXRD analysis was performed at 104 K, 298 K, 323 K and 373 K on the same crystal in order to observe structural changes that occur when the solvent is removed from the framework. Overlays of the asymmetric unit at 298 K and 323 K with the 104 K structure showed a close match, with slight changes in the orientation of the pyridyl rings of the bpe ligand as the temperature increases. The orientation of the pyridyl rings of the bpe ligand varied predominantly at 373 K compared to the lower temperatures. Additional differences at 373 K also included i) DMF being absent from the structure, ii) a space group change from $P\bar{1}$ to $C2/c$, iii) a quadrupling of the unit cell and iv) a lattice type change of the structure.

Mercury revealed that the cavities consisted of voids which formed channels.[1] The guest molecule could reversibly enter or leave the framework, while other organic solvents showed negligible sorption as demonstrated by liquid sorption experiments. The experiment also illustrated the porous nature of compound **2** despite being a two-fold interpenetrated network. VT-SCXRD analysis confirmed that the structure remained crystalline once the guest molecule is removed.

Gas and water vapour sorption experiments were performed on the activated compound. The compound absorbed 18.5 cm^3 (STP) g^{-1} at 273 K for carbon dioxide at an absolute pressure of 784 mmHg and the BET surface area was calculated to 84 m^2 g^{-1}, whilst more of the gas was absorbed at a lower temperature of 195 K. A type-IV isotherm was obtained for the carbon dioxide experiment at 195 K, which is usually associated with mesoporous materials (pores with an internal width between 2-50 nm)[3] and consists of broad hysteresis loops, associated with changes in the framework. The changes in the framework could be due to the opening and closing of the structure triggered by increased strength of intermolecular interactions at the lower temperature. A total of 54.7 cm^3 (STP) g^{-1} gas was absorbed at absolute pressure of 710 mm Hg at 195 K for carbon dioxide. The BET was calculated to a value of 127 m^2 g^{-1} at the lower temperature for carbon dioxide. Compound **2** also readily absorbed water vapour at relative pressures P/P_0 of 0.76 with a total of 43.2 cm^3 (STP) g^{-1} water vapour absorbed by the compound at 298 K. The BET surface area was calculated to a value of 154 m^2 g^{-1} for water vapour.

5.2 Final remarks and future work

The objectives of this project (**section 1.11.2**) were successfully completed using the mixed-ligand approach to synthesise MOFs. Two mixed-ligand MOFs were prepared using zinc(II) and cadmium(II) as the metals with carboxylate-based ligands and pyridyl ligands. The compounds were fully characterised using X-ray diffraction analysis, thermal analysis, Fourier transform spectroscopy and elemental analysis. Gas and liquid sorption experiments showed that both compounds are porous and that they are able to absorb carbon dioxide gas and water vapour.

Suggestions for future work on compound **1** would involve cogrinding experiments using water as the solvent. It would be interesting to investigate whether compound **1** could be synthesised using this method. Future work for compound **2** would include further investigation of the three-step sorption profile of the compound. SCXRD experiments under gas pressure could provide a representation of the crystal structure at the different pressures, therefore, giving an accurate idea of the changes that occur in the framework.

5.3 References

1 C. F. Macrae, I. J. Bruno, J. A. Chisholm, P. R. Edgington, P. McCabe, E. Pidcock, L. Rodriguez-Monge, R. Taylor, J. Van De Streek and P. A. Wood, *J. Appl. Crystallogr.*, 2008, **41**, 466–470.

2 Z. Su, M. Chen, T. Okamura, M. sheng Chen, S. Chen and W. Sun, *Inorg. Chem.*, 2011, **50**, 985–991.

3 I. Senkovska and S. Kaskel, *Chem. Commun.*, 2014, **50**, 7089–7098.

4 J. Luo, M. Hong, R. Wang, R. Cao, L. Han and Z. Lin, *Eur. J. Inorg. Chem.*, 2003, **14**, 2705–2710.